ABSTRACT

Title of Dissertation: DESIGN, FABRICATION, AND PERFORMANCE CHARACTERIZATION OF MULTIFUNCTIONAL STRUCTURES TO HARVEST SOLAR ENERGY FOR FLAPPING WING AERIAL VEHICLES

Ariel Perez-Rosado, Doctor of Philosophy, 2016

Dissertation directed by: Hugh A. Bruck, Professor, Department of Mechanical Engineering

Flapping Wing Aerial Vehicles (FWAVs) have the capability to combine the benefits of both fixed wing vehicles and rotary vehicles. However, flight time is limited due to limited on-board energy storage capacity. For most Unmanned Aerial Vehicle (UAV) operators, frequent recharging of the batteries is not ideal due to lack of nearby electrical outlets. This imposes serious limitations on FWAV flights. The approach taken to extend the flight time of UAVs was to integrate photovoltaic solar cells onto different structures of the vehicle to harvest and use energy from the sun. Integration of the solar cells can greatly improve the energy capacity of an UAV; however, this integration does effect the performance of the UAV and especially FWAVs. The integration of solar cells affects the ability of the vehicle to produce the aerodynamic forces necessary to maintain flight. This PhD dissertation characterizes the effects of solar cell integration on the performance of a FWAV. Robo Raven, a

recently developed FWAV, is used as the platform for this work. An additive manufacturing technique was developed to integrate photovoltaic solar cells into the wing and tail structures of the vehicle. An approach to characterizing the effects of solar cell integration to the wings, tail, and body of the UAV is also described. This approach includes measurement of aerodynamic forces generated by the vehicle and measurements of the wing shape during the flapping cycle using Digital Image Correlation. Various changes to wing, body, and tail design are investigated and changes in performance for each design are measured. The electrical performance from the solar cells is also characterized. A new multifunctional performance model was formulated that describes how integration of solar cells influences the flight performance. Aerodynamic models were developed to describe effects of solar cell integration force production and performance of the FWAV. Thus, performance changes can be predicted depending on changes in design. Sensing capabilities of the solar cells were also discovered and correlated to the deformation of the wing. This demonstrated that the solar cells were capable of: (1) Lightweight and flexible structure to generate aerodynamic forces, (2) Energy harvesting to extend operational time and autonomy, (3) Sensing of an aerodynamic force associated with wing deformation. Finally, different flexible photovoltaic materials with higher efficiencies are investigated, which enable the multifunctional wings to provide enough solar power to keep the FWAV aloft without batteries as long as there is enough sunlight to power the vehicle.

DESIGN, FABRICATION, AND PERFORMANCE CHARACTERIZATION OF MULTIFUNCTIONAL STRUCTURES TO HARVEST SOLAR ENERGY FOR FLAPPING WING AERIAL VEHICLES

by

Ariel Perez-Rosado

Dissertation submitted to the Faculty of the Graduate School of the
University of Maryland, College Park, in partial fulfillment
of the requirements for the degree of
Doctor of Philosophy
2016

Advisory Committee:
Professor Hugh A. Bruck, Chair
Professor Satyandra K. Gupta
Professor Abhijit Dasgupta
Professor Sarah Bergbreiter
Professor Sung W. Lee (Dean's Representative)

Dedication

I dedicate this dissertation to my parents Mandy and Ariel and my sister Mariely. They have always and will always be my biggest supporters and I will always love them for that.

Acknowledgements

I would like to express gratitude toward my research advisor, Dr. Hugh Bruck, for his guidance throughout the entire course of this dissertation. I learned so much about research and life along the way and will always be grateful for the experiences and lessons along the way. I would also like to express gratitude toward Dr. Satyandra Gupta for his guidance and help through the years as well.

Additionally, I would like to thank Dr. Sarah Bergbreiter, Dr. Abhijit Dasgupta, and Dr. Sung Lee for serving on this committee.

Looking back at the progress that has been made throughout the years, there is no way that this much progress would have been made without the help of a few people. First I would like to thank the other PhD students in the Robo Raven team. John Gerdes, Luke Roberts, and Alex Holness have all helped in the development of Robo Raven.

Lastly, I would like to thank Dr. Byung-Lip "Les" Lee and the ASFOR for their financial support. This work was sponsored by AFOSR grant FA9550-12-10158.

Table of Contents

List of Tables

List of Figures

Chapter 1: Introduction

1.1 Background

Unmanned Aerial Vehicles (UAVs) have gained a significant amount of attention in recent years due to their versatility in a wide range of missions and applications. UAVs are heavily utilized in the military for reconnaissance missions. With onboard cameras and sensors, specialists can observe an area of interest without endangering any lives. Similarly, UAVs can also be used in rescue efforts where an inhospitable area can be surveyed quickly. UAVs have also gained considerable attention from civilians that have found several commercial applications for these vehicles. Farmers could easily use a small UAV to survey their fields and check on their crops saving time, fuel, and energy. UAVs have even been used for cinematography and video production to safely obtain an aerial shot for certain scenes. Besides the aforementioned military and commercial uses, hobbyist have had a huge interest in UAVs for years. There are model airplanes, helicopters, and quadrotors that have been built by people from all walks of life.

UAVs can be broadly classified into rotorcraft, airplanes, or flapping wing aerial vehicles (FWAV). Rotorcraft are very maneuverable and generate a large amount of lift. This enables them to hover very well, but lack the speed to cover a large distance in a short amount of time. On the other hand, airplanes or fixed wing aircraft use thrust force to generate aerodynamic lift. This means they can cover large distances very quickly, but cannot hover and lack the maneuverability of a rotorcraft. FWAVs are unique in that they provide a versatile compromise between these two

extremes. Depending on how they are designed, FWAVs can hover just like rotorcraft or cover large distances like fixed wing aircraft. Smaller scale FWAVs take inspiration form insect based flight [5]. These FWAVs can hover and move very much like rotorcraft. Larger scale FWAVs take more inspiration from avian flight [1]. These UAVs can achieve greater speeds than their smaller counterparts while still maintaining more maneuverability than fixed winged aircraft.

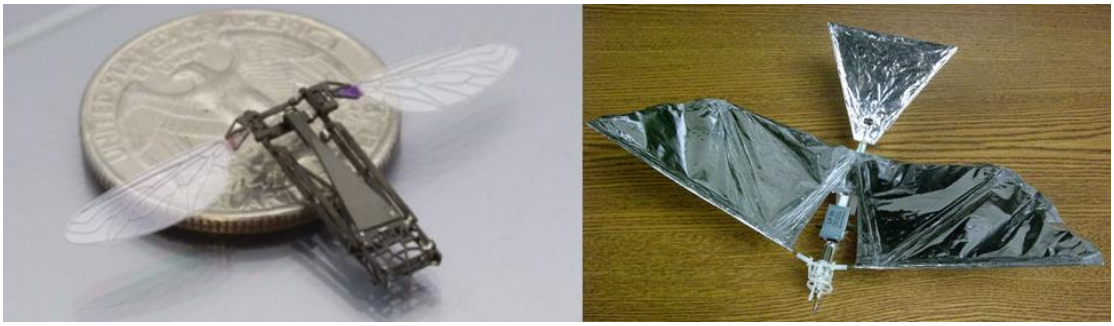

Figure 1.1*:* Left) Insect based UAV design [5] Right) UMD avian inspired UAV design [1]

Prior work at the Advanced Manufacturing Laboratory (AML) in the University of Maryland has demonstrated the utility of FWAVs as research platforms and as practical flying prototypes capable of transmitting live video, morphing wings, and having relatively large payload capacities [1]. These UAVs used a single DC motor to drive the wings in a synchronized symmetric manner. The FWAVs developed previously in AML lay the groundwork for the work presented in this dissertation.

1.2 Motivation for Research

A major factor in the performance of an UAV is onboard energy capacity. For UAVs that are powered and flown with an onboard battery, the size of the battery is limited by the payload capacity of the vehicle. This limitation hinders the flight

endurance for the UAV, a problem seen throughout the UAV field. A possible way to overcome this challenge would be to increase the available energy capacity by using on-board solar cells. This allows for increased flight time while decreasing the payload contribution of a large power source, thus potentially allowing for either: (1) battery size reduction or battery removal with the same performance capability, or (2) an increase in overall payload capacity. By integrating solar cells into the existing structures of UAVs, multifunctional structures are created. Multi-functional structures combine multiple functional requirements into a single structural component to create better efficiency in the overall design. Successful development of multifunctional structures can be expanded to other UAVs, including fixed wing and rotary craft. However to integrate commercial solar cells to the structures of an UAV, a large UAV must be developed to have enough surface area for solar cell integration.

It is unclear how the integration of photovoltaic (PV) solar cells will effect vehicle performance. Integrating these solar cells will add mass to the vehicle, causing inertial changes to various structures of the vehicle. Also, integrating PV solar cells into the wing will alter wing deformation. PV solar cells are expected to alter the stiffness of any vehicle component that they are integrated into. This change in stiffness alters how the wings deform while flapping. Wing deformation is an important aspect in force generation [1]. Altering the wing design is expected to affect wing force generation. However, due to a lack of wing models for FWAVs, we cannot predict the severity of these changes. It is clear that solar cell integration can be beneficial by increasing the vehicle's onboard energy capacity; however, how

beneficial and at what cost are unknown. This dissertation aims to determine the benefits of PV cell integration and the cost in performance associated with that integration.

1.3 Goal and Scope

This work aims to characterize solar cell integration into the structures of a flapping wing unmanned aerial vehicle. Successful integration can lead to self-charging and increased flight endurance. With efficient enough solar cells, infinite flight time with direct sunlight may be achieved. However, it is the modeling work in multifunctional UAV design that has the most significant impact on the field. The goals of this work are as follows:

1. *Develop an approach to integrate photovoltaic solar cells to the existing wing structure of the UAV*: The wings offer the largest surface area for solar cell integration. The wings are also responsible for the lift and thrust generation of a FWAV. A new manufacturing technique is required to integrate these cells while still maintaining the necessary compliance for flight.

2. *Characterize the impact of solar cell integration:* New wing designs with solar cells integrated into the wings must be developed, characterized, and tested. Changes in wing deformation must be measured and characterized to understand how these design changes affect performance. A multifunctional performance model must be developed to evaluate and predict how the changes in performance and mass affect

flight time of the FWAV. Aerodynamic models must be developed to explain how the changes in design are expected to alter the performance of the vehicle.

3. *Limitations created by solar cell integration*: Since the existing wings have been completely saturated with solar cells, new larger wings that can incorporate more PV cells can be designed. The changes in performance caused by scaling up to larger wings must be measured, understood, and modeled. The tail and body are the last two places on the UAV where solar cells can be integrated. The body is not responsible for force generation so is only expected to contribute to an increase in mass. Since the tail is responsible for control of the UAV, performance is expected to be affected. This change in performance should be quantified and modeled as well as the electrical benefits from the additional PV solar cells.

4. *Investigate new photovoltaic cell technologies*: Newer more efficient PV cell technologies exist and must be investigated. The best technology that will have the smallest effect on performance while still providing benefits in electrical power must be identified. Then, the actual effects on performance through solar cell integration must be identified by designing a FWAV based off of these cells. The goal is to design a FWAV that can be completely powered by the sun and fly as long as there is sunlight without a battery.

Chapter 2: Literature Review

In this chapter, literature related to the goals of the proposed work is surveyed. Due to the multidisciplinary nature of this work, this literature review covers several topics that give intellectual insight to the different issues and challenges faced in this work. First, previous UAV designs and accomplishments are observed. Next, a review of photovoltaic solar cell technology is conducted, followed by a review of multifunctional design. Previously used measurement techniques are also reviewed as well as modeling efforts from the UAV community.

In Section 2.1 previously built UAVs are observed. In doing so, a clear distinction can be made from what has already been accomplished and areas where significant progress can be made. This section serves to explain how the developed FWAV is different from what has already been built, and how the FWAV developed progresses the field of UAVs.

Section 2.2 is a review of photovoltaic (PV) solar cell technology. Certain information on PV solar cells must be known if we plan to integrate them to the structures of an UAV. Here we investigate different PV technologies, the mechanical properties of the PV solar cells, and how current UAV designs integrate them to their systems.

Section 2.3 reviews aspects of multifunctional design. A general overview of multifunctional design is introduced to help define our goal for solar cell integration. Current UAVs with multifunctional designs are also observed.

Measurement and data collection techniques are very important in obtaining information about UAV performance. This information is also critical for model

generation. To compare the results obtained in this work to any previous work, an understanding of how the previous data was collected is important. Section 2.4 investigates current and previous methods being used to measure the aerodynamic forces being generated by UAVs. Section 2.5 investigates how to extract the deformation of the wings through Digital Image Correlation (DIC).

Section 2.6 covers information that previous researchers have been able to determine, through their efforts, about certain aspects that enable these UAVs to obtain flight. This section also investigates current modeling efforts for FWAV wings. It is with this section that we aim to identify key components of wing design that have a direct correlation to flight performance.

2.1.1 Vertical Based Flight

The majority of research thus far has been accomplished on the micro scale. These small vehicles are known as Micro Aerial Vehicles (MAVs). At this size, flight behavior mimics the flights of insect and small birds. Researchers design these MAVs to fly vertically and to be capable of great maneuverability. The following section investigates the advances in vertical-based flight to understand the challenges other researchers have faced.

Vijay Kumar designed and created the smallest autonomous quadrotors capable of exploring, mapping and scouting an unknown three-dimensional building-like environment [2]. This UAV is capable of vertical flight with very controllable maneuverability (similar to insects and small birds). Even though this UAV is not a FWAV, it runs into similar challenges faced by FWAVs. Due to the necessary onboard components needed to achieve the mapping capabilities, the UAV is limited

to a minimum length of 0.75m and a mass a little less than 2 kg. This leads to a power consumption of over 400 Watts. With the best available battery, this UAV is only capable of a mission time of 10-20 minutes. This work introduces the need for more power or a more efficient system. Since this is a quadrotor design, the only way to obtain more power is through advances in battery technology.

The MFI project at the University of Berkeley [4] is looking at using flapping wings instead of rotor technology. They are studying wing behavior with 2 degrees of freedom. Their design calls for a wing with a length of 25cm with an average chord length of 6.7cm. Though these wings are not small, they are 2.3 mm thick which make them more comparable to the behavior of wings used for MAVs. The wings experience a 90 degree rotation at the end of each up and down stroke with a 140 degree flapping range. This group is simply observing flapping wing behavior and do not have an actual flying vehicle; however, they are collecting the aerodynamic forces generated by the flapping wing. To do so, they use a 2 degree of freedom (DOF) load transducer attached to the supporting structure of the wing. Minimizing friction, they are able to collect the lift and thrust forces generated by the wings. The flapping velocity and rotation of the wing are altered and the results are compared. Using their methods of data collection they are able to decouple the rotational contributions of the wings from the simple flapping motion.

The wings used in the MFI group are very similar in design to the wings used in Robert Wood's group out of Harvard [5]. They created a MAV at a very small scale. They were able to achieve much more flight control by using two piezoelectric actuators.

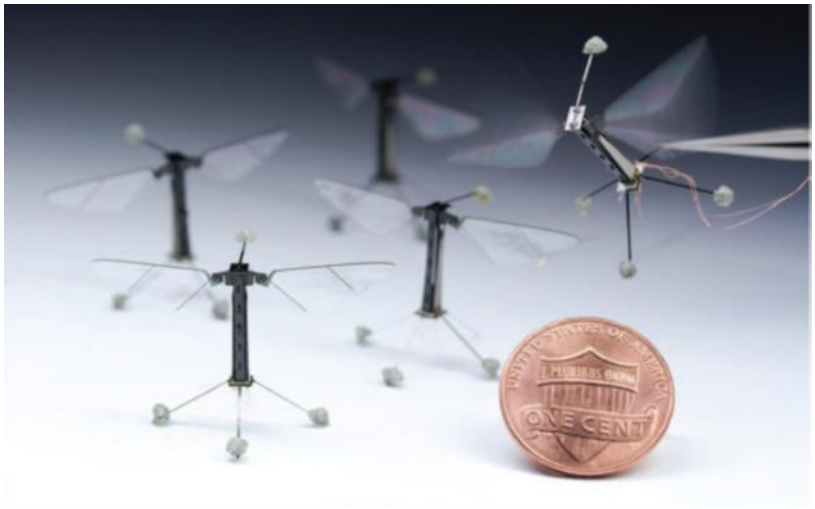

Figure 2.1: Robotic fly design with a pair of independently actuated wings [5]

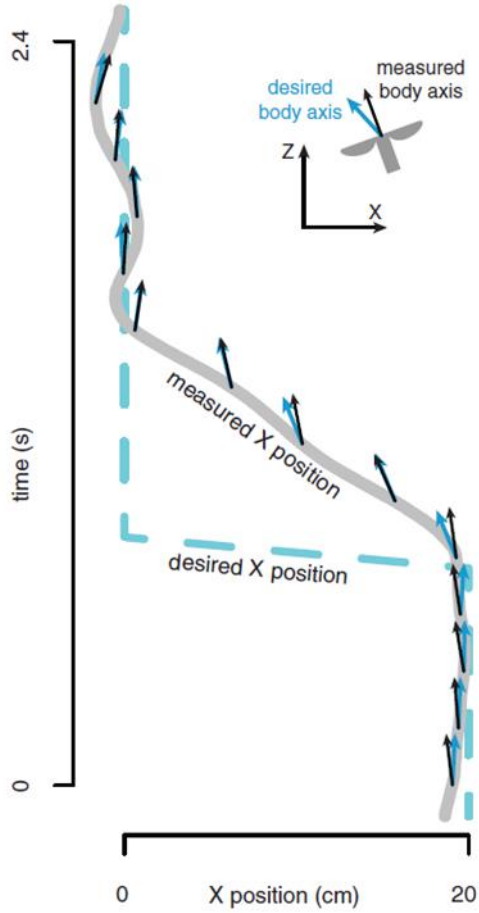

Figure 2.2: Laterally controlled movement of robotic fly [5]

Having two piezoelectric actuators allows for more flight control. Flapping one wing differently than the other alters the symmetry causing the body to roll and change the trajectory of the vehicle. Independent wing control is certainly an advantage to gaining maneuverability and is something that can be applied to larger more lateral based FWAV designs. However, a major drawback of these vehicles is their power source. Because they are so small and demand such high power, these vehicles are tethered to a nearby power supply. This can be seen in Figure 2.1, where the two copper wires are attached to the moving vehicle. This is a huge limitation to this design. A battery may simply add too much payload at this scale. Even with a battery small enough, it may not provide enough power to achieve the same flight observed experimentally.

Another small tethered design from Virginia Tech uses a rotary actuator [6]. The flight dynamics are very similar to the Berkeley and Harvard MAVs however this MAV uses a small pager motor to drive the wing instead of the piezoelectric actuator. The use of a motor to drive the wings makes this design easier to scale up. This design also introduces a tail consisting of 4 flaps to stabilize the MAV's flight. Instead of using independent wing control to alter the vehicle's flight path, the tail is actuated to control the vehicle's flight. This MAV is tethered to a power supply, but it can be easily scaled to a larger body using DC motors and available batteries. This was the direction taken with the SF-3 Mentor robot [7]. This vertical flight UAV is much larger than the FWAVs previously mentioned. It weighs 440 grams with a 0.36 meter wingspan. Unlike the previous designs, this UAV uses 4 wings, and is powered by a NiCd battery pack. However, the power required to lift 440 grams was

very demanding on the 8 pack NiCd battery used and as a result the maximum flight time of this UAV was only 20 seconds. However short the flight may have been, it was able to fly without a tether.

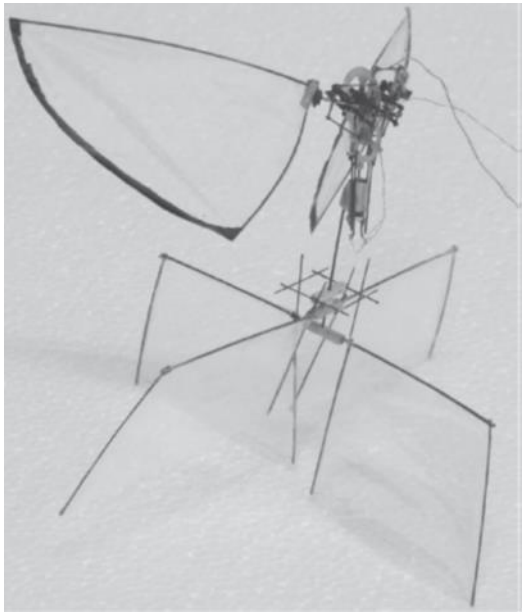

Figure 2.3: Tethered MAV with rotary actuator [6]

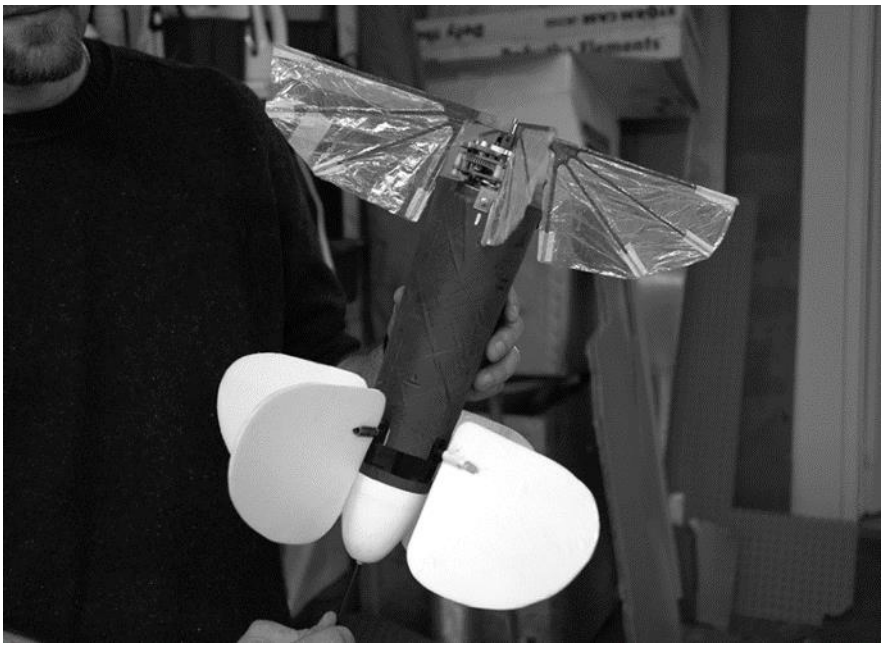

Figure 2.4: SF-3 Mentor Robot [7]

The final vertical flight MAV observed was the Nano Humingbird [8]. This vehicle is similar to the previous two in that it is powered by a DC motor, but unlike

the Mentor Robot it is much smaller scale. It weighs a total of 19 grams and has a wingspan of 16.5 cm. With less weight and a smaller battery, the maximum flight time was 4 minutes. What is interesting about this system is that the linkage that transfers power to the wings is cable driven. Turning is done by changing the tension at the bottom of the wings. This shows that by tensioning one wing more than the other, the performance of the FWAV is altered. Powering this much smaller design is a Lihium Polymer battery. The result is a tailless hummingbird-like robot.

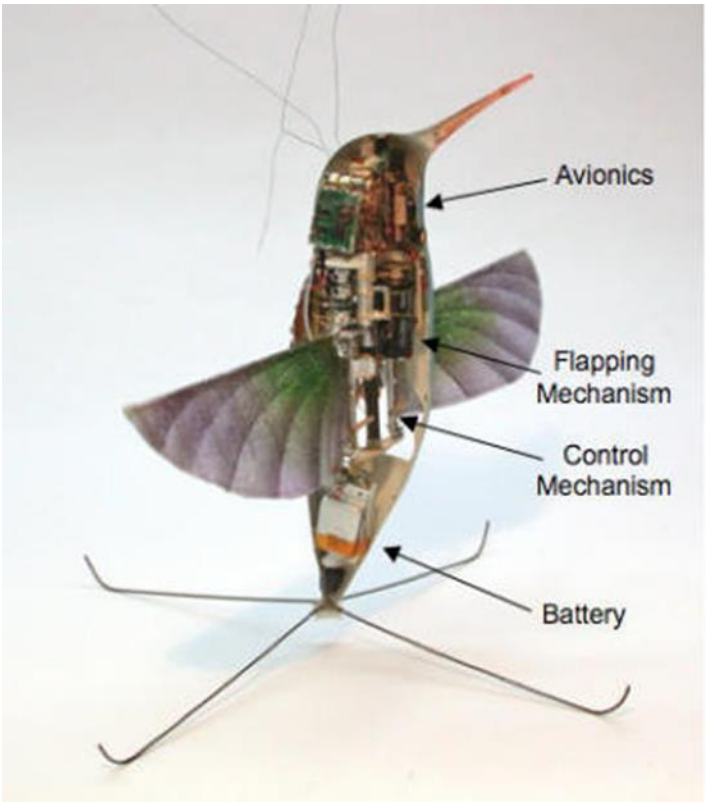

Figure 2.5: Nano Hummingbird [8]

2.1.2 Lateral Based Flight

When transitioning from vertical flight to lateral flight, there are a few common consistencies. First, the size of the UAV tends to increase. This is in agreement with flight dynamics observed in nature. Smaller animals, such as insects

and small birds, have the ability to hover and use a high flapping frequency. Larger birds propel themselves forward and have a more lateral flight path. They also flap slower than smaller animals. For these vehicles, the body of the MAV is no longer is seen as an upright object but as a mostly horizontal object. This is conveyed in flight and how people perceive these vehicles. Pictures are no longer taken with the UAV standing vertically, but with the body horizontal. These UAVs are built to travel larger distances and therefore are mostly battery powered. An external power supply is simply no longer an option.

The Microbat was the first FWAV to use an onboard battery [9]. A Ni-Cd battery was used to power a small DC motor with linkage that flaps the wings simultaneously. This palm-sized FWAV weighs 12.5 grams and is capable of a 42 second flight. By adjusting the frequency of this MAV the vehicle was able to control its pitch, while adjusting the vertical rudder on the tail allowed for left and right control. Two challenges were faced in the design of the Microbat. First, the weight constraints were met for the small size of this vehicle. Going any smaller would not allow the vehicle to fly due to the requirements for power production. Second, the size and energy capacity of their battery was a huge limitation. For a UAV of this size, the only way to improve energy capacity is through battery technology. A smaller more powerful battery with a higher energy capacity is the only way to increase flight time.

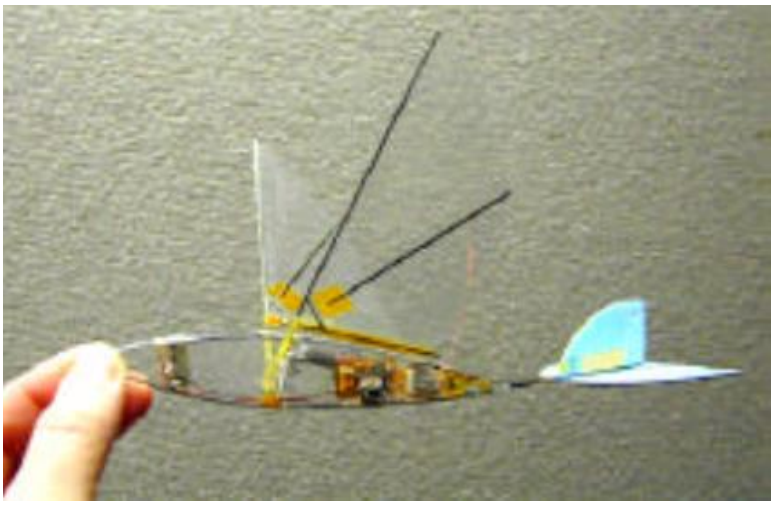

Figure 2.6: Microbat [9]

In the Netherlands, the Aerospace Software and Technologies Institute of the Technical University of Delft developed the Delfy [10]. This small UAV consisted of a DC motor that was used to drive a cranking mechanism to flap four wings. It is very similar in design to the Microbat [9].

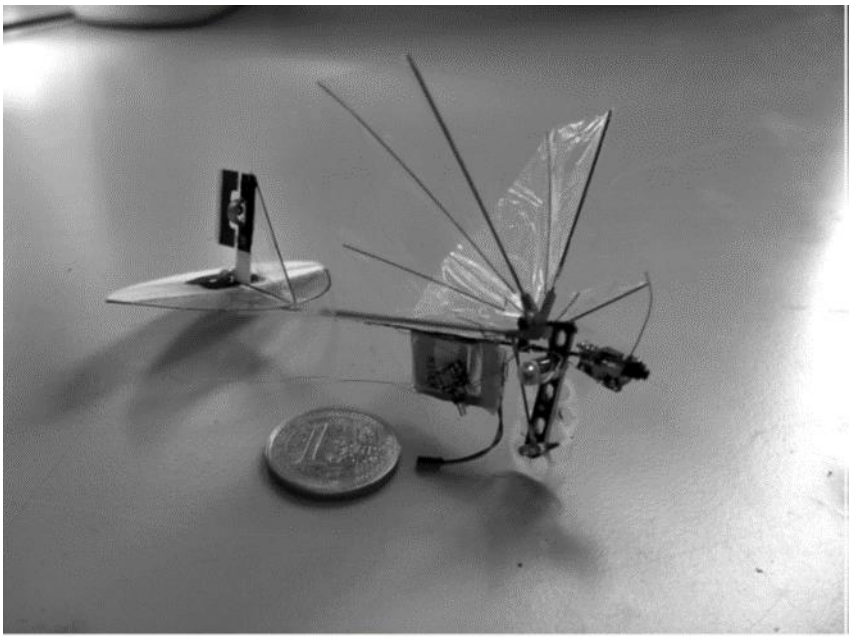

Figure 2.7: DelFly Micro next to a Euro coin [10]

The Delfly group's goal was to reduce the size of their platform as much as possible. They discovered is that was easy to reduce the physical size of their

structural components with today's manufacturing capabilities. The difficult part was reducing the weight. Components that they did not have the luxury of manufacturing such as the motor and battery could not be scaled down any further. If they were to scale down the manufactured components, the vehicle would not be able to produce enough aerodynamic force to lift the larger weight of the motor and battery. These scale-power limitations play a major factor in UAV design.

Since 2009, the University of Maryland's Advanced Manufacturing Laboratory has been designing, building, testing, and flying FWAVs [11]. Previously, the focus of these research platforms was to develop new manufacturing techniques for FWAVs, but they do serve as a stepping stone for continuing UMD UAV research. Small Bird and Big Bird are two UAVs that came out of this research effort that have very similar designs. They flap their wings with a single degree of freedom and use a horizontally moving tail for maneuverability. The wings are used to produce the aerodynamic forces necessary for lift and thrust while the tail movement controls the turning. The passive deformation of th wings is what allows it to produce enough force to achieve flight. The small bird uses a magnetic actuator as the tail driver while the big bird uses a small servo motor. Big bird weighs more and therefore is scaled up accordingly.

Figure 2.8: Small Bird [11]

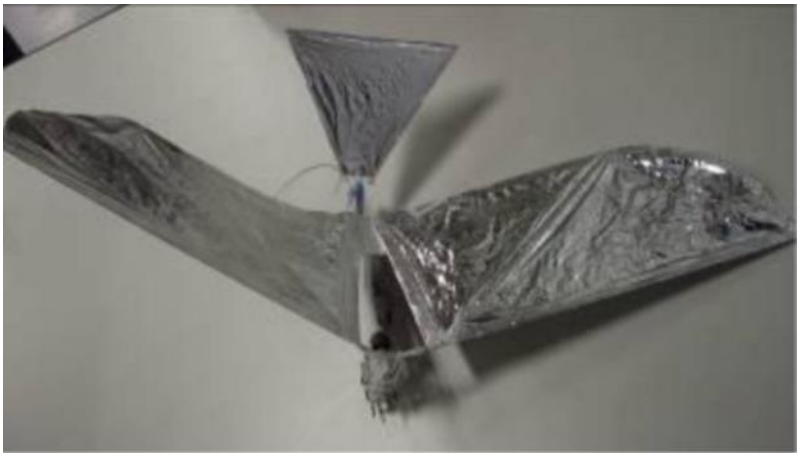

Figure 2.9: Big Bird [11]

An unconventional FWAV design was generated by the Air Force Institute of Technology in their NPS Flapping–Wing MAV [12]. This UAV uses an actuator that opens and closes in a clapping motion to move two wings at the rear of the vehicle. At the front of the vehicle is a stationary airfoil that uses simple airfoil theory to generate lift. The two rear wings are driven to generate substantial thrust. This UAV is a hybrid between a fixed wing vehicle and a flapping wing vehicle. All forces are not reliant on the flapping wing but shared among the flapping wing and airfoil structure. Although this FWAV is vastly different in design compared to the previous

FWAVs mentioned, its efficiency of this vehicle is remarkable. The NPS Flapping–Wing MAV is capable of a 15 minute continuous flight.

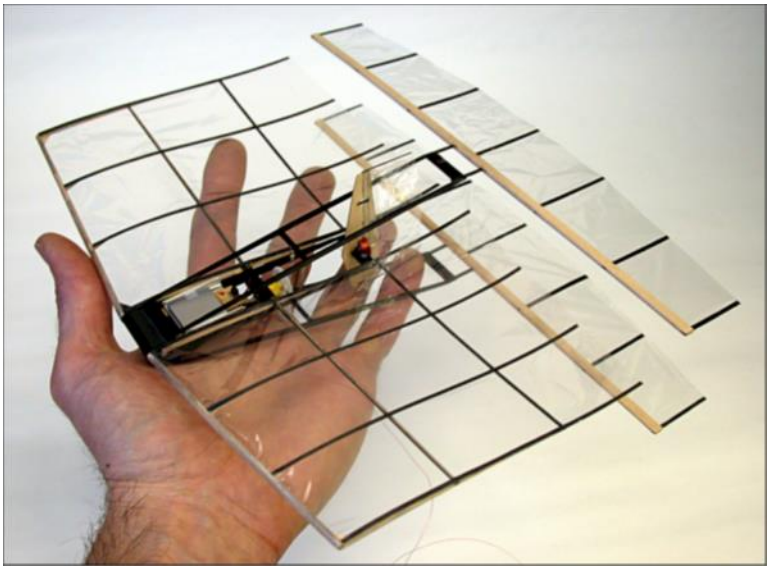

Figure 2.10: NPS Flapping-Wing MAV [12]

Typically, in nature the when comparing wingspans, the smaller wingspans are more capable of vertical flight than larger wingspans. Where insects and humming birds can simply take off vertically, larger birds need some forward movement to initiate flight. Figures 2.11 and 2.12 demonstrate just that. Based off of the power produced by available solar cell technologies (W/m^2) [45], we can begin to understand the FWAV that needs to be developed to have enough surface are for solar cell integration to power itself.

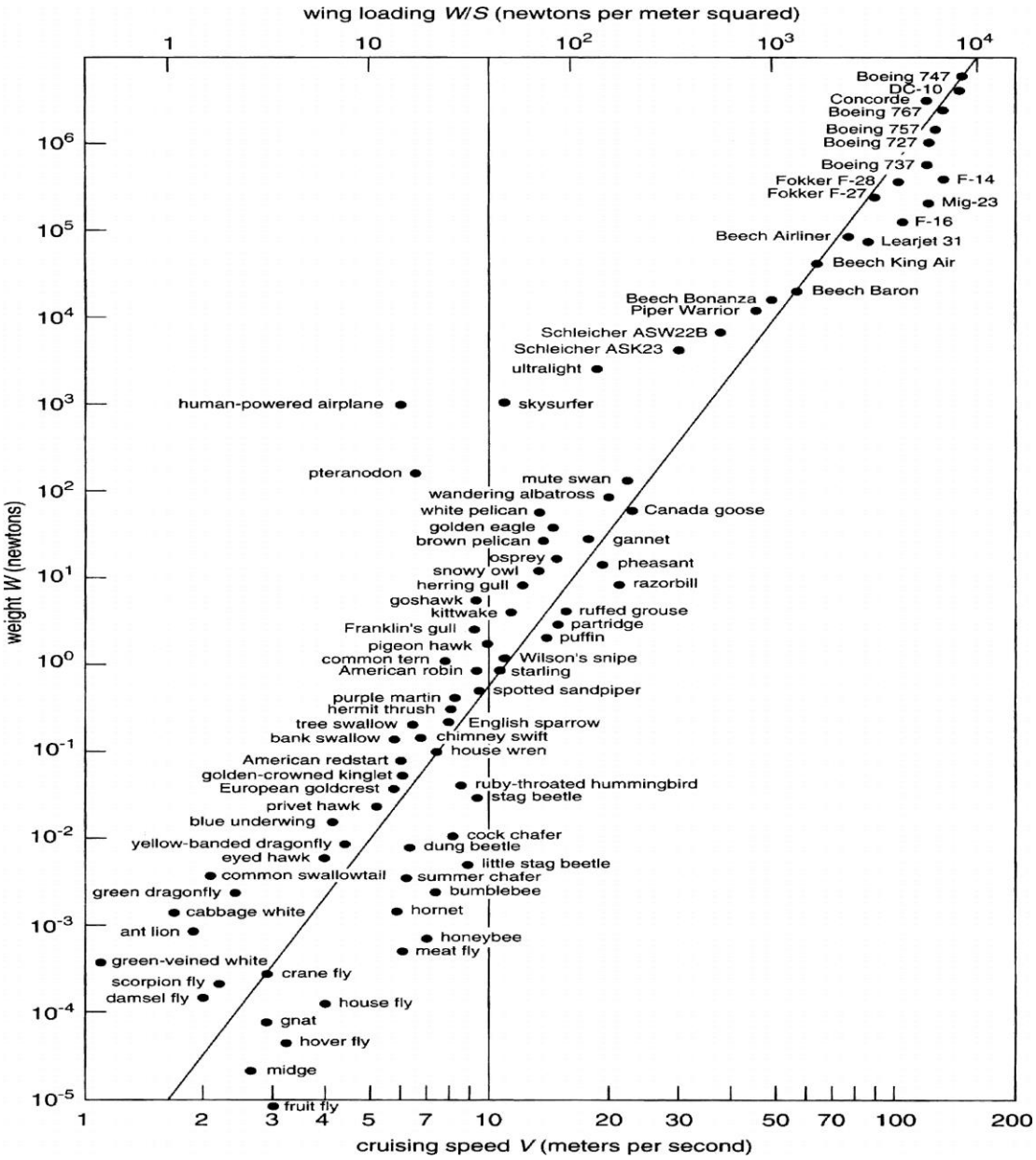

Figure 2.11: Great Flight Diagram [29]

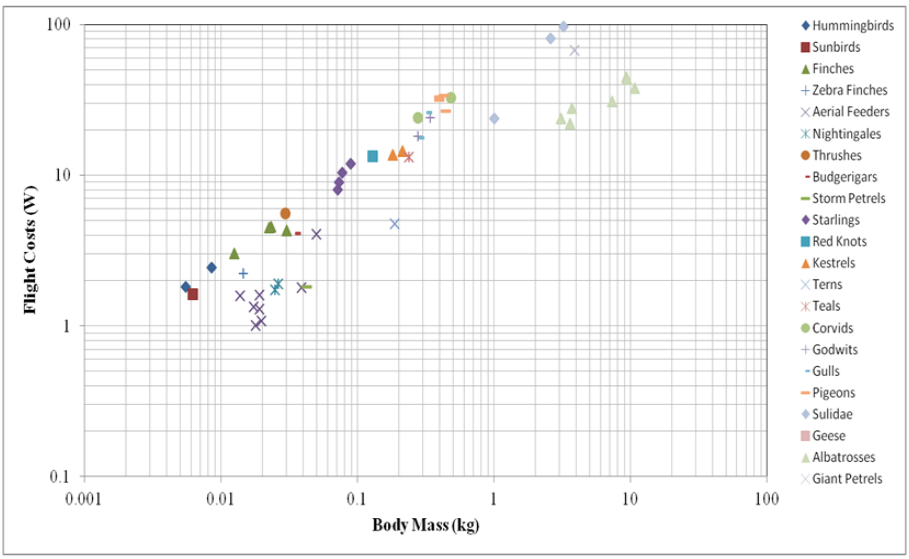

Figure 2.12: Flight Cost of Real Birds [53]

Based off of the avian inspired flight [53], we can understand the mass to power ratio of most birds. The mass to wingspan squared for birds can be observed in Figure 2.13. The power for scaling appears to follow $P = c*Mass^{(0.5685)}$ where P is the power required, and c is a fitting constant (26.83). Following this relationship and knowing the power that can be produced by current solar cell technology, we can develop a plot for the power needed vs wingspan. A small bird with a wingspan less than 0.1m simply does not have enough surface area for the solar cells to power the FWAV. This means a wingspan of at least 0.1m is needed for solar powered flight. This a already in the horiozntal flight regime as depicted in Figures 2.11 and 2.12. The wingspan needed comparable to small birds like the Red Knot to birds the size of Albatrosses.

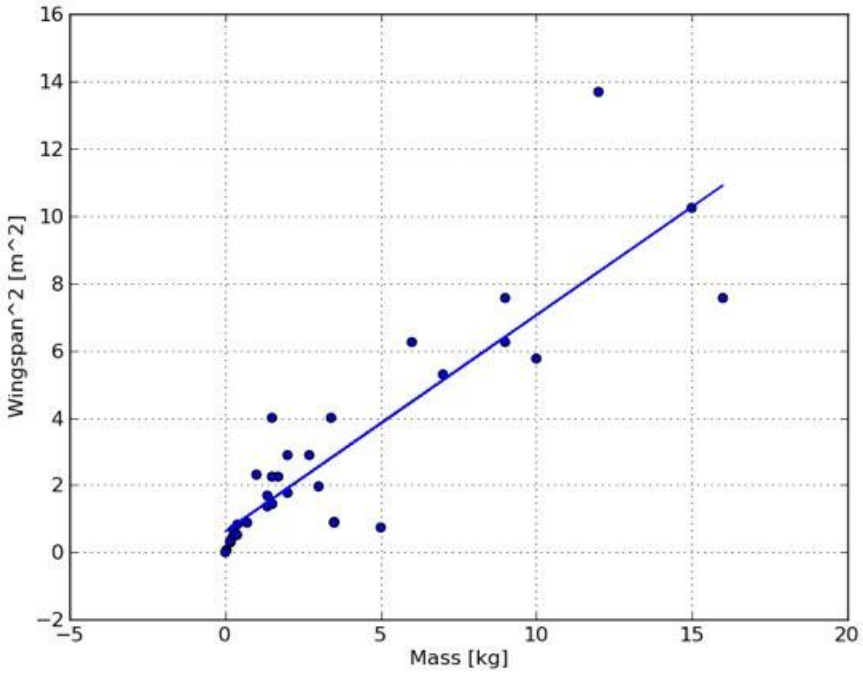

Figure 2.13: Wing Characteristics of Actual Birds [54]

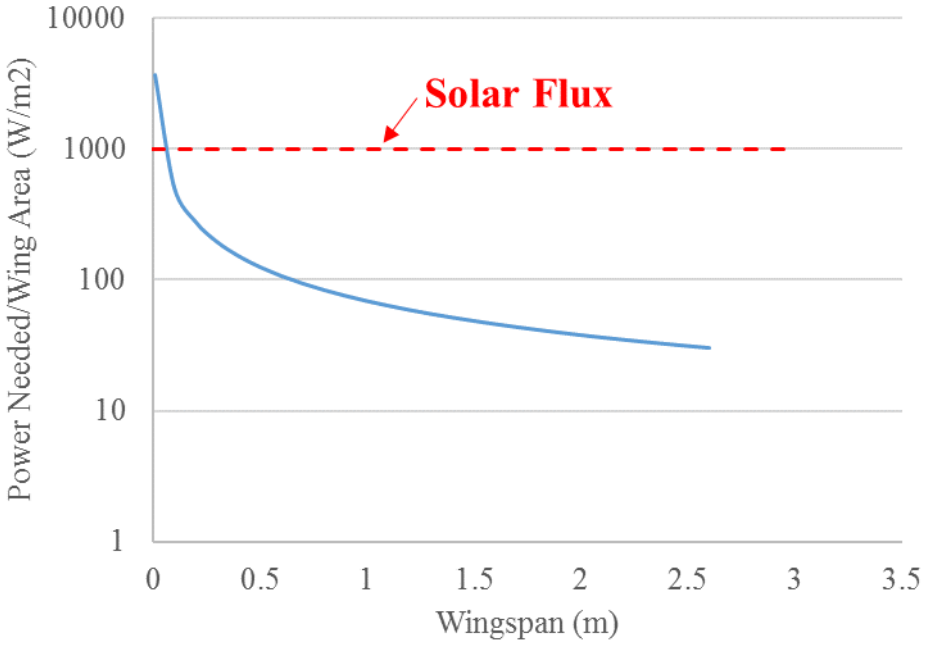

Figure 2.14: Calculated Power Needed vs Solar Flux

2.1.3 Summary of Findings in FWAV Design

This section reviewed several UAV designs to determine where the FWAV field is and where it needs areas of improvement. Clearly FWAVs have the advantage of taking on characteristics of fixed wing UAVs and rotary wing UAVs. The vehicles shown varied by design and size. Some were able to hover and some were able to cover some distance. Limitations were also observed in terms of scale and power. Current battery technology only allows these FWAVS to fly for short periods of time. The longest flight time observed was 15 minutes. There is clearly a need for more power, but a larger battery is not ideal since it adds weight to these vehicles that already have a limited payload capacity. The best solution is to harvest energy during flight. Efforts towards this idea have already been implemented in other platforms. In Virginia Tech, energy harvesting techniques have been implemented to a fixed wing UAV [13]. This UAV has cantilever vibrational harvesting modules on the wings to harvest energy from wing vibrations and small photovoltaic panels on each wing. These efforts assist the battery to have an overall longer flight time. Since the wing is fixed, these techniques are much easier to implement for their vehicle; however, for a FWAV it is much more difficult. The onboard payload capacity is much smaller and the wing must deform making integration of solar cells much more difficult.

2.2 Photovoltaic Solar Cell Technology

To effectively integrate solar cells into any UAV, a general knowledge of current photovoltaic solar cells must be acquired. In this section we review the different kinds of flexible PV cells available as well as their mechanical properties.

This review is very important because unlike fixed wing UAVs with PV cells [13]. Putting them on the wing of FWAVs can alter their flight characteristics by changing how the wing deforms.

Shah et al. made the case for flexible solar cells [14]. They showed that besides the several new application for thin film solar cell technologies, the amount of material and energy needed to continue to create the currently favored crystalline silicon solar cells will run out. Different kinds of solar cell technologies were investigated. Amorphous Silicon (a-Si), Cadmium Telluride (CdTe), and Copper Indium Gallium Selenide (CIGS) were the reported candidates. Shah et al. also touched on polycrystalline or multicrystalline silicon solar cells. These cells tend to be less stiff than their monocrystalline counterparts but are less efficient. These are commercially available with an efficiency of 17-18%. Commercially available solar cells of A-Si were reported to be between 4-8% efficient, were some laboratory samples reported a record efficiency of 13%. Commercially available samples of CdTe cells were reported to have 16% efficiencies. Finally, commercially available samples of CIGS were found to have 18.8 % efficiency. However, the market for CIGS solar cells and CdTe Solar cells has dried up. Since this study was performed a new thin film photovoltaic solar cell technology has emerged. Gallium Arsenide (GaAs) photovoltaic solar cell have become the newest most efficient solar cell technology. GaAs solar cells are normally 28% efficient [44], surpassing even monocrystalline technology. AltaDevices recently commercialized a 28.8% efficiency GaAs cell and MicroLink Devices a 31% efficient CIGS cell. In terms of tin-film solar cell efficiency, GaAs cells are the best choice. However,

In choosing the best PV cell for our application other factors besides efficiency must be observed. The mechanical substrate that the PV material is deposited on plays a major role in wing deformation and weight. This eliminates CdTe cells since their substrate is limited to rigid glass [15]. Cost is another major aspect that determines which type of PV cell we can obtain. A-Si and polycrystalline solar cells are relatively cheap compared to the CIGS or GaAs cells. This is due to the difficulty in the manufacturing process for A-Si cell compared to the CIGS and GaAs cells. When we need a high quantity of solar cells and can afford to not worry about efficiency, A-Si PV cells are the best choice. However, to really stretch the electrical capability of the system, GaAs PV cells are the best yet much more expensive.

To integrate these cells into the wings of an UAV, the mechanical properties of these cells must be known. This data serves as the basis for predictions of mechanical failure and efficiency loss under more complex loading situations like ours. Antartis et al. investigated the residual stress and mechanical properties in A-Si PV thin films [16]. They found that the performance of the PV cells was found to be unaffected after 100 loading cycles at up to 0.3% strain. However, degradation occurred when the cells were gradually loaded to 1% strain. It was found that the buckling stress of the A-Si cell measured was (-114 ± 27) MPa and the mean residual stress was (-661 ± 93) MPa. This results in a maximum allowable strain of 0.1 ± 0.02% for the entire cell. In Blakers et al. they use bending equations to determine the minimum survivable radius (ρ) for a curved piece of A-Si cells.

$$\rho = \frac{Ex}{\sigma}$$

Where E is the modulus of Elasticity (168 GPa), x is the half thickness of the piece of silicon, and σ is the tensile yield strength (7.0 GPa). Depending on the thickness of the cells we obtain, we can safely bend them as along as we do not reach the minimum curvature necessary to cause damage to the solar cells.

2.3 Multifunctional Design

By integrating PV solar cells into the various functional structures of an UAV, we are implementing multifunctional design. Multifunctional structures combine multiple functional requirements into a single structural component to create better efficiency in the overall design. Multifunctional design has already been used in biologically inspired technologies for electromagnetic functionality, heating functionality, healing functionality, and sensing functionality [17]. Multifunctional structures can be used in miniaturization [18], which is an important concept in current MAV design. As we have already seen out of the group from VA Tech [13]. The wings are also being used to harvest both solar and vibrational energy on a fixed-wing vehicle.

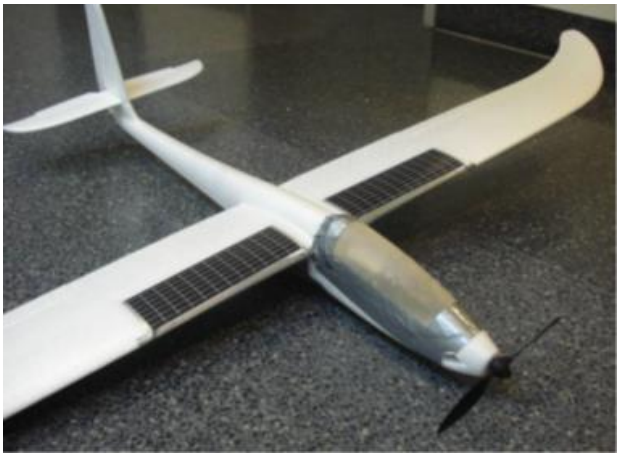

Figure 2.15: Fixed wing vehicle with vibrational harvesting capability as well as solar harvesting capability [13]

Another multifunctional UAV consists of integrating the actual batteries into the wings of a fixed wing UAV [19, 20]. For this vehicle, the batteries were actually integrated into the wing and assist the structure in making an airfoil shape to generate lift for the aircraft. This UAV was propeller driven.

Figure 2.16: UAV with batteries integrated into the wing [19, 20]

Multifunctional structures have been used in FWAVs as well. In the Department of Mechanical & Electromechanical Engineering at Tamkang University, researchers are using a polyvinylidene fluoride (PVDF) skin on the wings for self sensing [21, 22]. Although this FWAV does not fly, it plays a critical role in determining how wing deformation characteristics correlate to force generation. Some self-sensing multifunctional work was also done on the MFI platform [4]. Strain gauges were placed along the spar components of the wings to observe strains during the flapping motion. At the University of Maryland, elastomeric strain gauges

were painted onto the surface of the wings of a UAV. A correlation was found between the strains observed and thrust production [23].

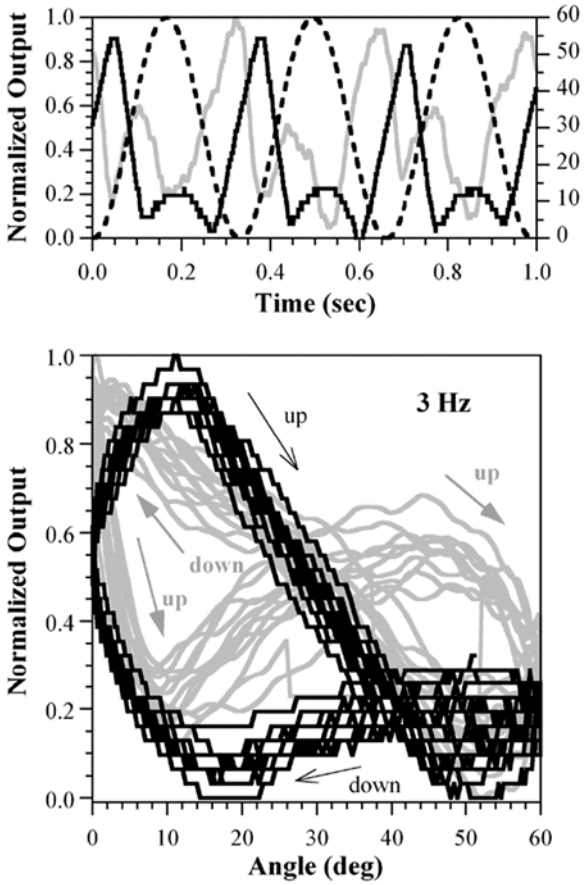

Figure 2.17: Sensing results showing a correlation between thrust (grey) and strain (black) on a FWUAV Top) Time Resolved, Bottom) Angular Position of the Wing [23]

Multifunctional design has the ability to make current designs more efficient by freeing up volumetric space and allowing for more payload. Integrating more than one functionality into existing structures is beneficial, however, one must always worry about how the integration will affect overall performance. If the change in performance in minimal, then adding another functionality to an existing structure is beneficial. An acceptable multifunctional design should minimize the effects that any additional integrated function has on the existing performance.

Oh et al. [52] also used multifunctional structures on a FWAV. A vertical based flight FWAV was developed that had a thin film membrane that had an antenna integrated. The actual flight performance was not observed, but the capabilities of the antenna and performance of the antenna were measured. This is simply another example of a multifunctional effort for FWAVs.

2.4 Force Measurement Techniques

To evaluate how changes in design affect vehicle performance, the lift and thrust forces generated by the vehicle should be measured before and after design changes are made. Similar methods of extracting this data can be observed throughout the field. In the case where a 1 degree of freedom (DOF) load cell is used, there are two basic ways to extract the forces. The first method requires only aerodynamic lift to be measured [21, 22]. A wind tunnel is set to the exact speed of forward velocity of the UAV. This is accomplished when the average thrust value equals zero. The only force that should be generated by the flapping UAV is aerodynamic lift force. The load cell is set vertically and the aerodynamic lift can be recorded.

Another way that a 1 DOF load cell can be used to measure aerodynamic lift and thrust forces is to run two tests separately. This is the method used at UMD for many years [11, 23, 24, 25, and 26]. The aerodynamic thrust forces were measured with the UAVs wings parallel to the wind direction with the UAV pointed towards the wind. A load cell is attached to a linear air bearing and the resulting forces generating during operation are measured and recorded.

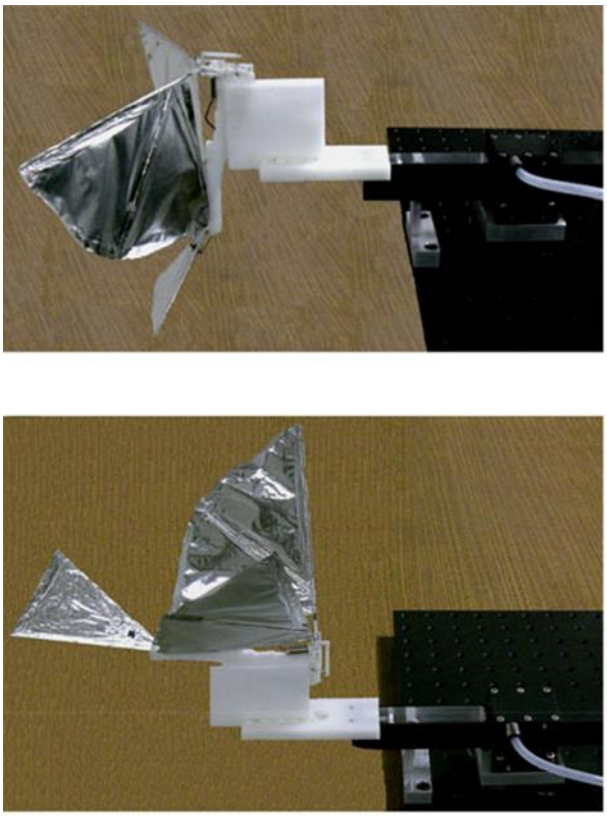

Figure 2.18: Load cell test configurations for early UMD UAVs Top) Lift Bottom) Thrust [25]

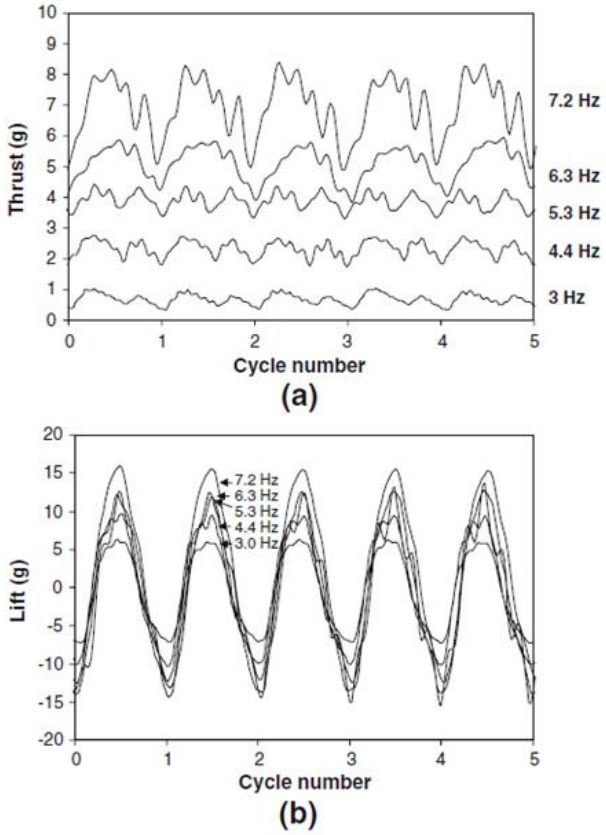

Figure 2.19: a) Thrust response from load cell b) Lift response from load cell [25]

The lift forces are measured similarly. For lift the orientation of the UAV on the test stand is changed so that the load cell can measure aerodynamic lift. The test stand is also placed in the wind tunnel at an alternate angle so that the UAV is still facing the direction the wind is coming from. Again since these are two separate tests the aerodynamic lift and thrust forces cannot be measured and recorded simultaneously. However, this method does not require that the wind tunnel be set to the exact forward velocity of the UAV.

A much more straightforward and easier way to obtain the aerodynamic forces generated by a UAV is to use a 2 DOF load cell [9]. This enables both lift and thrust forces to be measured and recorded simultaneously. The last way to extract the most amount of information about flight dynamics is to use a 6 DOF force transducer like

in Wright State University [27]. This enables the researcher to study lift, thrust, yaw, and the moments generated by different UAV designs.

Being able to quantify the difference in force generation by altering wing, tail and body designs will become a paramount aspect of this work. A consistent and accurate test stand and wind tunnel are critical components in getting accurate and comparable results.

2.5 Digital Image Correlation Techniques

An important aspect that should be quantified to further understand FWAV flight dynamics is wing deformation during the flapping cycle. The wings of most FWAV go through passive deformation while flapping. The passive deformation is responsible for generating the forces necessary for flight. Further understanding of wing deformation and wing shape will encourage better wing design and development of a wing model that allows performance to be predicted. Past attempts have been used to extract the wing shape during the flapping cycle. Previously two high speed cameras were used to track fifteen points on a wing surface [26]. This is a very tedious way to collect the wing shape since it involves someone going through and measuring the displacements one by one for each picture. It is also prone to error since an individual is making the measurements.

In Wu et al., three dimensional Digital Image Correlation (DIC) was used to track the wing deformation through the flapping cycle [28]. 3D DIC uses a system of at least two cameras to track the surface of a deforming body.

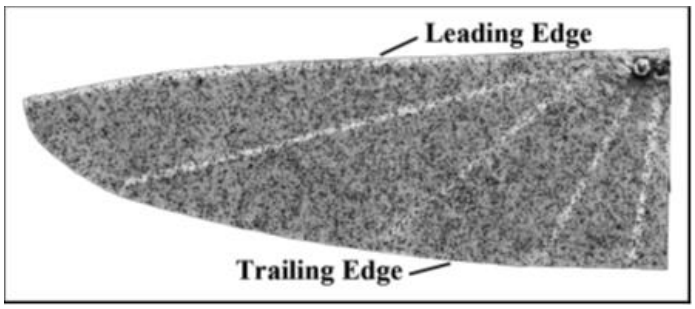

Figure 2.20: Speckled wing used for 3D DIC [28]

The surface being observed is painted with a speckled pattern to allow the cameras to track up to thousands of points throughout the surface. Pictures of the deforming speckled wing were taken simultaneously with 4 cameras. The images are processed using a DIC software. This software tracks the speckles in relationship to each other in 3D space and determines how much the wing has deformed in 3D space. From this information strains along the wing surface can also be determined. However, in this case, all that was observed were the contours of the wings during the flapping cycle.

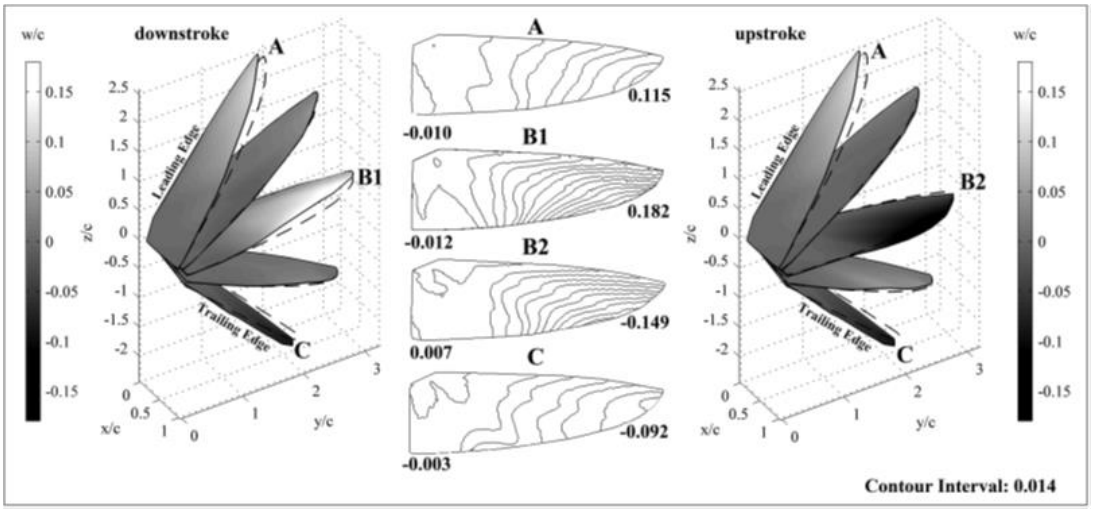

Figure 2.21: Wing contours while flapping [28]

DIC is an important tool used in this work to determine how altering wing designs changes the shape of the wings during the flapping cycle. Using this data, knowledge can be gained that allows a predictive model for wing performance to be

made based on how the wing is expected to deform. This shows a better understanding of wing dynamics and wing design for FWAVs.

2.6 Efforts in Modeling

Pines et al. describes the challenges faced in future MAV/UAV development [29]. One major challenge is the lack of models for MAV/UAV flight behavior. A major contribution to the field would be general models that enable UAV designers to anticipate how the UAV will behave under flight conditions. FWAV design is different in that wing design has a huge impact on flight performance. The generic airfoil model will not work for these dynamic structures. However, previous papers and findings can lead us to developing a model for FWUAVs.

Generally it has been found that different UAV sizes will encounter different Reynold's Numbers [30]. Smaller UAVs will encounter higher Reynold's number requiring them to flap faster. Larger UAVs will encounter smaller Reynold's numbers allowing them to flap slower yet still obtain flight. This is reminiscent of behavior and patterns in nature.

From work done at the Micro level, we know that Leading Edge Vortices (LEVs) play a role in enabling small insects to fly [31, 32]. Under general aerodynamic theory, small insect with large thoraxes should not be able to fly; however, through LEVs on surface of rapidly moving wings, these animals are able to fly. The small insect like MAVs take advantage of this as well.

The rotation of the leading spar also plays a role in wing dynamics. For insect-like flight with front wing rotation [3], the ability for the front spar to rotate during the flapping cycle correlated well with lift generation. This enables us to

extend traditional translation based wing models since rotation plays also plays a role in force generation.

Wing stiffness also plays a role in flight dynamics [33]. A wing that is too stiff will not deform enough to generate lift; whereas, a wing that is not stiff enough will not push the air through the wing in a direction to generate thrust. A balance in stiffness is critical in flight dynamics.

Using PVDF sensors on the wings showed a correlation between wing deformation and lift [21, 22]. Using smaller strain gauges on the wing spars correlated the strains to thrust measurements [23]. A better understanding of wing shape and kinematics can help to model wing behavior through deformation.

These findings all come from observations of wing dynamics. Putting these factors together can help derive a model that will enable designers to mathematically predict how a wing will perform before it is even built. Development of such a model will lead to a better understanding of FWAV design.

2.7 Summary of Literature Review

This literature review demonstrates the need for the proposed work. Section 2.1 demonstrates the need for more electrical power from these UAVs. With the maximum flight time currently at 15min, and the limitations imposed by the payload capacities of these vehicles, solar cell integration is needed for more power generation. Section 2.2 highlights the benefits A-Si and GaAs PV solar cells. Section 2.3 introduces multifunctional design and the anticipated effects that solar cell integration will have in vehicle performance. Sections 2.4 and 2.5 investigate data collecting techniques using load cells and DIC. Section 2.6 introduces the need

for UAV models to help predict how changes in design will effect flight performance. Through the integration of solar cells, the need for more power can be met, but the cost in overall performance needs to be understood. This work serves as a trade-off analysis for this issue. Through this investigation, more knowledge towards FWAV behavior is gained allowing for models to be derived that enable performance to be predicted based off of changes in vehicle design.

Chapter 3: Design and Manufacturing of Robo Raven

In this chapter, a new FWAV named Robo Raven is introduced. This vehicle was designed and manufactured in the Advanced Manufacturing Laboratory at the University of Maryland. This is the base platform used for solar cell integration. It is an ideal candidate thanks to a wingspan of over 1 meter that provides a large surface area for PV solar cells. The following is an overview of the development of Robo Raven and its characteristics. This content of this chapter is presented similarly to what was published in *Soft Robotics* [38]

3.1 Introduction

There was high interest in developing a platform that can be used to investigate outdoor aerobatics maneuvers, so inspiration was taken from the Common Raven, a relatively large bird capable of aerobatics. Moreover, to provide customizable flapping motions, each wing was powered with a separately controlled independent drive train, consisting of a motor, gears, position sensor, and feedback control loop. The benefit of this approach is to allow completely arbitrary wing motions, which provides increased freedom to explore some aggressive and interesting maneuvers. These include asymmetric roll initiation, upflap-downflap asymmetry, gliding and soaring dynamics, gust rejection, and blending of tail and wing steering modes.

In the present effort, many of the same techniques previously developed to characterize and understand changes in wing design are applied. The results culminate in a flying prototype vehicle called Robo Raven, a FWAV that overcomes the substantial challenge of producing sufficient lift and thrust for sustained flight

with fully independent wing control. This newly designed FWAV has a larger wing surface area making it a great candidate for solar cell integration.

3.2 System Overview

3.2.1 Design Requirements

The primary objective was to build a FWAV that can be used to learn about the effects of changing wing kinematics while improving the maneuverability of flapping wing air vehicles outdoors. Since nature provides the best examples of flight it was sought to replicate avian-based flight dynamics. This effort was inspired by the Common Raven, Corvus Corax, with properties listed in Table 3.1.

Table 3.1: Properties of the Common Raven, Corvus Corax

Parameter	Common Raven	Unit
Total Mass	0.69-2.00	kg
Length	0.63	m
Wingspan	1.00-1.50	m
Average Chord	0.21	m
Aspect Ratio	2.77	
Flight Speed	9.80-12.50	m/s

For vehicle design, the following eight requirements were identified:

1. Flap wings of at least $0.20m^2$ surface area at 3.5 Hz. This requirement came by observing raven wings and was necessary to enable outdoor flight.
2. Flap each wing independently with the ability to synchronize wing motions when needed. This requirement was needed to perform normal flight and do aerobatics.
3. Have ability to program wing velocity and position as a function of time. This requirement was needed to optimize normal and aerobatic maneuvers.
4. Minimize weight to achieve flight and a climb rate of 0.5m/s.

5. Achieve minimum turning radius of 10m. This requirement was needed to conduct tests in indoor stadiums and fly in outdoor fields with trees.

6. Remotely control the flight from a distance of 500m.

7. Land unpowered at glide speed from a height of at least 3m without sustaining structural damage.

3.2.2 System Decomposition

The design requirements for Robo Raven assisted in determining how to control and power the entire system. A functional decomposition that demonstrates the energy and signal flow through the system was developed. This allowed for the individual components that were going to be needed for the system to be selected.

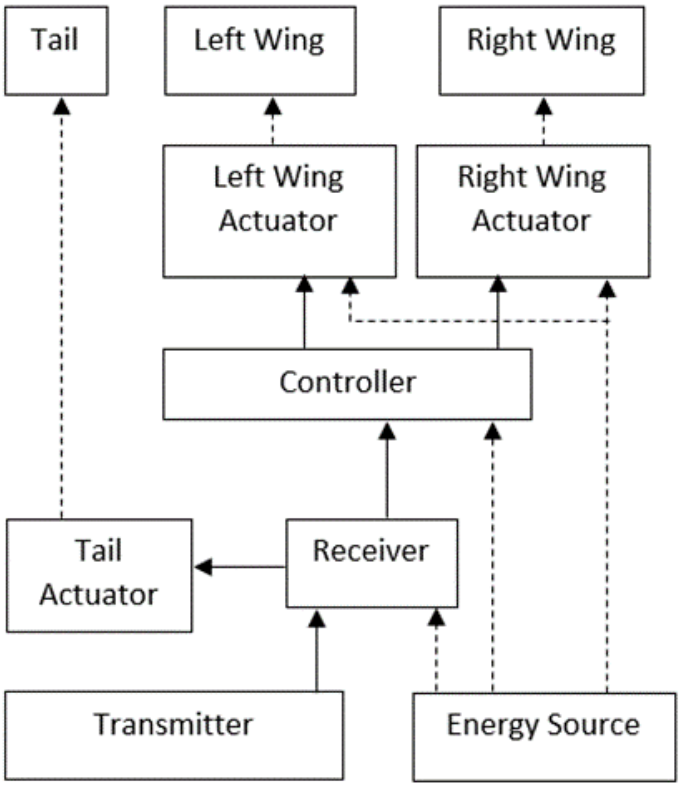

Figure 3.1: Functional Decomposition of Robo Raven: dotted lines (- - -) denote energy flows and solid lines (—) denote signal flows

Each component that was selected was the lightest component that was commercially available. This would allow for maximum payload capacity when the vehicle is completely assembled. Additionally, each component was chosen for its small size. This allows for easier mounting on the fuselage of the UAV. A breakdown of the components and weights are shown below.

Table 3.2: Weight breakdown of Robo Raven for electronics, frame, wings, tail, and total

Component	Weight (g)
Drive Actuators (2 - Futaba S9352HV)	136.0
Tail Actuator (Futaba S3114)	7.8
Controller (Arduino Nano)	6.0
Wiring	19.8
LiPo Battery	27.0
Spektrum 2.4 GHz Receiver	3.0
Wings (2)	26.0
Tail	8.0
Actuator Mount Assembly (for the S9352HV servos)	16.4
Frame	30.0
Foam Crash Protection	5.0
Assembly Fasteners	5.3
Total	**290.3**

3.3 Design and Fabrication of Wings

3.3.1 Wing Design

Wing design was adapted from a previously used approach developed for successfully realizing a FWAV platform with synchronized wing motion, which has been shown to be effective in generating lift and thrust forces across a variety of applications and size scales [11, 23, & 24]. The design is shown in Figure 3.2.

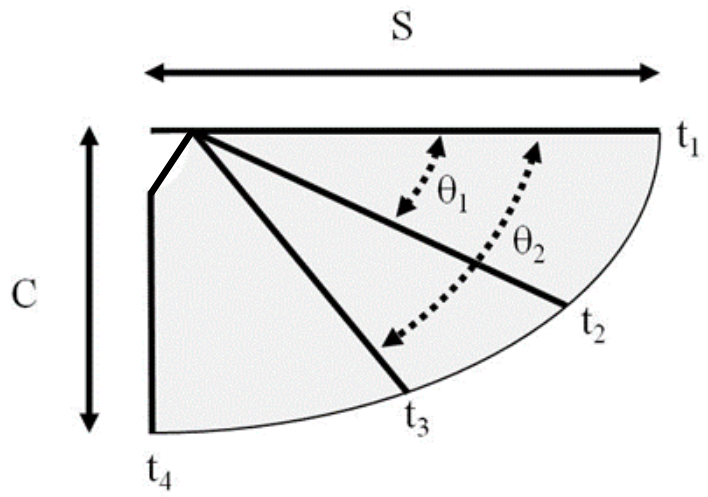

Figure 3.2: Characteristic wing design: S is the semi-span, C is the chord, and t_n are the diameters of carbon fiber stiffening rods

The parameters of the wing are as follows: S is the semi-span, C is the chord, and t_n are the diameters of carbon fiber stiffening rods. The wing membrane is a 0.0254mm thick film of biaxially-oriented polyethylene terephthalate (Mylar) which provides light weight, flexibility, and good toughness.

Due to extensive usage of lightweight materials, this wing design changes shape passively in response to loads from the flapping motion. As the wings flap, aerodynamic loads on the compliant wing surface generate a significant camber change. The cambered wing is a thin airfoil, which captures and expels a large volume of air with each stroke. The induced shape change alternates with upstroke and downstroke producing lift and thrust. Thus, the selection of parameters in Figure 3.2 plays a major role generating the aerodynamic loads.

3.3.2 Experimental Wing Design Procedure

To identify the best wing design for this new vehicle, a series of experiments with different wings were conducted to help characterize this design. The objective of this experimental wing characterization was to select a wing geometry that would

result in the servos operating as close as possible to their peak power operating condition. Each wing design was evaluated using a custom-built test stand with a 6 degree of freedom load cell in a wind tunnel to measure the forces generated by the vehicle. This test stand was mostly made of wood. It was deigned to keep the FWAV at a pitch of 20 degrees, which was the angle taken by the vehicle during flight. An aluminum slab separated the load cell from the rest of the test stand providing a smooth flat surface for accurate results. The load cell used was an ATI Mini 40 Force Transducer, capable of measuring a maximum load of 40 N for thrust with a resolution of 1/100 N and a maximum load of 120 N for lift with a resolution of 1/50 N. A National Instruments PXI system was used to measure voltages from the load cell during wind tunnel testing, and these voltages were post-processed to obtain the lift and thrust forces.

High speed video footage was recorded during all load cell tests to visually observe the difference in flapping for each wing design. These tests were repeated under no air flow and significant air flow conditions with varying angles of attack. The load cell testing quantitatively revealed which wing created the most lift and thrust, while high speed video footage offered qualitative explanations for the results and provided design insight. The test stand is shown in Figure 3.3. The load cell testing quantitatively revealed which wing created the most lift and thrust.

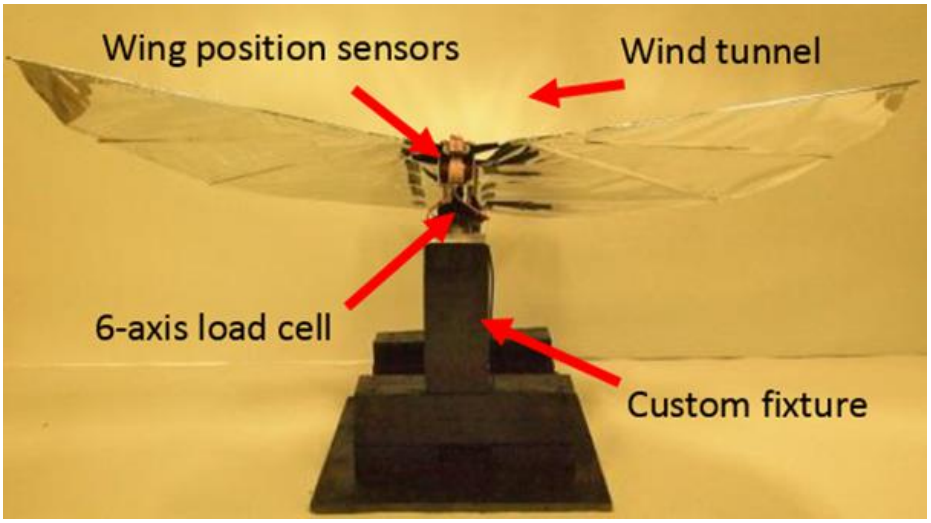

Figure 3.3: Custom built test stand fixture with 6 DOF load cell in the wind tunnel

3.3.3 Characterization of the Selected Wing Design

Each of the experimentally designed wings were built by hand using a template matching the parameters in Table 3.3. The Mylar membrane was taped flat on a clean flat table and carbon fiber tubes were installed according to the template using Uhu Por glue. Mylar strips were then used to cover and secure the carbon fiber stiffeners on the wing's membrane, and additional reinforcement Mylar was bonded to areas of higher stress concentrations to prevent tearing. Five holes were melted into the wing next to the chord-wise spar and 5 rubber bands were tied through for tensioning the wing attachment to the frame. A completed wing can be seen in Figure 3.4.

Table 3.3: Wing Design Parameters

Parameter	Value	Units
S	605.8	mm
C	362.0	mm
t_1	3.18	mm
t_2	1.63	mm
t_3	1.63	mm
t_4	1.63	mm
θ_1	20	degrees
θ_2	40	degrees

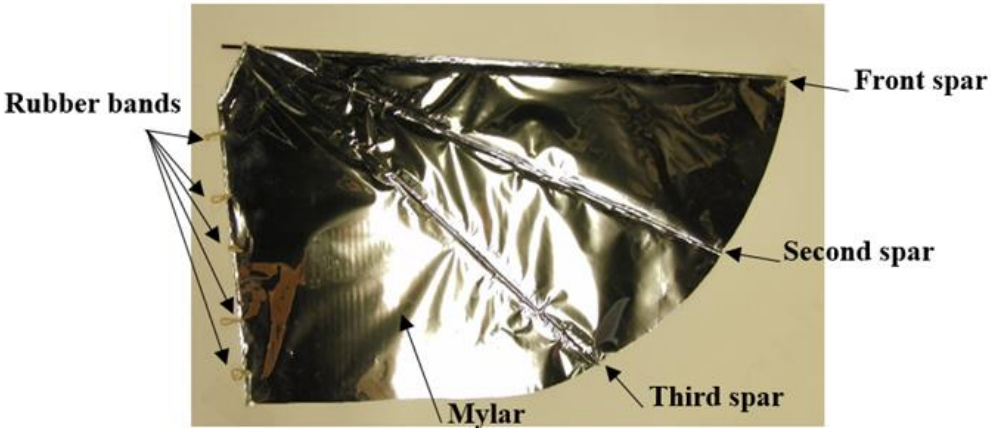

Figure 3.4: Completed wing with geometry defined by Table 3.3

These wings were tested in a wind tunnel (airspeed approximately 5 m/s) using the load cell test stand. The wings generated averages of 243 g of lift and 120 g of thrust at a 20 degree angle of attack. Lift and residual thrust data as a function of time from a sample trial are shown in Figure 3.5.

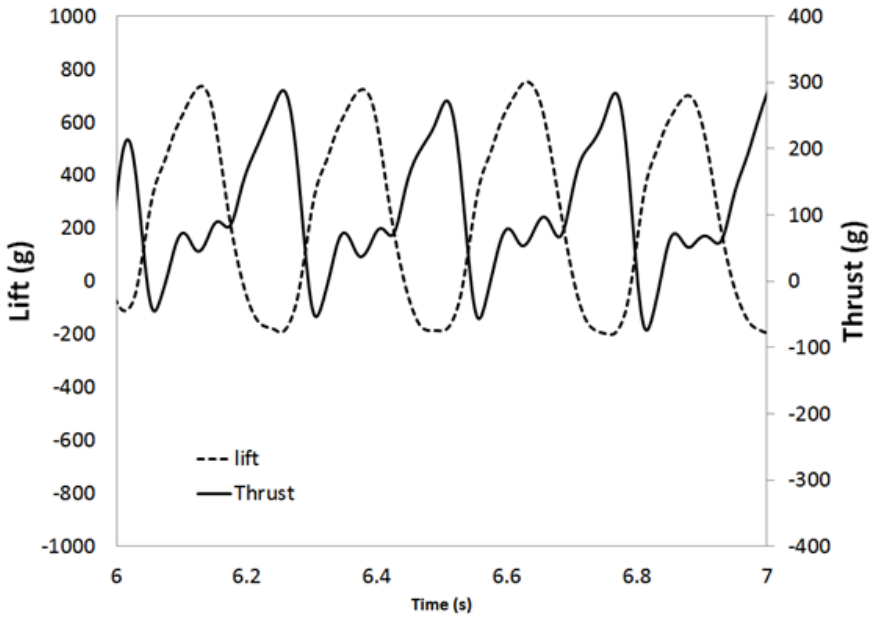

Figure 3.5: Lift and thrust production during multiple flapping cycles

It is important to note that the response of these wings is similar to the response of previously developed FWAVs [25]. The lift demonstrated a smooth almost sinusoidal response where the thrust was more complex. There are several peaks within one flapping cycle. In this case, there are two different magnitudes demonstrating the difference in magnitude in thrust produced in the up and downstroke at an incline of 20 degrees.

3.4 Design and Fabrication of Wing Drive Subsystem

The wing drive subsystem is responsible for producing the wingbeat kinematics that result in lift and thrust. The design of this subsystem is an important aspect of the vehicle design. Therefore, nature was used for inspiration and provided some insight into the trends that exist among feasible designs.

Power density is a key design factor for FWAVs to ensure lift and thrust forces are sufficient to overcome the weight and drag of the vehicle. The design of custom actuators was beyond the scope of this effort, so commercially available

actuator for the wing drive subsystem were selected. Vehicle size limited the selection to the slower and more powerful actuators, including electric motors, shape memory alloys, bimetal benders, and dielectric elastomers. Of these choices, only electric motors and dielectric elastomers offer acceptably high efficiency of operation. However, the very high operating voltage presents integration challenges and required additional voltage step-up electronics on-board. Therefore, electric motors were used for this application.

Electric motors must be paired with a flapping mechanism to provide reasonable speeds of operation. In addition, integration with a position sensor and a feedback loop is required for programmable kinematics. These requirements lead to increased weight, part count, complexity, and integration difficulty. To avoid the challenges associated with matching all of those components and designing the required hardware and software, servos were chosen for this effort to actuate the wings, due to their high power output, programmable motions, and integrated packaging including the motor, drive train, speed controller, and position sensor. The Futaba S9352HV was chosen due to its high figure of merit, computed as the power output divided by the mass. The available servos exhibit a linear relationship between available power and figure of merit. While other servos exist on the market that offer either higher torque, higher speed, or lower mass, none are sufficiently strong performers in all three categories to justify their selection for our efforts.

The Futaba S9352HV servo motors were tested with a dynamometer and power analyzer to provide details about the electrical power input as well as the mechanical power output. The test results included the power and efficiency curves as

a function of motor speed. The objective was to determine the location of the power band, the operating condition that provided peak power output, and the operating condition that provided peak efficiency. The results of our testing are summarized in Table 3.4. The maximum torque and speed are not reachable simultaneously. The peak power output of 9.4 W is reached at a final drive speed of about 509.9 deg/s which corresponds to approximately half the peak torque and speed.

Table 3.4: Performance Test Results for Futaba S9352HV

Parameter	**Value**	**Units**
Stall Torque	12.5	mN-m
Top Speed	1008.4	deg/s
Peak Power Output	9.4	Watts
Peak Efficiency	63.9	%
Mass	72.0	g

Due to the importance of weight minimization, 3D printing was used to manufacture the frame that comprised the primary structure of the vehicle. The ability to produce a part with complex geometry eliminated many assembly steps and hardware that would have otherwise been required. The frame was sized to minimize the weight and to ensure that it was capable of withstanding the expected load. The part is manufactured using ULTEM 9085 material, which has a tensile strength of 71.6 MPa. The design has substantially less stress than this during normal operation. Iterative testing has shown that crashes imparting loads of over 5 kg can be survived without part failure, yet the weight of the final part is only 8.0 grams.

The custom servo horns were laser cut out of 1/4” Delrin®. These servo horns fit over aluminum servo horns that physically attach to the servos and have 1/8” holes

for the wings' front spars to fit into. To prevent off-axis loads from damaging the gear train inside each servo as well as to provide crash protection, a stiff 3D printed nose is attached to the front, labeled Torque Lock in Figure 3.6. Carbon fiber tubes are used to connect the front section to the tail and the rest of the body. An exploded view of the CAD model of the main drive system is shown in Figure 3.6.

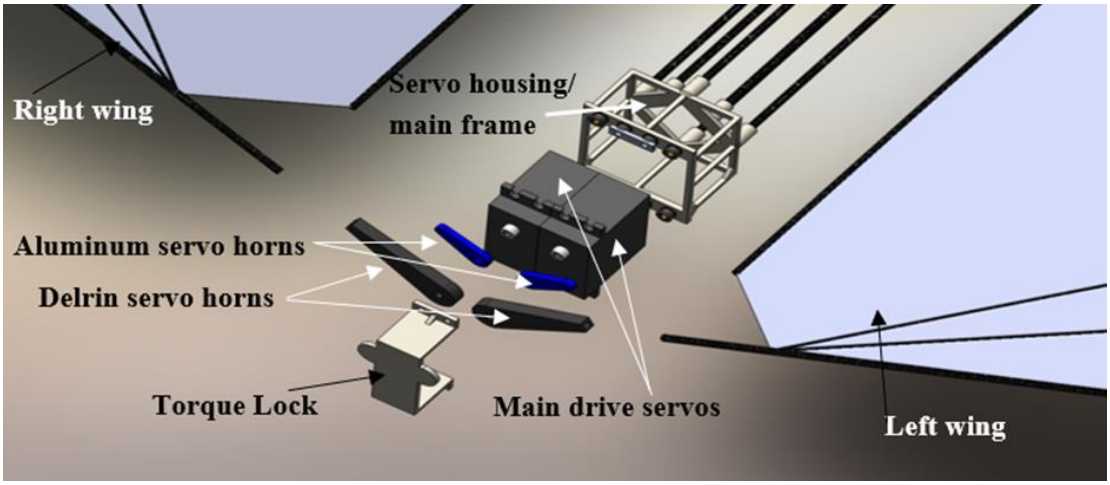

Figure 3.6: Main drive assembly (exploded view)

3.5 Design and Fabrication of Steering Subsystem

A steering system consisting of a tail surface mounted to the rear of the fuselage was included to control the direction of the FWAV during flight. The tail maintains a fixed elevator angle while providing a variable roll angle relative to the fuselage. A flat trailing edge allows for simplified manufacturing and is also an aerodynamically ideal solution. Any portion of the tail that contracts in span will be subject to the upstream wake and produce primarily drag, with a minimal contribution to lift.

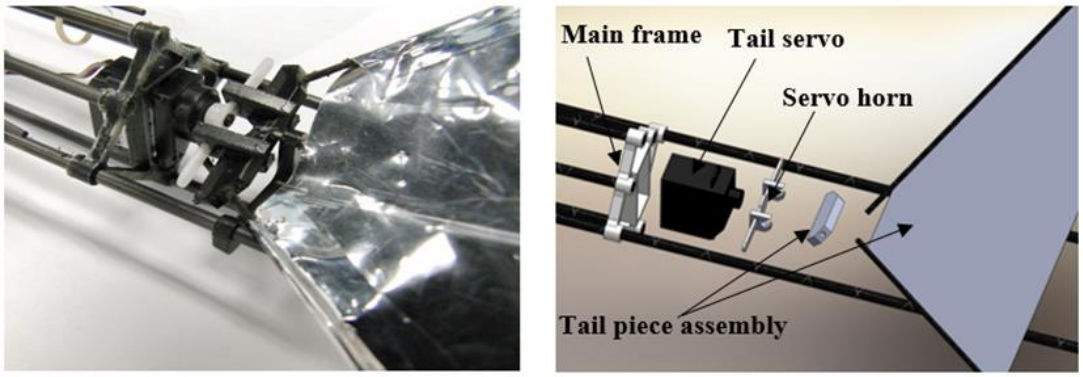

Figure 3.7: Tail drive subsystem assembled (left) and exploded view (right)

This design provides the option of fully controlling the steering with the tail alone, or blending the steering control with wing motions to explore bio-inspired techniques of flight control. This enables the operator to execute aggressive maneuvers. In addition, this layout gives us the ability to explore some behaviors that would be challenging or impossible to train an animal to execute, yet could still be informative from a research perspective. Flight testing of this design revealed a minimum turn radius of 6 m at a 40 degree tail angle, with an almost linear increase in turn radius proportional to reduced tail deflection.

3.6 Design and Evaluation of Normal Flapping Gaits

The selection of a flapping gait simultaneously controls the selection of a number of important parameters including the flapping amplitude, rate, average dihedral, and periodic symmetry, among others. All of these parameters affect the flight speed and body pose, which significantly influence the forces produced during flight. At a minimum, our objective with the Robo Raven would be to reach the point that corresponds to minimum power required to sustain flight, and thus provides the greatest endurance.

The prototype vehicle shown in Figure 3.8 was used for flight testing. Initially, the angle of attack required adjustment, as early flights exhibited a very high forward speed and gradual loss of altitude. This was likely due to the large concentration of weight at the front attributed to the servos. Therefore, a small extension was added to the rear of the fuselage from which the battery was suspended, which shifted the center of mass rearward, and thus the angle of attack increased, directing the net force vector closer to vertical. The flapping gait was also adjusted by increasing the flapping amplitude and slightly increasing the flapping rate. This brought the prototype within the range commonly exhibited by flying animals, and resulted in sustained flight with the ability to climb and maneuver.

Figure 3.8: Fully Assembled Robo Raven

The flapping gait was programmed on the Arduino Nano. Average force production during testing was 242.9 g (5.5 g standard deviation) lift and 119.6 g (6.4 g standard deviation) thrust. Due to some turbulence in the wind tunnel a small amount of variability was present across trials. The typical flight duration of the

system with a 370 mAh onboard LiPo battery is 4 minutes and 30 seconds. Flight testing the Robo Raven has helped us to understand the capabilities and operational conditions during cruising, which are summarized in Table 3.5.

Table 3.5: Flight test results of the Robo Raven

Parameter	Value	Units
Flap Rate	4.0	Hz
Flap Amplitude	100	degrees
Angle of Attack	20	degrees
Climb Rate	0.53	m/s
Reynolds Number	124,000	-
Strouhal Number	0.395	-
Minimum Turning radius	6.1	m

3.7 Conclusions

A new FWAV platform called Robo Raven was developed that flies with wings independently controlled by digital servo motors. This represents an improvement in flight capability and takes a step closer towards replicating avian flight. Thus, this platform represents a significant advance towards biomimicry of birds using a FWAV platform.

Successfully realizing this design required a multi-faceted approach. First, advanced manufacturing processes such as 3D printing and laser cutting were used to create lightweight polymer parts to reduce the weight. Second, wing motion profiles were programed that ensured that wings maintain the optimal velocity during the flap cycle to achieve the right balance between the lift and the thrust. Third, a method to measure aerodynamic forces generated during the flapping cycle was developed. This allowed for quick evaluations of many different wing designs to select the best one.

Finally, a systems approach was adopted to make sure that all components worked well as an integrated system.

Due to the relatively large size of the FWAV, it is an ideal candidate for solar cell integration. The current maximum flight time is currently 4 minutes and 30 seconds and the current aerodynamic forces have been measured and recorded. Changes in design can be easily tested and quantified using the current methods.

Chapter 4: Design, Fabrication, and Characterization of Multifunctional Wings to Harvest Solar Energy in Flapping Wing Aerial Vehicles

This chapter is the work presented in *Smart Materials and Structures* [47]. In this section we describe a layered fabrication method that was developed for realizing multifunctional composite wings for Robo Raven by creating compliant wing structure from flexible solar cells. The deformed wing shape and aerodynamic lift/thrust loads were characterized throughout the flapping cycle to understand wing mechanics. A multifunctional performance analysis was developed to understand how integration of solar cells into the wings influences flight performance under two different operating conditions: (1) directly powering wings to increase operation time, and (2) recharging batteries to eliminate need for external charging sources. The experimental data is then used in the analysis to identify a performance index for assessing benefits of multifunctional compliant wing structures. The resulting platform, Robo Raven III, was the first demonstration of a robotic bird that flew using energy harvested from solar cells. We developed three different versions of the wing design to validate the multifunctional performance analysis. It was also determined that residual thrust correlated to shear deformation of the wing induced by torsional twist, while biaxial strain related to change in aerodynamic shape correlated to lift. It was also found that shear deformation of the solar cells induced changes in power output directly correlating to thrust generation associated with torsional deformation. Thus, it was determined that multifunctional solar cell wings were capable of three functions: (1) lightweight and flexible structure to generate aerodynamic forces, (2)

energy harvesting to extend operational time and autonomy, and (3) sensing of an aerodynamic force associated with wing deformations.

4.1 Introduction

As a part of previous work, we have developed a highly maneuverable FWAV named Robo Raven [38]. These vehicles rely on flapping wings and their deformation to generate the aerodynamic forces necessary for flight. The size of these vehicles are comparable to the size of actual birds found in nature. This platform features independently controlled programmable wings. In FWAV such as Robo Raven, flight endurance is one of the primary concerns. To perform missions in remote regions, the UAV cannot charge batteries using electrical outlets. A possible way to overcome this challenge would be to charge batteries using on-board solar cells. Since Robo Raven has a large wing area, solar cells can be integrated into the wings. The resulting compliant wing structure with integrated solar cells can be considered both multifunctional and smart because it not only provides lift and thrust, but also acts as a method of harvesting energy and sensing changes in deformation caused by aerodynamic loading, which can be used to determine changes in the flapping profile to improve flight control. This combination allows for increased flight time while decreasing the payload contribution of a large power source, thus potentially allowing for either: (1) size reduction with the same performance capability, or (2) an increase in overall payload capacity. It also introduces new capabilities for control schemes through new sensing capabilities. Successful development of multifunctional compliant wing structures through the integration of multiple functions can be expanded to other aspects of all UAVs, including fixed wing and rotary craft.

Integrating solar cells into the wings presents the following three challenges. First, a new manufacturing process is needed to integrate solar cells into wings without substantially increasing weight. Second, we need to ensure that wings with integrated solar cells maintain the appropriate deformation during the flapping cycle to ensure production of adequate aerodynamic lift and thrust. Finally, we need to make sure the modified version of Robo Raven with multifunctional wings produces enough thrust and lift to compensate for the heavier wings and enable flight.

In this chapter, we describe a new layered fabrication method for integrating commercial off-the-shelf solar cells into wings for a new solar-powered FWAV: Robo Raven III. Different wing designs were tested to observe how adding different quantities of solar cells affects flight performance through wing deformation, and how this leads to changes in power output that can be measured for potential onboard sensing and control. A new multifunctional performance analysis is also developed to quantify the effects of solar cell integration on recharge time and flight time to determine trade-offs from the multifunctional effects of solar cell integration to be considered by examining the impact of lift and thrust on power requirements versus the gains from recharging by harvesting solar energy.

4.2 Design and Layered Manufacturing Process for Compliant Multifunctional Wings

4.2.1 Design of Compliant Multifunctional Wing

Multifunctional wings were created for Robo Raven III (Figure 4.1). The design of the multifunctional wing, also seen in Figure 4.1, was adapted from a design we used previously for Robo Raven, which has been shown to be effective in generating lift and thrust forces necessary for flight [38]. The parameters of the wing

are as follows: S is the semi-span, C is the chord, and t_n are the diameters of carbon fiber stiffening rods. Table 4.1 presents values of the wing parameter used in the design reported in this paper. The wing membrane is a 0.001" thick film of biaxially-oriented polyethylene terephthalate (Mylar) which provides flexibility and toughness while remaining lightweight. Table 4.2 lists the properties of the base Robo Raven platform with batteries.

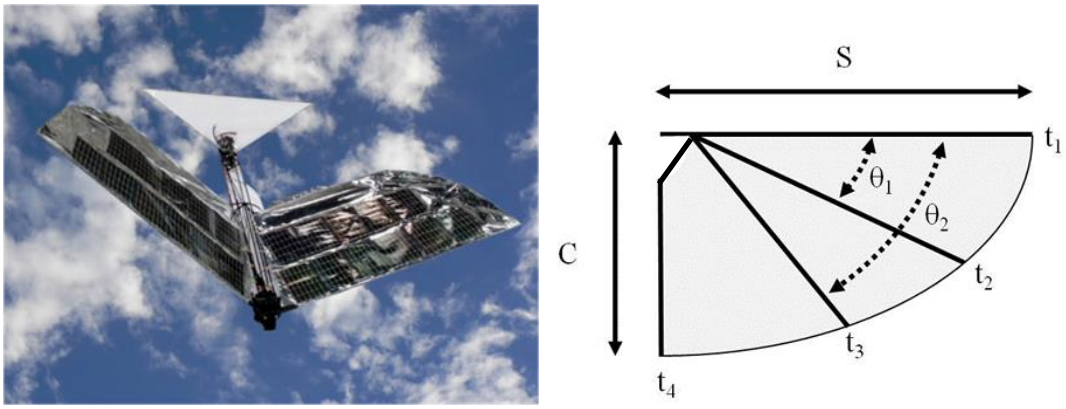

Figure 4.1: (left) Robo Raven III, the first solar powered robotic bird using multifunctional wings, and (right) parameters for the multifunctional wing design: ***S*** is the semi-span, ***C*** is the chord, and $\boldsymbol{t_n}$ are the diameters of carbon fiber stiffening rods

Table 4.1: Parameters for multifunctional wing design

Parameter	Value	Units
S	605.8	mm
C	362.0	mm
t_1	3.18	mm
t_2	1.63	mm
t_3	1.63	mm
t_4	1.63	mm
θ_1	0.358	Rad
θ_2	0.750	Rad

Table 4.2: Properties of Robo Raven.

Parameter	Robo Raven	Unit
Total Mass	0.29	kg
Length	0.554	m
Wingspan	1.168	m
Average Chord	0.248	m
Aspect Ratio	2.01	
Flight Speed	6.7	m/s

4.2.2 Multifunctional Wing Fabrication

To produce appropriate aerodynamic lift and thrust forces, many ornithopters rely on large deformations using compliant wings at lower flapping frequencies to achieve airfoil shapes [24]. The basic compliant wing structure weighs 16.8g with a total area of 1420cm^2. To maintain compliance when creating a multifunctional wing with a similar structure, Powerfilm's© MPT6-75 flexible solar cell modules were chosen. These flexible 7.3 x 11.4 cm amorphous silicon solar cell modules are reported by the manufacturer to produce 50mA of current at 6V at 100% sunlight flux, which represents their maximum power point. However, the bending stiffness and mass of the solar cells as packaged and was much higher than the Mylar, and therefore would not allow the wing to deform enough to maintain flight. Therefore, modifications had to be made to the solar cells to reduce the mass and bending stiffness to be more compatible with the Mylar. By heating and peeling off the protective encapsulation on the solar cells, the bending stiffness of the solar cells and

mass was substantially reduced. Then, solar modules were glued and soldered together in parallel to produce more current. Creating the multifunctional wings from the de-encapsulated solar cells modules involved a layered manufacturing process (Figure 4.2), and the completed multifunctional wing structure integrated into Robo Raven III can be seen in Figure 4.3.

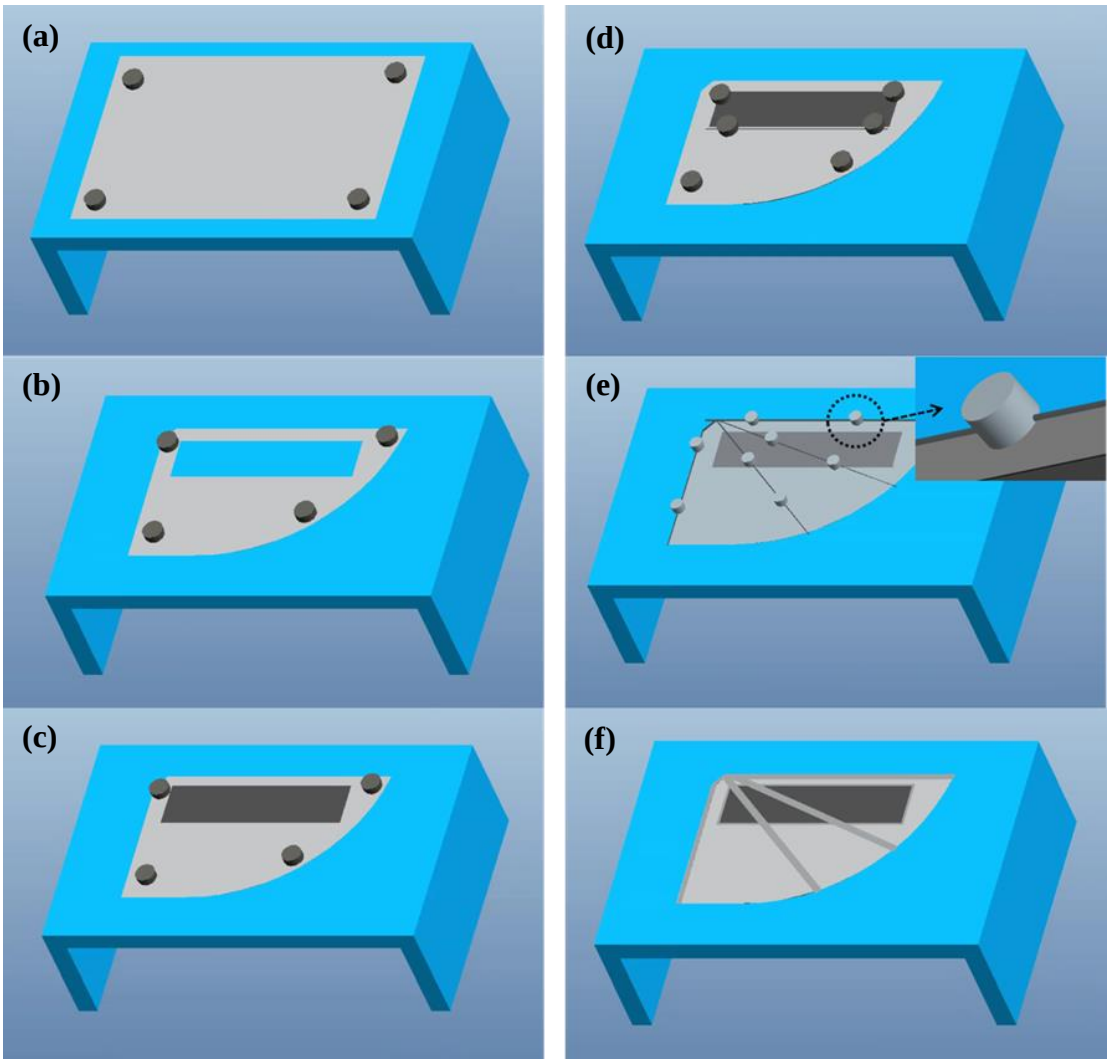

Figure 4.2: Layered manufacturing process for multifunctional solar cells wings (bottom side of wing is shown).

To fabricate the wing, a layered manufacturing process was developed to provide precise control over the location of each element of the wing (Figure 2). The layered manufacturing process consisted of the following steps:

(a) A sheet of Mylar is secured to a work table with the use of magnets.

(b) The wing shape including the hole for the solar modules is cut from the secured sheet of Mylar.

(c) The solar modules are applied to the wing.

(d) A Mylar frame is adhered around the solar modules that holds the solar cells in place.

(e) The spars are held in place using magnetic holders with notches while they are adhered to the wing.

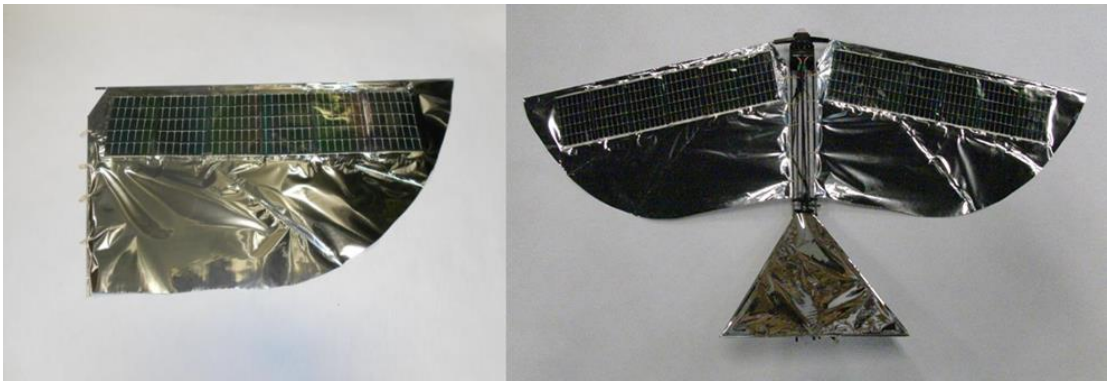

Figure 4.3: (Left) Assembled multifunctional wing with 6 solar cell modules, (Right) multifunctional wings integrated into Robo Raven III.

Once Robo Raven III was completed, a flight test was conducted and it was determined that the platform could achieve flight. The first version of Robo Raven III used 6 solar cell modules in each wing to generate 300 mA at 6V, so a second row of solar cells consisting of 5 modules were used to replace as much of the original wing material as possible (Figure 4.4). This version of Robo Raven III was also flight tested, and it was determined that the new wing design was incapable of continuous flight for more than 10 seconds due to increase in mass and decrease in thrust and lift force generation. Based on our previous experience, additional compliance at the trailing edge of the wing can compensate for the increase in stiffness over the area of

the wing when solar modules are integrated, so the wing was redesigned accordingly. The modified wing design compared to the original wing design can also be seen in Figure 4.4. There are three main differences between the new design and the previous. The first two involve extending carbon fiber tubes in the inside part of the wings to permit increase in wing area and compliance of the wing at the trailing edge. The final modification involved changing the shape of the Mylar skin into a "teardrop". It was determined that the modified wing design was capable of restoring flight capability to Robo Raven III.

Figure 4.4: (Left) original Robo Raven III wing design with 11 solar cell modules, and (Right) the modified wing design.

4.2.3 Integrating Multifunctional Wings into Robo Raven for Energy Harvesting

Robo Raven uses a two-cell Lithium Polymer battery rated at 7.4V and 370mAh. To maintain the balance of the battery cells when charging with the multifunctional wings, a charging circuit was design as seen in Figure 4.5. Each module produces 50mA at 6V at 100% sunlight flux with the voltage from each wing depicted in Figure 4.5 as V1 and V2. A zener diode with a breakdown voltage of 4.3 V is used to regulate the voltage so it does not exceed the maximum of 4.2 V for each cell. The resistor in the circuit was chosen to achieve the appropriate voltage drop

from the modules based on their current, reducing the power generation by 25%. The drop is transformed to heat and can be felt radiating from the electronics.

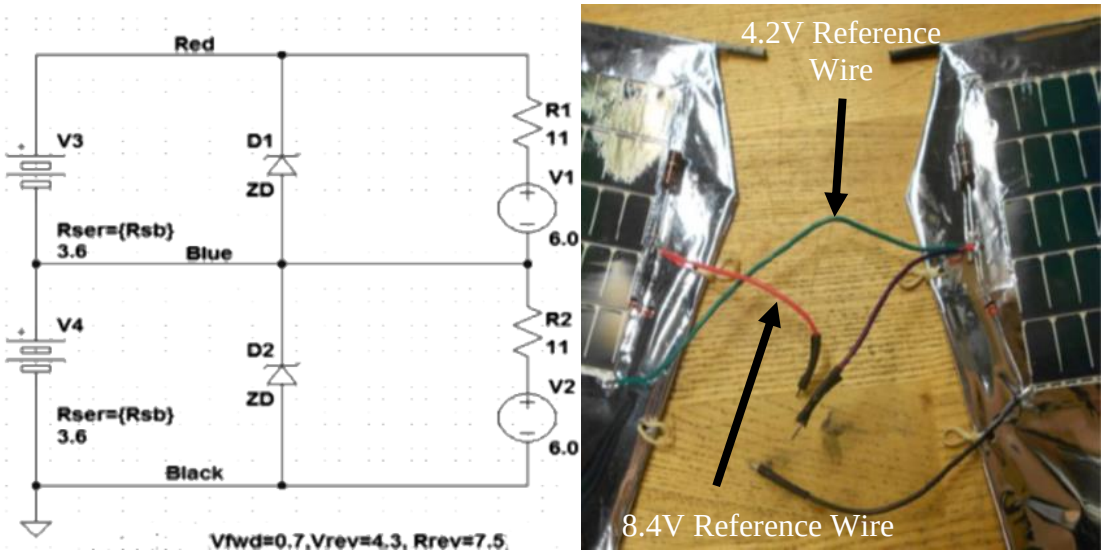

Figure 4.5: (Left) Schematic of battery charging circuit used for multifunctional wing structures, and (Right) the actual wiring of the solar cells for the circuit.

For direct powering of the servomotors, the solar cells were directly connected to the servomotors instead of the battery. This is possible since servos can operate at up to 7.2V and the solar cell output has been measured up to 7.8V. This would optimize performance of the solar cells for powering the UAV in series with the battery pack, as opposed to the 25% reduction in power experienced when utilizing the recharge circuit for the battery. This has an additional benefit of prolonging the life of the battery by allowing the solar cells to assist the battery in powering the UAV, thereby reducing the current draw on the battery and extending the discharge time.

4.3 Experimental Characterization of Wing Mechanics

4.3.1 Measurement of Lift and Residual Thrust Forces

Since existing computational models are inadequate for accurately predicting aerodynamic loads acting on compliant flapping wings, direct measurement of these loads during the flapping cycle was selected as the method for gaining insight into the effects of wing design parameters on the wing mechanics. For this study, we adapted the previous test stand we developed, but used the same 6 DOF ATI Mini40 load cell mounted on a wood and Delrin frame for measuring aerodynamic lift and thrust loads simultaneously, as well as the moments generated (Figure 4.6). The test stand also allowed the UAV to be set to any angle of attack from 0 to 20 degrees, which was the angle of the bird body relative to the wind direction. Unlike the previous test stand the load cell is horizontal to the ground and allows for the lift and thrust forces to be measured directly. To simulate the actual flight conditions, the test stand is placed at the end of a wind tunnel operating at 6 m/s, which is near the actual flight speed.

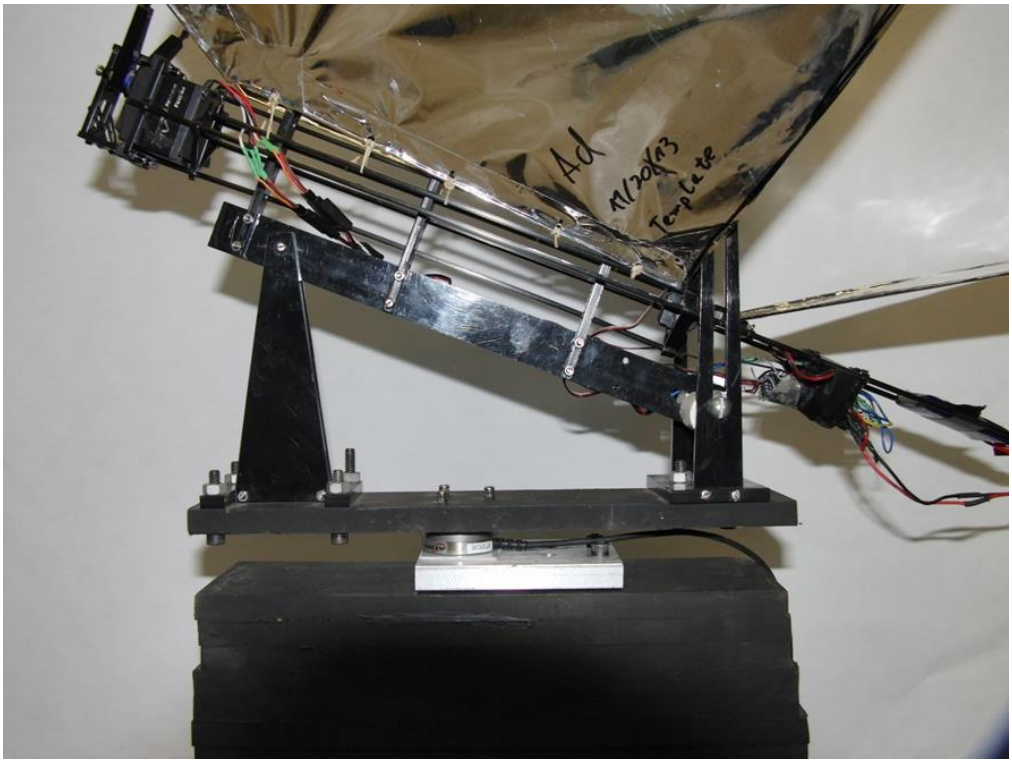

Figure 4.6: Test stand used in wind tunnel to characterize aerodynamic lift and thrust loads on the compliant multifunctional wings.

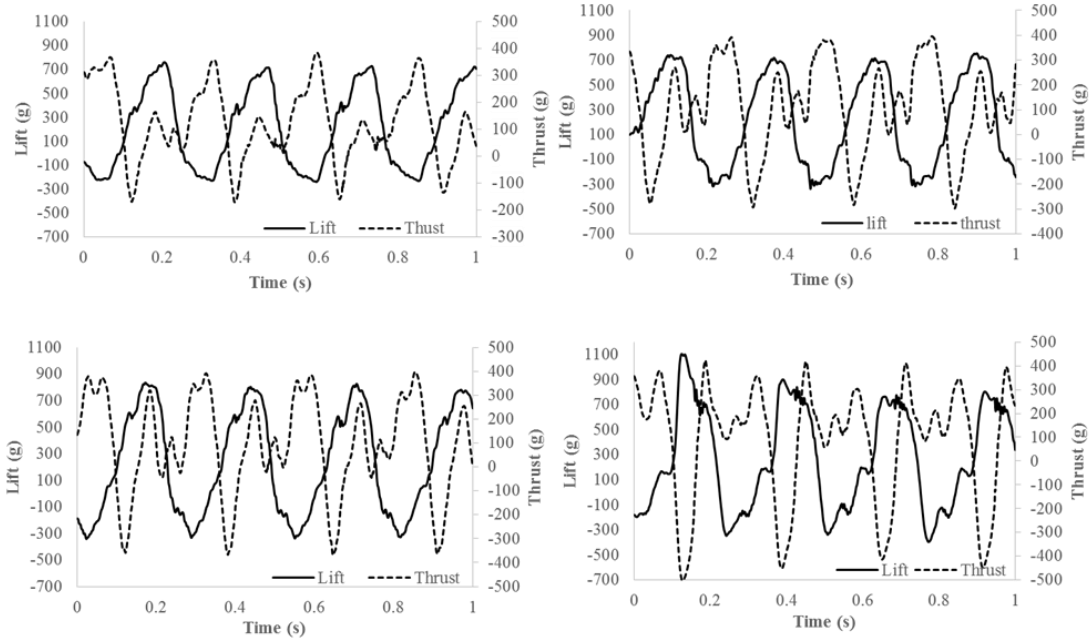

Figure 4.7: Time resolved load cell results for all four wing designs: (top left) regular, (top right) 6 module, (bottom left) 11 module, (bottom right) modified 11 module.

The wings were testing at a flapping frequency of 4 Hz and were programmed to flap with a range of 60 degrees. The wings flapped symmetrically orthogonal to the body of the UAV. Time resolved load profiles for wings with and without solar cells can be seen in Figure 4.7 for Robo Raven. These thrust and lift profiles are consistent with previous measurements and models of flapping wings where the lift produces a sinusoidal profile consistent with aerodynamic drag while the residual thrust exhibits a double peak consistent with a "blowback" effect from the rear of the wing during the flapping cycle [26, 38]. As a result, the peaks appear 180° out-of-phase when they overlap on the time-resolved plot.

Comparing these profiles for each wing design, it can be seen that there is a slight change in performance caused by the addition of solar cells on the wings. Because the solar cells stiffen the wings and reduce compliance in sections of the wing structure, it was predicted that the solar cell wings would underperform the regular wings. However, from the profiles it seems that the 6 module wings actually have slightly larger values for lift compared to the regular wings. For the 11 module wings, the values for thrust decreased significantly compared to the original wings with only a slight increase in lift, which was consistent with the observed loss of flight capability. The modified wing design had an increase in lift force generation compared to the original wings, consistent with the observed restoration of flight capability. The average values of lift and residual thrust load for each trial can be seen in Table 4.3.

Table 4.3: Lift and residual thrust loads generated by each wing design

	Robo Raven		12 Module Robo Raven III		22 Module Robo Raven III		Modified 22 Robo Raven III	
	Residual Thrust (g)	Lift (g)	Residual Thrust (g)	Lift (g)	Residual Thrust (g)	Lift (g)	Residual Thrust (g)	Lift (g)
Trial 1	111	218	105	201	70.6	240	77.4	247
Trial 2	104	220	98	219	75.2	242	101	229
Trial 3	109	221	98	218	91.9	237	74.8	268
Average	108	220	100	212	79.2	240	84.5	248
Std. Dev.	3.36	1.79	3.86	10.1	11.2	2.53	14.7	19.5

In a wind tunnel, a residual thrust value of 0 g would correlate to steady-state flight conditions. However, our low speed wind tunnel has a maximum velocity of ~5 m/s, while the actual flight velocity for Robo Raven is 6.7 m/s. Since this meant the aerodynamic force would be approximately 25% greater during flight, a scaling factor of 1.4 X was determined using this value combined with a measured maximum payload of 40 g for Robo Raven. Thus, this scaling factor made it possible to predict the corresponding payload capacity of Robo Raven from the wind tunnel data (*Force Magnitude X Scaling Factor = Total Flight Weight*). The corresponding results, seen in Table 4, clearly explain why the original 22 module UAV did not fly given the predicted payload of -4 g, which was recovered to 21 g with the modified wing design.

Table 4.4: Weight and payload characteristics for each UAV design

	Robo Raven	12 Module Robo Raven III	22 Module Robo Raven III	Modified 22 Module Robo Raven III
Weight of UAV (g)	290	317	331	346
Force Magnitude (g)	234	235	232	260.1
Total Flight Weight (g)	330	332	327	367
Payload (g)	40	15	-4	21

4.3.2 3D Digital Image Correlation (DIC) Characterization of Wing Shape

Previously, Stanford et al. used 3D Digital Image Correlation (DIC) to study wing deformations in fixed membrane wings for MAVs to optimize their design for aerodynamic forces [40]. We utilized 3D DIC to study the effects of deformation on the different multifunctional wing designs by quantifying differences in shapes and strain and relating it to the aerodynamic loads generated during flapping. For our 3D DIC investigation, two Flea3 FL3-FW-03S1M cameras were used to acquire stereoscopic high speed images at 80 HZ while the wings were flapping at 4 Hz. Speckle patterns were applied to the surface of the wings, and the software package VIC-3D (Correlated Solutions, Inc) was used to obtain deformation measurements at 20 different angles during a single flapping cycle.

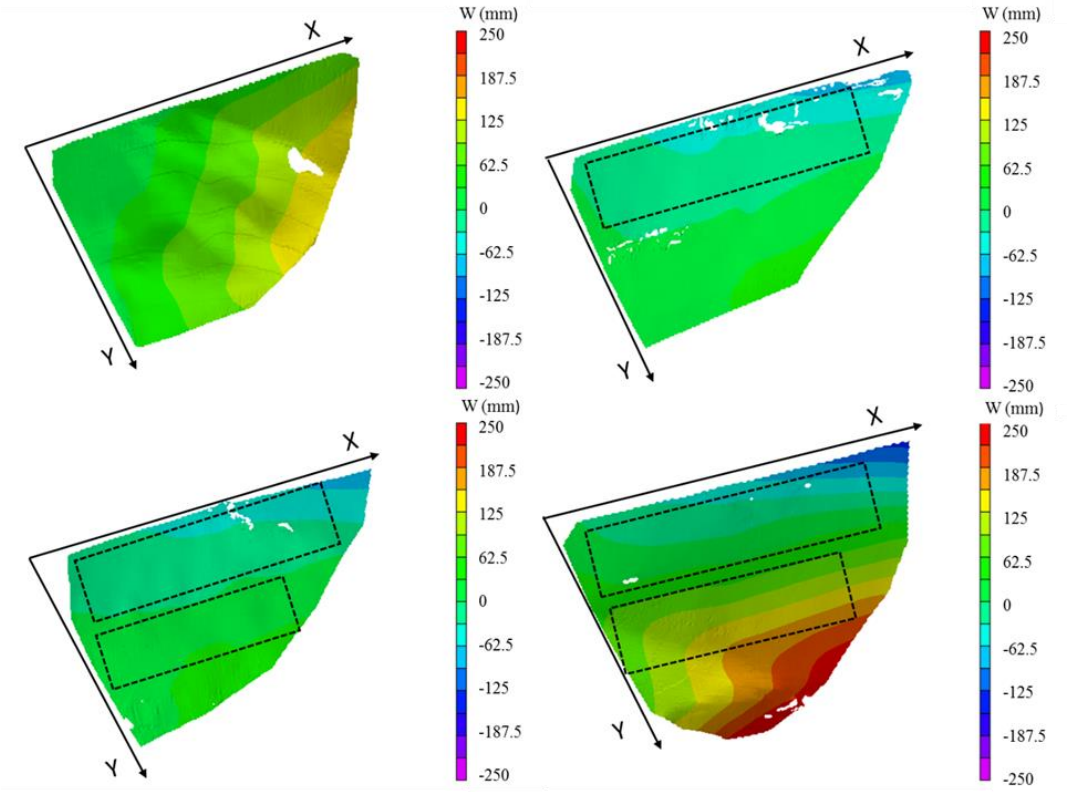

Figure 4.8: Comparison of out-of-plane displacement (W) for each wing at the horizontal position while flapping downward, which was found to be most representative of the relative deformations between the wing designs for the 20 different wing positions that were measured during a single flapping cycle. (top left) regular, (top right) 6 module, (bottom left) 11 module, (bottom right) modified 11 module. Dashed lines indicate approximate location of the modules

Representative DIC data associated with wing shape be seen in Figure 4.8, which was obtained by taking the out-of-plane displacement (W) in the z-direction normal to the wing while it is in a horizontal position while flapping downwards. For these measurements, the x-axis and corresponding U displacements were chosen to run along the leading spar of the wings, while the y-axis and V displacements runs along the body of the UAV. At the horizontal position, wings are generating the most aerodynamic lift and exhibit the greatest deformation. It is clear that the regular wing has greater deformation towards the trailing edge of the wing than the 6 module wing or the 11 module wing, where the deformations are more indicative of bending on the

leading edge. These larger deformations are intuitive since the wings are not stiffened by the addition of solar cells.

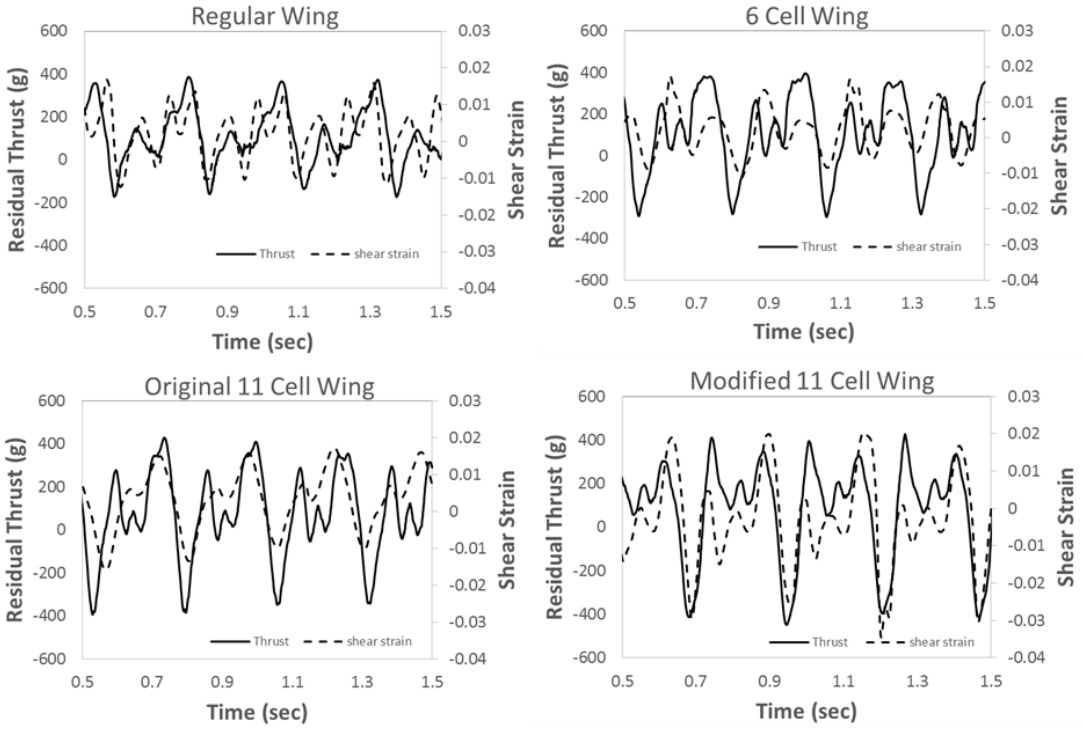

Figure 4.9: Comparison of time resolved residual thrust and shear strain: (top left) regular, (top right) 6 module, (bottom left) 11 module, (bottom right) modified 11 module.

A comparison was also made between the four wings and the time-resolved resolved thrust and aerodynamic lift loads versus the average shear strain and biaxial strain respectively of the entire surface of the wing throughout the flapping cycle (Figures 4.9 and 4.10). The aerodynamic lift and thrust correlate strongly with the biaxial strain and shear deformation from the DIC results. Since we are interested in the change in biaxial strain, the mean strain was subtracted from the strain observed throughout the flapping cycle to compare the differences. As mentioned earlier, it is clear that the integration of solar cells has an effect on the wing shape during the flapping cycle due to the increased stiffness of the solar cell material relative to

Mylar. This in turn reduces the amount of thrust and lift as the solar cells are integrated into the regular wing design. However, by increasing the wing area in the modified 11 module wing design, residual thrust and lift could be recovered, although greater deformation was also observed that could influence performance. The 17% increase in wing area provided an additional 7% of thrust force and 4% of lift force. The correlation between the lift and thrust forces to the biaxial and shear strains have been measured using the correlation coefficient. These values are shown in Table 4.5.

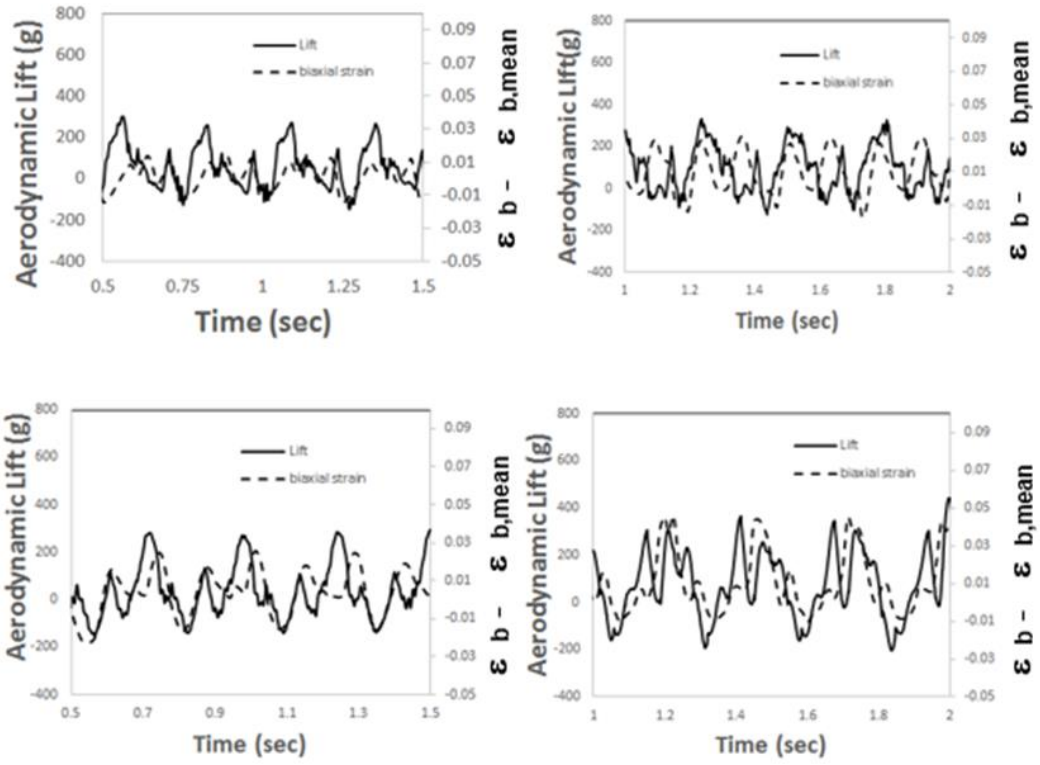

Figure 4.10: Comparison of time resolved aerodynamic lift and biaxial strain relative to mean biaxial strain for the entire wing: (top left) regular, (top right) 6 module, (bottom left) 11 module, (bottom right) modified 11 module.

Table 4.5: Correlation coefficients between thrust and lift forces and shear and biaxial strains respectively.

	Robo Raven	12 Module Robo Raven III	22 Module Robo Raven III	Modified 22 Robo Raven III
Thrust/Shear Strain Correlation Coefficient	0.45	0.39	0.65	0.66
Lift/Biaxial Strain Correlation Coefficient	0.56	0.19	0.45	0.77

As the majority of the wing becomes covered in solar cells, the deformation of the wing decreases. By observing the time resolved results from the 6 module and 11 module wings, it is clear that the shear strain slightly decreases as solar cells are added. Where the 6 module wing achieved a strain of 2% the 11 module wing remains under 2%. By increasing the wing size and allowing for more deformation, a large increase in shear strain in the modified 11 module wing is observed. These results are also mirrored in the cyclic results. The shear strain for the 6 module wing and 11 module wings have a much lower value than the regular wings. However, the modified 11 module wings have a much higher shear strain value. This increase in deformation is the difference between the original 11 cell wing and the modified 11 cell wing. The increase in compliance is what allows the modified 22 module UAV to maintain flight. The increase stiffness and weight of the solar cells is counteracted by the increase in overall wing deformation.

4.4 Multifunctional Performance Modeling of Wings

A new model was developed to characterize the multifunctional performance of the wings based on the aerodynamics of flapping wing UAVs. Let F_t be the thrust generated by the flapping wings, V be the flight velocity due to F_t, and F_l be the

aerodynamic lift at flight velocity V for the baseline UAV. Let M_m be the mass of the baseline UAV, and M_b be the mass of battery on the baseline UAV. To maximize the flight time, the largest possible battery permitted by the lift can be used, leading to the following condition:

$$F_l = (M_m + M_b)g \tag{4.1}$$

or

$$M_b = F_l/g - M_m \tag{4.2}$$

Let U be the energy capacity of battery on the baseline UAV. In general, U is proportional to the mass of the battery M_b. So,

$$U = k_b M_b \tag{4.3}$$

where, k_b is battery coefficient. The flight time for this baseline configuration will therefore be:

$$T = U/P = k_b M_b/P = k_b(F_l/g - M_m)/P \tag{4.4}$$

Where P is the power consumed by the UAV during flight. P is a variable that changes with each vehicle. It is measured by observing the amount of time it takes to deplete a fully charged battery and knowing the battery's energy capacity.

For multifunctional wings, M_s is the mass of solar cells in the wings. The solar cells have the following effects:

- They are expected to alter the thrust due to stiffening of the wings. The changed thrust leads to a different flight velocity, V' , due to a relative change in drag force, $k_1 = V'/V = (F'_t/F_t)^{0.5}$

- They also change the aerodynamic lift coefficient by a ratio, k_2, resulting in a total aerodynamic lift $k_1k_2F_l$.

Equation (4.1) becomes,

$$k_1k_2F_l = (M_m + M_s + M'_b)g \quad (4.5)$$

Where M'_b is the mass of battery on the UAV with solar cell integrated wings. So,

$$M'_b = k_1k_2F_l/g - M_m - M_s \quad (4.6)$$

Flight time for the multifunctional wings will therefore be as follows when directly providing power during flight:

$$T' = k_bM'_b/ (P-k_sM_s) \quad (4.7)$$

In this expression, the power produced by the solar cells is assumed proportional to the mass of the solar cell, and k_s is the solar coefficient influenced by factors such as the conversion efficiency of the solar cell and the solar energy flux. Flight time for the multifunctional vehicle would be as follows if the solar cells do not provide power during the flight (i.e., *baseline flight time*):

$$T' = k_bM'_b/ P \quad (4.8)$$

Using Equation (4.6), we can determine the flight time when the solar cells provide power as follows:

$$T' = k_b (k_1k_2F_l/g - M_m - M_s)/(P-k_sM_s) \quad (4.9)$$

Provided the current output of the solar cells does not exceed the recharge limit of the battery, the battery recharge time for an UAV with integrated solar cells can also be determined as follows:

$$T_r = f_c k_b \, (k_1 k_2 F_l / g - M_m - M_s) / k_s M_s. \tag{4.10}$$

Where f_c is the fraction of the battery charge that was consumed before recharging.

For most situations, flight time is considered a system design problem, resulting in a constraint on the minimum value of flight time,

$$T_{\text{flight}} \geq T_{\min} \tag{4.11}$$

If $T \geq T_{\min}$, then there is no benefit in integrating solar cells into the wings such (i.e., $T' = T_{\min}$). Therefore, the objective in that case would be to select M_s such that T_r is minimized without T' exceeding $T_{\min}$. Since there are complex interactions between the baseline wings and solar cells, solar cells should be placed such that k_1 and k_2 are maximized in order to maximize T'.

Equation (4.7) enables the multifunctional criterion k_s to be determined that allows for the mass of the solar cells to generate the same amount of current as consumed by the UAV (i.e., *infinite flight time*), and can be considered a critical multifunctional criteria, k_s^*, under the following condition,

$$k_s^* = \frac{P}{M_s} \tag{4.12}$$

Therefore, a comparison between the multifunctional criterion for the solar cells, k_s^*, and the mass of the UAV, M_m, can also be made for design purposes based on: (1) area of solar cell coverage, and (2) power consumed by the UAV.

4.5 Experimental Results for Multifunctional Performance

Inputs for the multifunctional performance model were obtained from experimental results. Since flight conditions can be different for each flight, these experiments were conducted while holding the vehicle in place and pointing the wings towards the sun. These experiments were conducted on clear sunny days at noon with the planform area of the wings parallel to the sun. The wings allowed to flap where Battery energy storage is typically stated as Ampere-hour (A-hr). Hence for the power calculations, energy storage is multiplied by the operating voltage of the battery and get power in terms of Watt-hour (W-hr). The value k_b is obtained by dividing battery capacity by battery mass, resulting in 106.54 W-hr/kg. To determine flight time, a fully charged battery was used to power the UAV until depleted by flapping, resulting in 4.50 min. Using this in Equation (4.8), the average current draw from the batteries was found to be 4.9 A. The UAV mass, battery mass, and solar cell module mass were determined using a DigiWeigh model DWP-1001 scale with 0.1 g resolution, resulting in 263.3 g for the UAV, 25.7 g for the battery, and 1.7 g per module. Therefore, the minimum total mass without solar cells is 289 g, and the F_l is 2.83 N.

Due to the change in wing design for the modified 22 module UAV, the M_m increases to 278.3 g, resulting in a F_l of 2.98 N. The actual lift force generated by the UAV was previously measured to be 3.23 N. To compare the aerodynamic lift

changes caused by the integration of solar cells, the raw lift forces were compared for all wing designs. Thus, the k_2 was found to be 1.023 for the 12 solar cell UAV, 1.029 for the original 22 module UAV, and 1.194 for the modified 22 module UAV. Similarly, k_1 had to be calculated for each of the new wing designs since a change in thrust production was observed on the load cell. Using the thrust forces observed on the load cell, k_1 was 0.970 for the 12 solar cell UAV, 0.912 for the 22 module UAV, and 0.922 for the modified 22 module UAV.

4.5.1 Direct Powering of Motors

To calculate *T'*, k_s must be found first. Since k_sM_s gets subtracted from *P*, k_sM_s is equal to the power being supplied by the solar panels, which was measured to be 4.10 W for the 12 module UAV. Therefore, using the previously reported mass of the solar cells of 27 g, k_s equals 0.152 W/g. This makes the new predicted maximum flight time 5.05 minutes. This represents an 11.5% increase in operation time using the solar cell wings. Thus, the overall effect of using the solar cell wings on flight time turns out to be positive despite the additional mass and rigidity that it adds to the wings.

The calculation is slightly different for the 22 module UAV. Since the body of the UAV was modified to accommodate the new wing design, a different flight time can be expected since the weights of the UAVs are different. To lift the difference in weight, the servos must pull more power from the battery, shortening the flight time. The new flight time for this wing was 4.32 minutes, which is consistent with the increased weight and area requiring more energy to power the wings at the same frequency and amplitude. The average current draw was calculated

to be 5.14 A, which results in an average power consumption of 37 W. Next, the new k_s for the modified 22 module UAV must be calculated. The solar cells add an additional 42 g to the UAV and were found to generate 7.41 W, making k_s a value of 0.176 W/g. Using these numbers, we can predict the new maximum time of flight of the 22 module UAV using Equation (4.9). The new time was calculated to be 5.23 minutes. This is 12.5 seconds more than the 12 module UAV and a 15.4% increase in operational time compared to the original Robo Raven design.

The prediction of the multifunctional performance model demonstrates the potential gain from the solar cells. However, it does not take into account the power generation variations introduced by flapping the UAV. While flapping we expect a deviation from perfect conditions because the solar cells are constantly changing their position relative to the sun. We experimentally measured the increase on the operation time by using both battery and solar cells to power motors. During actual flight tests with the solar cells electrically connected, large variations in flight times were observed due to variations in flight conditions. Variations in flight conditions cannot be predicted or accounted for, so all flight endurance tests were done outdoors but on a test stand. All outdoor tests were done on a clear sunny day at noon. The wings were held at an angle where the most solar energy could be collected by the solar cells. The actual operation time for the 12 solar cell UAV increased by 10.2% (flight time of 5.00 minutes) which was close to predicted. The same test was done for the modified 22 module UAV. The actual operational time for the 22 module UAV was 5.17 min, representing a 14.1% increase in operational time, which was

also close to the prediction. Results for changes in power and flight time are summarized in Table 4.6.

It is important to note that while increasing the modules from 12 to 22 on the UAV only increased the operational time by 3.9%, the low increase was primarily due to the extra power required for the new wing design that reduced some of the solar cell benefit. This further reinforces the trade-off that is assessed when using more solar cells. Therefore, in addition to the time of flight, we also determined the critical k_s^* according to Equation (4.12) which would require improving the solar cell production output instead of adding more solar cells or redesigning the wing. Given M_s and P for the 12 module UAV, k_s^* equals 1.34 W/g. Given the value of 0.152 W/g for the flexible solar cells used in this investigation, we are at only 11.3% of the value needed for infinite flight. Thus, ~8.8X improvement is needed to reach infinite flight time. Doing the same calculation for the Modified 22 module UAV, k_s^* equals 0.787 W/g. With a k_s value of 0.176 W/g, we are generating 22.4% of the power necessary for infinite flight. Only ~4.5X improvement is needed for infinite flight. Since the efficiency of the flexible solar cells we are using is only 5%, infinite flight time would only require increasing the efficiency to 22.5%, which would obviate the need for batteries and render them a secondary power source.

Table 4.6: Comparison of predicted and measured flight time for regular and multifunctional wings (dnf denotes "did not fly")

	Power Consumption	**Solar Power Generation**	**Predicted Increase in Flight Time**		**Measured Increase in Flight Time**	
	W	W	Time (sec)	%	Time (sec)	%
Regular UAV	35.8	n/a	n/a	n/a	n/a	n/a
12 module UAV	36.4	4.10	29.4	10.8	27.6	10.2
22 module UAV	36.8	7.41	dnf	dnf	dnf	dnf
22 module UAV (modified wings)	37.0	7.41	41.9	15.4	38.1	14.1

4.5.2 Recharging of Batteries

To determine recharge performance to compare with the multifunctional performance model, the UAV was placed in sunlight, and measurements were taken to see how long it would take to completely recharge a depleted battery. The 2 cell Lithium Polymer battery is completely recharged when it reads 8.4V. The results for both the 12 solar cell and 22 module UAV are shown in Figure 4.11. It took 149 minutes for the 12 solar cell UAV to completely recharge the battery and 90 minutes for the 22 module UAV. These results are compared to the fastest theoretical results in Table 4.7 below. Differences can be attributed to the passive recharge circuit that minimized weight and power consumption. A more active circuit using maximum

power point tracking could optimize recharge time, but at the expense of adding more weight and increasing the power requirements for the UAV.

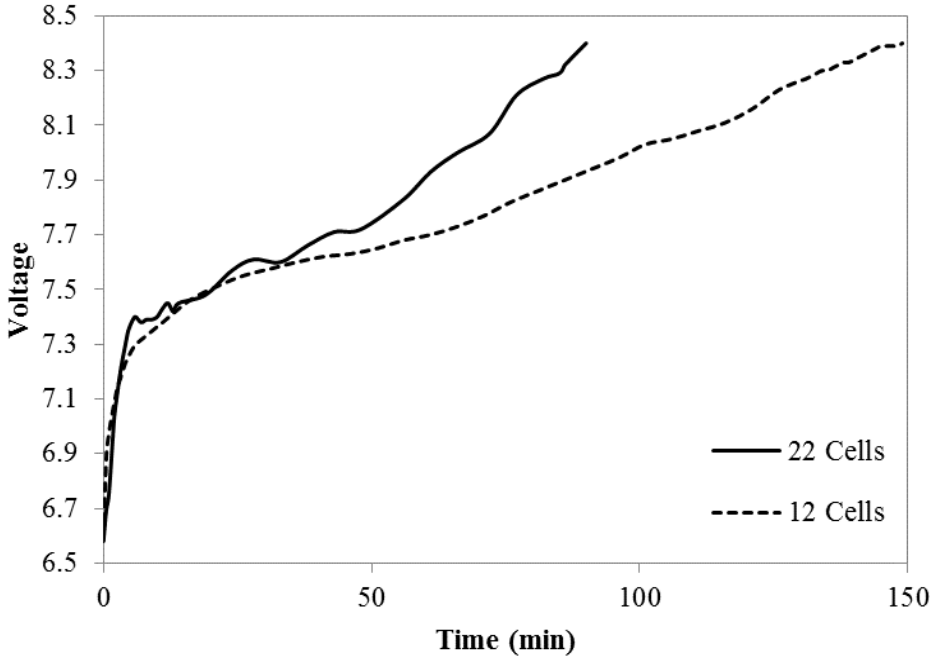

Figure 4.11: Recharging time profiles for the 12 and 22 module UAVs.

Table 4.7: Comparison of theoretical charging to actual charging results.

	Theoretical Fastest Recharging Time (Min)	Actual Recharging Time (Min)
12 module UAV	74.0	149
22 module UAV	40.4	90

4.5.3 Impact of Aerodynamic Forces of Power Output Solar Cells for Sensing

The time-resolved power generated by the multifunctional wings was determined by measuring the voltage and current during flapping. In Figure 4.12a, results for the 22 module UAV, generating an average of 7.42 W, are compared with the 12 module UAV, generating 4.10 W. The power output was expected to change

sinusoidally while flapping, due to its position relative to the sun. However, the response is not sinusoidal, which indicates the deformation of the wings must have an effect on power output as well. In Figures 4.12b and 4.12c, it was found that changes in the power output appear to directly correlate with the thrust generation of the wing. Since the thrust has been found to correlate with the amount of torsional deformation being produced, it is likely the cause of the changes is due to local rotations from the torsional deformations that can reorient cells more towards or away from the sun. Therefore, the solar cells wings are not only multifunctional in being able to harvest solar energy and serve as skin to generate aerodynamic force during flapping, but it can also be used to sense those forces due to the effects of the shear deformation. The shear strains on the surface of the wings for both the 12 and 22 module UAVs were compared to the % change in power output to observe their correlation. The two signals are compared in Figure 4.13. The correlation coefficients for percent change in power output to thrust and shear strain were found to validate their relationship, and are shown in Table 4.8.

The implications of sensing thrust using solar cells has many applications going forward. Gusts of winds can be detected during flights using the same structure that is used to help power the UAV. Thus, this information can be used to change the flapping profile in reaction to the changes in aerodynamic loads. These changes can be potentially automated to allow for correction while it is being piloted or flown autonomously, in which case the wings would be used as smart structures. Because the solar cells are being used to achieve longer flights, being able to adjust to flight

conditions using solar cell sensing can be a very powerful new tool for further increasing flight time.

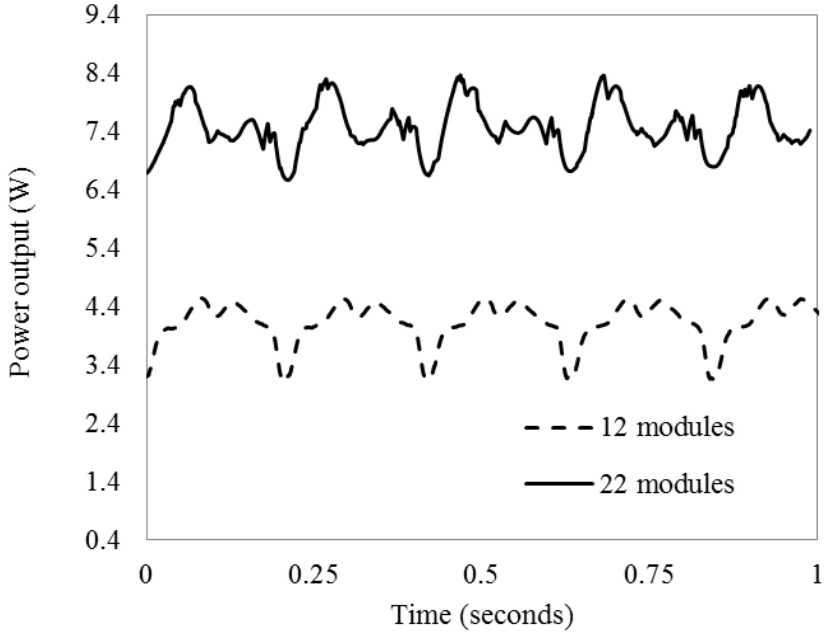

(a)

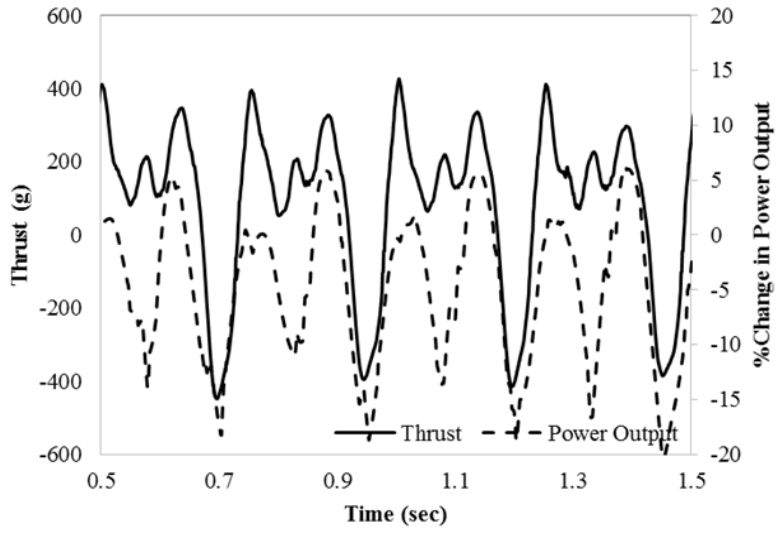

(b)

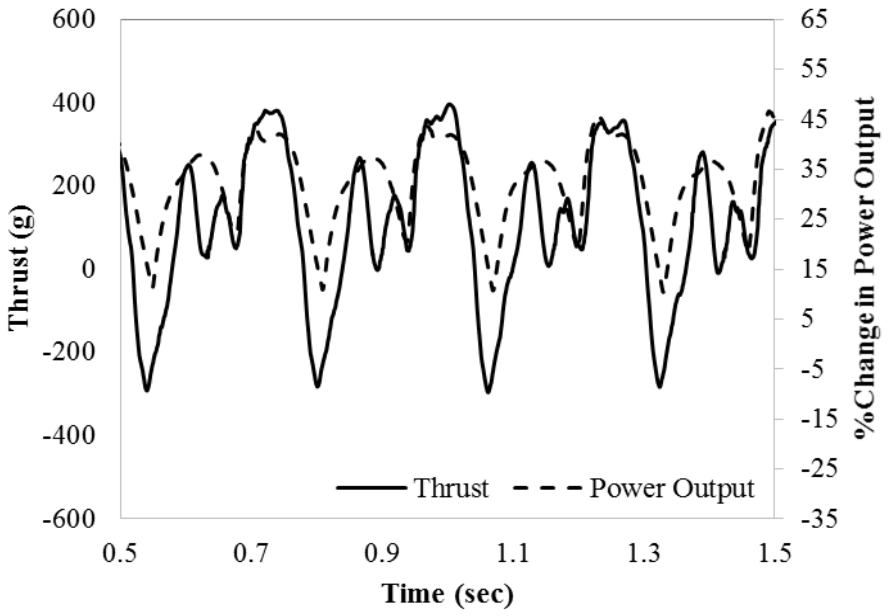

(c)

Figure 4.12: (a) Electrical power generated by the 12 and 22 module UAVs while flapping, and thrust versus % change in power output for (b) 22 module and (c) 12 module UAVs indicating that the solar cells can be used to sense aerodynamic forces due to the shear deformations.

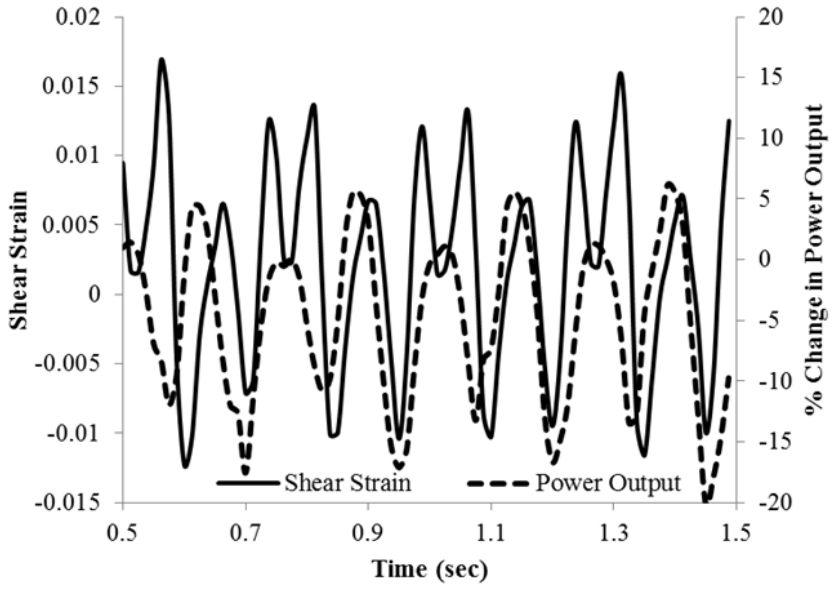

(a)

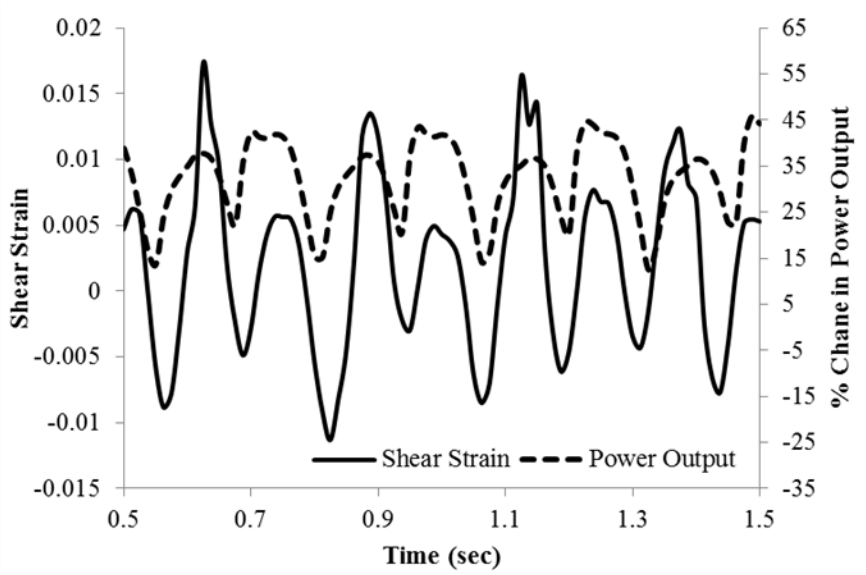

(b)

Figure 4.13: Shear strain versus % change in power output for (a) 22 module and (b) 12 module UAVs

Table 4.8: Correlation factors between thrust and % change in power output for each wing design

	12 Module UAV	22 Module UAV
Thrust/% Change in Power Output Correlation Coefficient	0.87	0.79
Shear Strain/% Change in Power Output Correlation Coefficient	0.53	0.26

4.6 Conclusions

This chapter investigates the mechanics that affect the potential benefits of introducing multifunctional structures to harvest solar energy on the wings of a flapping wing UAV. We used Robo Raven as our base platform for this investigation. Three different wing designs were initially observed: (1) the regular wings without solar cells, (2) wings with 6 solar cell modules that constitute a 12

module UAV, and (3) wings with 11 solar cell modules that constitute a 22 module UAV. Immediately, a deterioration in flight performance was observed when solar cells were added. The 12 module UAV was still able to fly, but the wings of the 22 module UAV were too stiff and heavy to generate enough aerodynamic lift, resulting in a calculated negative payload capacity. Knowing that deformation plays a major role in force production, the wing design for the 11 module wings was altered, and a modified wing design was developed for the 22 module UAV to recover aerodynamic forces.

With these four wing designs, the force production of each wing design was compared to understand the mechanical effects the solar cells had on the aerodynamic performance of the wing. Therefore, the lift and thrust forces generated by each wing design were quantified. Next, the deformation of each wing surface was quantified while flapping using 3D DIC to determine the specific effects of the mechanical properties of the solar cells as the wing design was varied. There was a clear correlation between the measured DIC deformations and the aerodynamic forces, in particular the correlation of the thrust force to the shear strain and biaxial strain to lift force which is critical to providing the forward velocity necessary to generate aerodynamic lift that enables the UAV to achieve flight. It was also found that the shear deformation of the solar cells induced changes in power output that directly correlated to the thrust generation, indicating that the multifunctionality of the solar cell wings was not limited to just harvesting solar energy and serving as skin to generate aerodynamic forces, but that they could also be used to sense those forces.

Next, the electrical benefits of adding solar cells were determined. A charging circuit was developed so that the UAV can be charged by the solar cells. The solar cells were also directly integrated to the electrical power of the UAV to extend the operating time of the UAV. A performance model was developed to model the change in operating time due to the integration of solar cells. It was determined that it takes 149 minutes to completely recharge the battery with 12 solar cells and 90 minutes to recharge with 22 modules. Theoretically we could have a maximum 13.9% increase in flight time with the 12 module UAV and a 21.2% increase for the 22 module UAV. Unfortunately the model does not take into account the flapping motion of the solar cells nor the heat of running these tests outdoors. We observed a 10.2% and 18.7% increase in operational time for the 12 module and 22 module UAVs respectively. The current solar cells have an efficiency of 5%; however, with recent developments in flexible PV solar cell technology provide more efficient solar cells can be integrated to provide for a longer and maybe infinite flight time. We found we would need a flexible PV solar cell that is 22.5% efficient to achieve infinite flight, and there are flexible PV solar cells that are more than 24% efficient commercially available.

In summary, the fundamental mechanics of adding solar cells to flapping wing UAVs has been established. The added stiffness of the solar cells prevents the wings from deforming resulting in a loss in aerodynamic force generation. The shear and biaxial strains on the surface on the wing were directly correlated to the thrust and lift generated by the wings. This new information is utilized in developing a multifunctional performance model to predict the effects on the flight time of the

UAV. Although the stiffness and weight of the solar cells were quantified and determined to have a negative effect on the aerodynamic force production, this was offset by the power generation of the solar cells to result in significant gains in the flight time. From this model, further addition of solar cells to larger wings, the body, or the tail of a UAV can be expected to result in increased flight time. However, the greatest benefit to flight time is expected to result from higher efficiency flexible solar cells, such as thin film GaAs multi-junction solar cells, where a 4.5X improvement in efficiency will theoretically result in infinite flight time and obviate the need for batteries other than as a secondary power source. Finally, it was determined that multifunctional solar cell wings were capable of three functions: (1) lightweight flexible structure to generate aerodynamic forces, (2) energy harvesting to extend operational time, and (3) sensing of aerodynamic forces.

Chapter 5: Integrating Solar Cells into Flapping Wing Air Vehicles for Enhanced Flight Endurance

This chapter investigates ways to redesign Robo Raven to significantly increase the wing area and incorporate more solar cells into the wings, tail and body. This was the work presented in the *Journal of Mechanisms and Robotics* [51]. Increasing wing area allows for additional solar cells to be integrated, but there are tradeoffs due to the torque limitations of the servo motors used to actuate the wings as well changes in the lift and thrust forces that affect payload capacity. These effects were modeled and systematically characterized as a function of the wing area to determine the impact on enhancing flight endurance. In addition, solar cells were integrated into the body and the tail. The new design of Robo Raven generated a total of 64% more power using on-board solar cells, and increased flight time by 46% over the previous design. They were also able to recharge batteries at a similar rate to commercial chargers.

5.1 Introduction

Recently, Robo Raven was developed at the University of Maryland [38,42]. It features independent wing control that allows the wing motions to be programmed to perform complex aerobatic maneuverers. A picture of Robo Raven can be seen in Figure 1. Its flight endurance was limited by the small battery pack used to power the vehicle, which was a 370 mAh 7.4V LiPo. Robo Raven was able to continually flap for around 4.5 minutes before the battery was depleted and significant decrease in flapping frequency was observed.

Figure 5.1: Robo Raven I [38]

Energy harvesting techniques can be implemented in FWAVs to meet the need for more available energy during flight and at rest, while increasing payload capacity by generating more lift can provide more energy storage. As part of previous work, Robo Raven IIIv1 was developed, which took advantage of a large amount of surface area in the wings to integrate solar cells [27]. Through this integration, the wings became multifunctional structures. The wings not only performed the function of providing the vehicle with the aerodynamic forces necessary for flight, but also provided electrical power for charging the battery. Initially, the Robo Raven III platform consisted of 12 solar modules integrated into the wing structure of the original Robo Raven design (Robo Raven IIIv1). These modules were integrated to the front most area of the wing, which minimized the changes in deformation of the flapping wings. The solar cells produced 3.6 Watts and resulted in a 27 second increase in flight time with the ability to recharge the battery to 8.4V in 149 minutes. To produce more power, more solar modules were integrated into the rest of original wings' surface area. This resulted in a different wing design

that allowed the FWAV to maintain flight. Ultimately, Robo Raven IIIv2 featured 22 solar modules that increased the flight time by 38 seconds representing a 14% improvement in endurance [42].

This version of Robo Raven III was also able to completely recharge the battery in 90 minutes. However, the integration of solar cells had an effect on the flight performance of the FWAV. The additional mass and increase in stiffness to the wings affected the wing deformations, which were necessary to achieve the shape changes responsible for aerodynamic performance. They also caused the motors to pull 2.2 W more than the original Robo Raven IIIv1 design, however an additional 7.4 W was produced by the solar cells resulting in an additional 5.2 W of power generation.

With infinite flight time being the ultimate goal, two approaches have been considered: (1) higher efficiency solar cells, and (2) integrating more solar modules into the FWAV. This paper focuses on the latter. By increasing the size of the wings to provide room for more solar cells and integrating solar cells into the body and tail of the vehicle, the harvested energy could be increased significantly. Integration of solar cells into the body should have minimal effects on the performance of the vehicle, whereas integrating solar cells into larger wings and the tail should have much more significant effect on vehicle's aerodynamic performance. This paper investigates ways to redesign Robo Raven to significantly increase the wing area for incorporating additional solar cells and adding solar cells into the tail and body.

5.2 Increasing Solar Cell Coverage by Increasing Wing Area

5.2.1 Designing and Building Larger Solar Wings

The carbon fiber spar arrangement utilized in this paper was based on a previously successful wing design [26]. This geometry allowed the wings to deform favorably under actuation. This spar layout was shown to be scalable when it was used for a larger platform [38]. Using this spar arrangement provides a good starting point when making further changes to the wings. The parametric design configuration is the same as shown in Chapter 3&4 and is shown again in Figure 5.2. It is repeated to show exactly how the designs differ. The angle between the spars is kept the same as the previous Robo Raven designs.

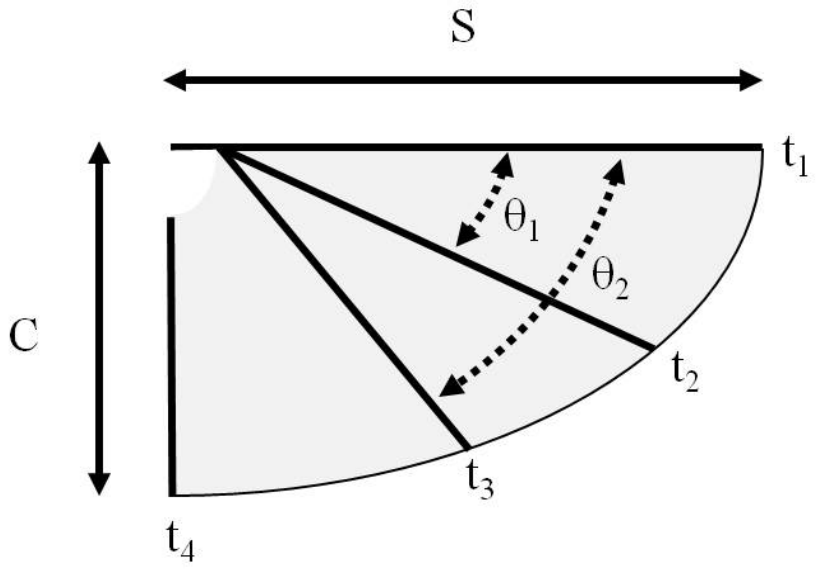

Figure 5.2: Parameters for wing design: S is the semi-span, C is the chord, and tn are the diameters of carbon fiber stiffening rods

The solar cell configuration for each wing design was also based on a previous successful design [47]. This design showed that keeping the rear of the wing free to deform allows the wing to maintain a shape under actuation that aid generation of aerodynamic forces. Moreover, adding solar cells to the front most part of the wing has the least effect on the deformation of the wing than integrating them anywhere else. When integrating solar cells into new wing designs, it is best to

integrate them from the front spar of the wing and expanding towards the rear. This configuration allows for wing to deform under aerodynamic loading and enable generation of appropriate aerodynamic forces.

In a previously reported study, we have investigated how scaling the wing size affects the performance [42]. Wings of 133%, 166%, and 200% of the size of the original Robo Raven wings were evaluated. An increase in performance was observed for the 133% and 166% wings but not for the 200% sized wings. Based on these findings, the 133% size wings and 166% size wings were considered as candidates for solar cell integration.

By increasing the stiffness and mass through the number and location of the solar cells, the deformation is more constrained and less aerodynamic force can be generated. Thus, a limit to the endurance gains was found to exist for the Robo Raven IIIv2 wing design (shown in Figure 5.3) when integrating solar cells into the wings. Therefore, in order to harvest more energy, larger wings are needed to increase the number of solar cells. However, increasing the number of solar cells and the wing area will not only alter the aerodynamic forces generated by the larger wing size, but also affect the flapping characteristics (e.g., flapping frequency and amplitude) due to the torque limitations of the servo motors. The maximum torque the servo can handle is 22 kg-cm. The closer the servos operate to the maximum torque, the slower they become until they eventually stall. The wings designed are not large enough or heavy enough to stall the servos. However, they were large enough to reduce the motor speed. Thus, a slight adjustment in the programmed frequency was used to

compensate for the slowing down of servos. Table 5.1 summarizes the characteristics of the new larger wing designs used in this investigation.

Table 5.1: Characteristics of the different wing designs

Wing Design	**Semi-Span (cm)**	**Chord (cm)**	**Wing Area (cm^2)**	**Mass (g)**	**Solar Cells**
Robo Raven I Wing	52.71	31.12	1017.3	15.3	No
Robo Raven III v2	52.71	34.57	1229.5	33.2	Yes
A	62.23	35.56	1368.0	19.3	No
AS	62.23	35.56	1368.0	45.2	Yes
B	66.68	39.37	1627.6	25.4	No
BS	66.68	39.37	1627.6	50.0	Yes

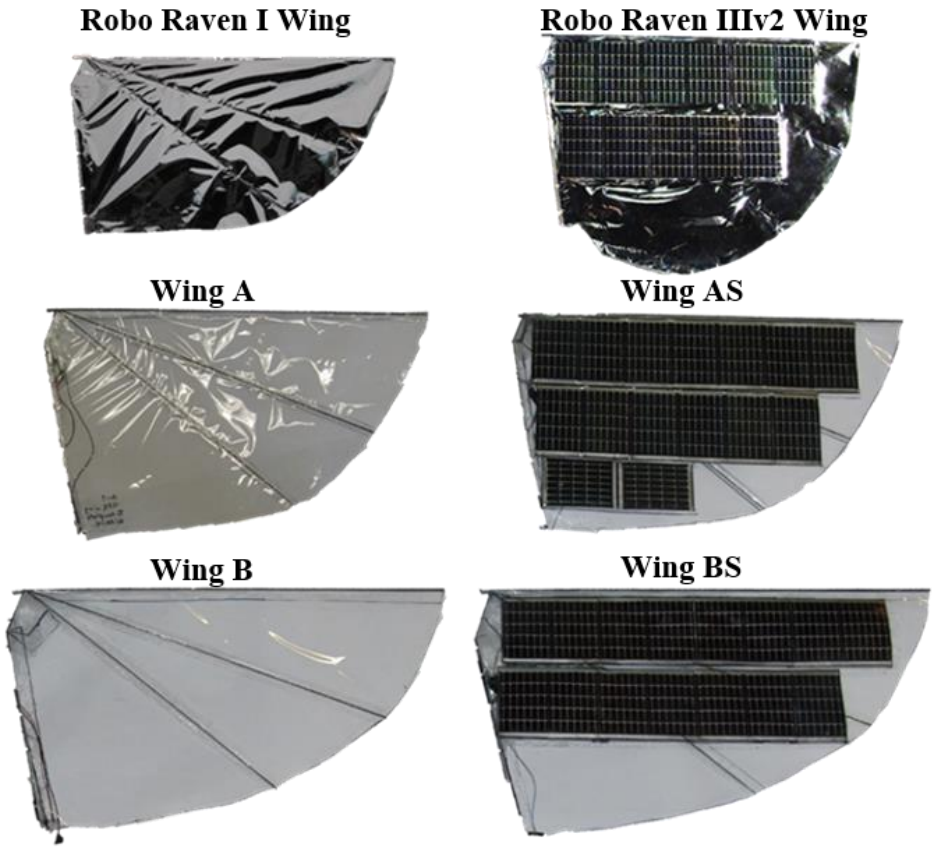

Figure 5.3: Wings designed, built, and characterized to determine the effects of solar cell integration on flight endurance for Robo Raven

Wings AS and BS are geometrically just like wings A and B respectively, except they have solar cells integrated into them. We use Powerfilm's© MPT6-75 solar cell modules. These are flexible 7.3 x 11.4 cm solar cell modules produce 50 mA of current at 6 V for a power output of 0.3 W. More efficient commercial solar cells are available, but they tend to be several orders of magnitude more expensive compared to the solar cells used in this investigation. Cost considerations prohibited us from using expensive high efficiency solar cells in our experimental studies. Low-cost solar cells can be considered as surrogate material for this study focused on the mechanical design.

Modifications had to be made to the solar cells to reduce the mass and the bending stiffness to be more compatible with the Mylar® membrane of the wings and tail. By removing the protective encapsulation on the solar cells, the bending stiffness of the solar cells was minimized, and the weight of the cells was reduced to approximately 1.8 g. The solar modules were connected to one another to make panels that fit on the wings. A total of 30 modules were integrated into the wings. A hole was made in the Mylar to fit the panels into the membrane of the wing. Once in place they were attached to the Mylar membrane and the spars were put in place to complete the wing. In Figure 5.3, the original wing designs for Robo Raven and Robo Raven IIIv2 are compared to the newly developed wings A, AS, B, and BS.

5.2.2 Modeling Performance Changes Based on Design Changes to the Wing

One important parameter for flapping wing flight is the Strouhal number [49]. It is a dimensionless number that is used to describe oscillating flow mechanisms. The formula for the Strouhal number (St) is shown in equation (5.1).

$$St = \frac{fA}{v_f} \tag{5.1}$$

Where f is the flapping frequency, A is the flapping amplitude in meters, and v_f is the forward velocity in m/s. It was found that a Strouhal number between 0.2 and 0.4 provided the most efficient flight for animals in nature [48]. The first design of Robo Raven was slightly under this metric. By increasing the Strouhal number, more efficient flight can be achieved. However, the servo motors used to actuate the wings constrained the available power to drive the wings. Increasing the size and mass of wings will cause the flapping amplitude to decrease for a given motor, as well as the

move the motor operation point to the low efficiency regime. Smaller amplitudes for flapping are detrimental to thrust production, since thrust relies on the volume of air that can be moved by the wings in the direction opposite to the forward velocity. In turn the velocity of any point on the wing moving through the air is a major factor in thrust production. The equation for the magnitude of the velocity profile, v, of the rotating wing is:

$$v = 2fr(\theta_{max} - \theta_{min}) \tag{5.2}$$

Where f is the flapping frequency, r is the distance any given point on the wing from the axis of rotation, and θ is the angle of the wing during the flapping cycle. This equation was adapted from the angular velocity of the wing and described in terms that can be used in predictive models. The velocity is limited by the motor torque motor. The power effects for the drag of the wing through air and against gravity were adapted from Wu et al. [28] and can be calculated as follows:

$$P = \int C_D \rho v^3 \, dA + mgc_g w \tag{5.3}$$

Where C_D is the drag coefficient of the wing, ρ is air density, A is the wing area, m is the mass of the wing, c_g is the center of gravity for the wing measured from the motor that actuates the wing, and ω is the angular velocity of the wing. However, power effects are expected to change under different operating conditions and for different wing designs. As described in previous findings [38], they can be easily transformed when the axis of rotation is reoriented to the angle of attack during flight. Therefore, the power effects can be accounted for when the velocity, mass of the wing, center of gravity, and flapping angle change for each wing design.

Our previous studies on compliant wing structures have shown that there is a direct correlation between spar deformations and thrust [25]. In these studies, analytical models of the wing shape and aerodynamic forces generated (F_L and F_T) due to drag during flapping have been employed and adapted from previous work, and then were modified to include aerodynamic lift as follows [26]:

$$F_L = \int C_D \rho v^2 \cos(\theta)\, dA + C_L S \rho v_f^2 \tag{5.4}$$

$$F_T = \int C_D \rho v^2 \sin(\theta)\, dA \tag{5.5}$$

where C_L is the coefficient of lift, S is the planform area of the wing, and v_f is the forward velocity of the platform. These equations describe the forces generated when the axis of rotation is in the direction of thrust due to the drag of the wing as it rotates, along with the lift generated as it is dragged forward through the air during flight. This model produced good correlation with observed trends in lift and thrust, which conformed to assumed characteristics of the wings generating these loads. Therefore, these models can be used to predict the changes in lift and thrust production for each wing design due to the integration of solar cells.

In addition, empirical terms have been employed for the thrust to account for the compliance of the wing while the wing captures air during its deformed state and pushes air towards the rear of the vehicle at the apex and nadir of the flapping cycle, known as the "blowback effect", as follows [38]:

$$\Delta F_D = (kf) \sin\left(\frac{\pi(\theta - \theta_i)}{\theta_f - \theta_i}\right) \tag{5.6}$$

$$v = \left(1 - \frac{D_f}{c\delta}\right) v_o \tag{5.7}$$

where ΔF_D is the change in total drag force that is decomposed into corresponding contributions to lift and thrust as given in Equations (5.4) and (5.5) based on the angle of attack, k is an empirical constant of proportionality previously determined to be 0.2, f is the flapping frequency, θ is the angle of the wing during the flapping cycle, D_f is the level of the drag force above the point at which the deformation transitions from global to local during blowback, c is the global stiffness of the wing, δ is the displacement of the mid-chord of the semi-span of the wing if it were infinitely rigid, and v_o is the corresponding rigid wing velocity. It is important to note that the contribution from ΔF_D to thrust and lift only occurs when the wing is near apex or nadir [25] and corrects for the duty cycle on force generation for the platform.

5.2.3 Wing Testing

Each wing was tested using a force measurement system similar to the one introduced in the previous chapter to determine the differences in force production. Using the same 6 degree-of-freedom (DOF) load transducer, the relevant lift and thrust forces associated with flight were measured simultaneously. Changes to the previous test stand were made to measure the lift and residual thrust generated by the vehicle. This test stand is set higher to compensate for the larger wings tested. The Delrin platform was also switched for a wooden structure to further eliminate vibrational effects. The test stand allows the vehicle to be pitched to a 20° incline to replicate flight conditions. The entire test stand is placed at the end of a wind tunnel to measure aerodynamic lift and residual thrust under actual flight conditions. The wind tunnel was set up to replicate the flight conditions of Robo Raven and its

inflight Reynolds number of 120,000. The test stand and its components can be seen holding the FWAV in Figure 5.4.

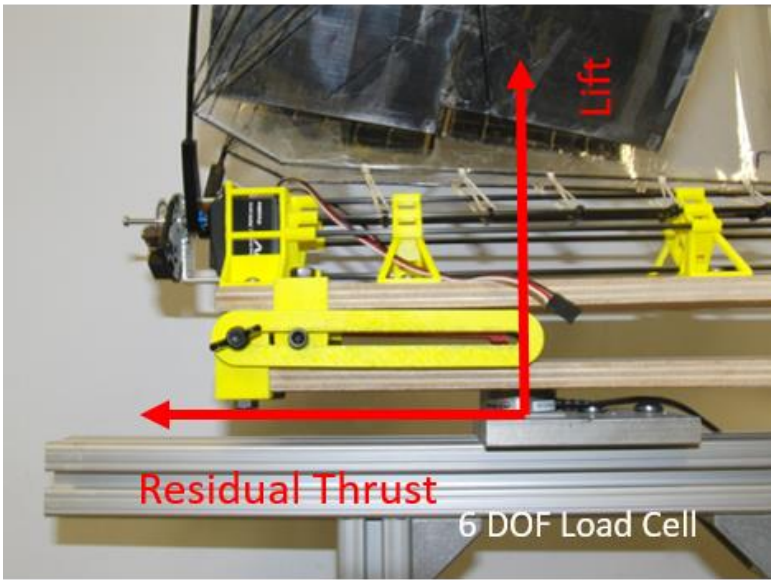

Figure 5.4: Test stand with residual thrust and lift directions identified. The ATI Mini40 6 DOF load cell is capable of measuring up to 40 N of force with a resolution of 0.01 N in the thrust direction and 120 N of force with a resolution of 0.02 N in the lift direction

In addition to measuring the aerodynamic forces generated by the wing during flapping, the test stand is also capable of measuring the position of the wings using an optical encoder to characterize the flapping range. All of the signals are simultaneously collected using a National Instruments NI DAQ-9188 data acquisition module. The raw data is sent to a LabVIEW VI that converts the raw signal to the actual loads being measured, and then the final loads are saved to an Excel template.

To effectively characterize the change in performance between the wing designs, tests were conducted over a range of frequencies with no tail attached. Larger wings were expected to perform better while flapping slower than the original wings, which flapped at 4 Hz. Therefore, each wing design was tested at 3, 3.25, 3.5, 3.75, and 4 Hz. The frequencies were measured in real time using the encoder on the

test stand and the LabVIEW VI software. The frequency was adjusted manually using a remote control until the desired frequency was achieved. A minimum of 3 Hz was required to maintain flight. A significant drop in flapping amplitude, and subsequent lift and thrust force generation, was observed beyond 4 Hz. To ensure the wings were operating at their peak performance, the FWAV was powered by a constant voltage power supply. The load cell measurements were then compared with model predications.

The load cell results from testing Robo Raven in a wind tunnel at speeds of 6 m/s were found to be representative of force production during actual flight after using a correction factor related to the difference in the actual flight conditions [47]. Integrating solar cells into Wing AS added 51.8 g, compared to its counterpart without solar cells (Wing A). The previously reported payload for Wing A was 46.8 g [42]. Therefore, the only way for Wing AS to maintain flight is if it could produce higher lift forces than Wing A. Wing BS weighed 49.2 g more than Wing B. Wing B had a previously reported payload of 76.6 g [42]. Therefore, Wing BS However could underperform Wing B by 27.4 g, and still maintain flight. The results from load cell testing are shown below and are compared to the predicted results from the wing models in equations (5.4) and (5.5).

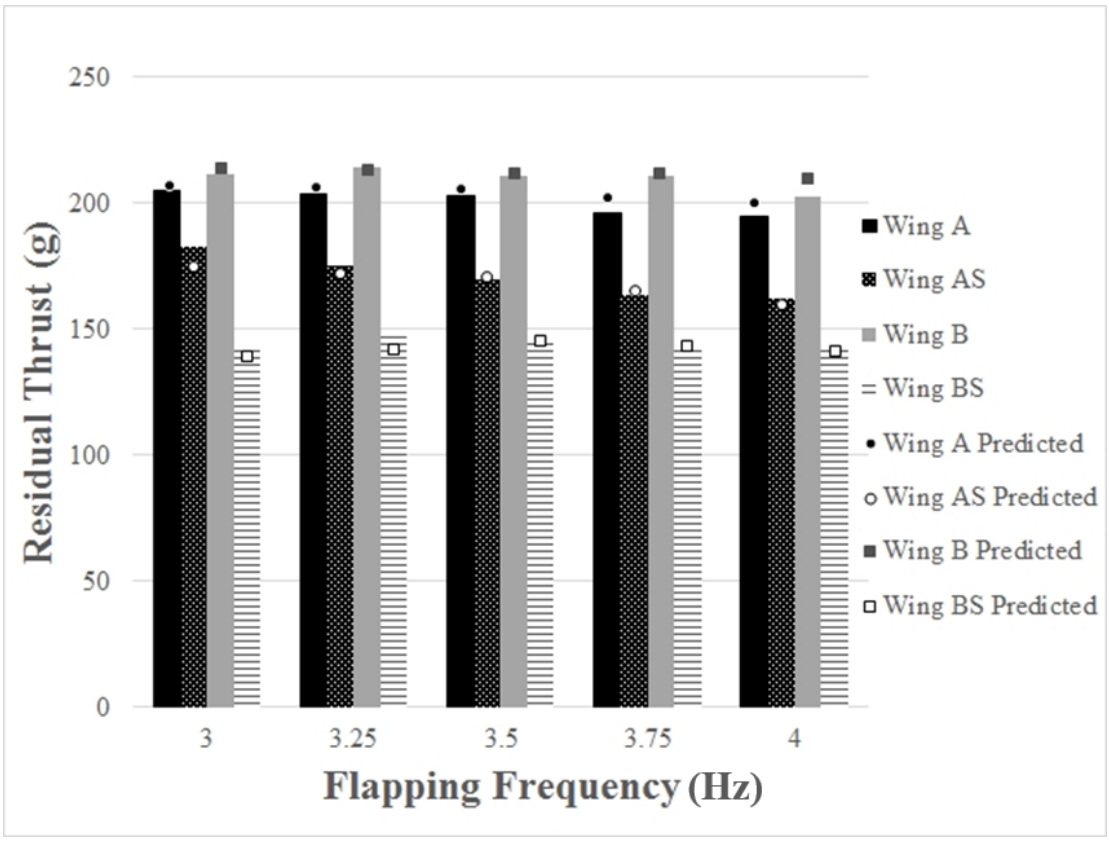
250
200
150
100
50
0
Residual Thrust (g)
3
3.25
3.5
3.75
4
Flapping Frequency (Hz)
Wing A
Wing AS
Wing B
Wing BS
Wing A Predicted
Wing AS Predicted
Wing B Predicted
Wing BS Predicted

(a)

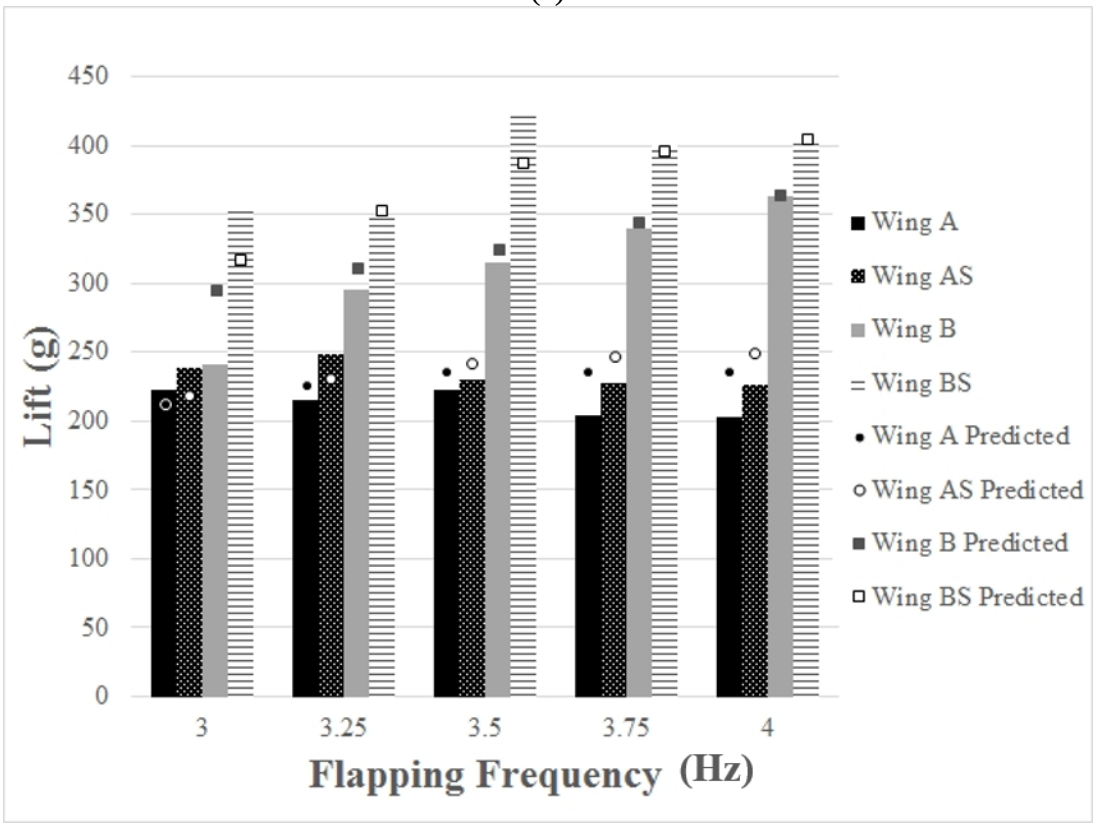
450
400
350
300
250
200
150
100
50
0
Lift (g)
3
3.25
3.5
3.75
4
Flapping Frequency (Hz)
Wing A
Wing AS
Wing B
Wing BS
Wing A Predicted
Wing AS Predicted
Wing B Predicted
Wing BS Predicted

(b)

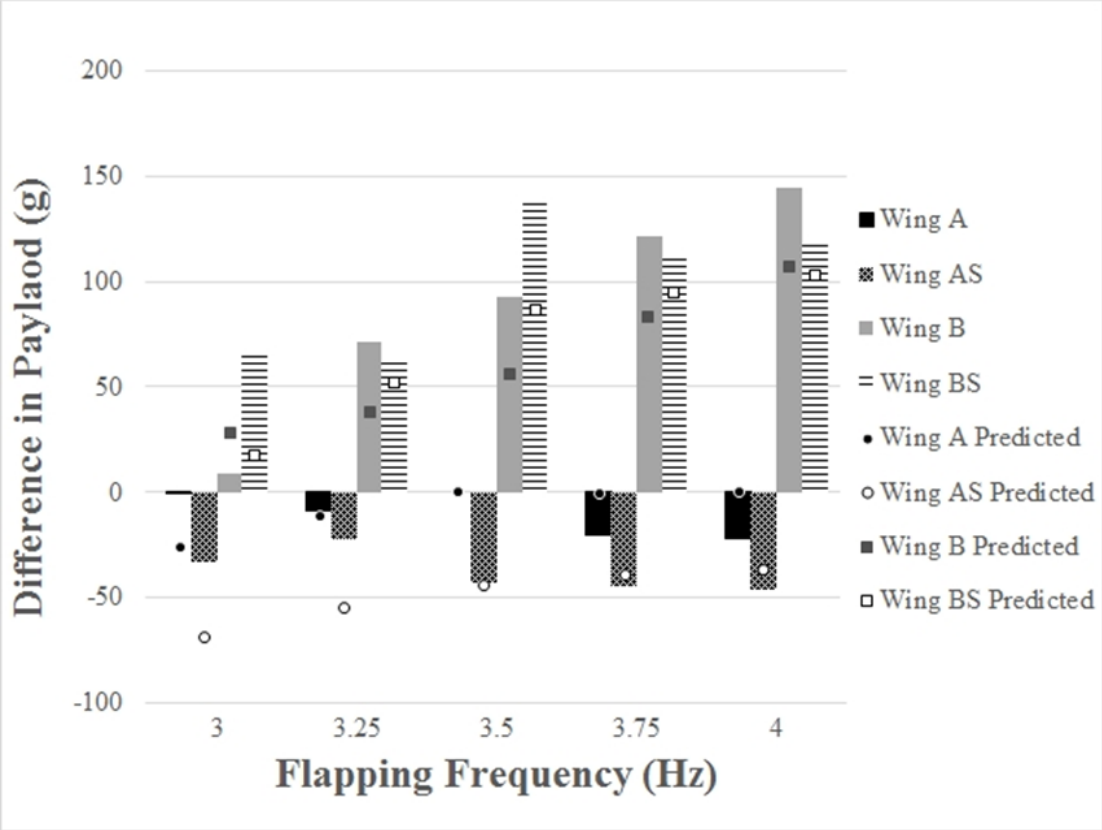

(c)

Figure 5.5: Load cell results and subsequent changes in payload capacities compared to predicted results from models for different wing designs: Top) Residual Thrust, Middle) Aerodynamic Lift, Bottom) Difference in Payload. Mass of each single wing: Wing A = 19.3g, Wing AS = 45.2g, Wing B = 25.4g, Wing BS = 50.0g

As the flapping frequency is increased from 3 to 4 Hz, the thrust decreased for each wing design. Wings with solar cells produced the least amount of thrust, however Wing BS produced the least amount of thrust where its non-solar powered counterpart, Wing B, produced the most amount of thrust. For each frequency that was tested, Wing A produced the least amount of lift, Wing AS the second least, Wing B the second most, and Wing BS produced the most amount of lift. The largest lift forces were observed at 3.5 Hz.

As previously noted, the weight of solar cells integrated into Wing A was beyond the inherent payload capacity of the wing design, so the increase in lift was

barely sufficient to achieve flight, as seen in Figure 5.5. On the other hand, the weight of solar cells added to Wing B was less than the inherent payload capacity of the wing design, and with the measured increase in lift and thrust, a total of 48.1 g of additional payload capacity was achieved by integrating solar cells into the Wing B design at 3.5 Hz. Further evidence of these effects was also observed during actual flight tests, where Wing AS was not able to climb and maintain flight while Wing BS was able to. By observing the Strouhal number for each wing design under each flapping frequency, the best overall flapping performance can be predicted that is consistent with the lift and thrust measurements.

Table 5.2: Strouhal number for each wing design under each flapping condition

	Strouhal Number				
	3 Hz	3.25 Hz	3.5 Hz	3.75 Hz	4 Hz
Wing A	0.192	0.198	0.224	0.220	0.199
Wing AS	0.175	0.179	0.182	0.180	0.178
Wing B	0.194	0.199	0.203	0.204	0.208
Wing BS	0.175	0.183	0.192	0.190	0.184

The models were also able to predict how changes in the wing design affected the vehicle performance. By using the actual recorded amplitude in the predictive models, the limitations imposed on wing performance by the available torque of the motors were simulated. The trends were all consistent with the actual trends observed with the measured data. The changes in thrust were larger than expected. The predictions for the wings with solar cells were lower than the actual measured values, where the predictions for the wings without solar cells were over the measured values. The lift model was slightly different. Where the predictive model suggested that the largest lift force would be observed by Wing BS at 4 Hz, it was actually measured with Wing BS at 3.5 Hz. This showed that we are reaching a torque

limitation in the servo motors that is accounted for by changing the flapping range used to calculate lift and thrust in the models. The models were able to predict that integrating solar cells would ultimately decrease the thrust produced and increase the lift. When solar cells are integrated into the wings, they stiffen the wings causing the wing deformations to decrease, subsequently reducing the amount of air the wings could capture and move towards the rear of the vehicle to produce thrust. On the other hand the increase in inertial forces due to solar cell integration can affect the aerodynamic forces generated during "transitions" in the flapping direction where a "whipping" effect that increases the contribution to both lift and thrust forces. The additional weight of the wings will also increase the moment acting on the motors, resulting in a great power draw from the servo motors while rotating the wings at a given frequency.

5.3 Increasing Solar Cell Coverage by Utilizing the Tail

5.3.1 Modeling Performance Based on Design Changes to the Tail

Integration of solar cell into the tail allows for several different tail designs to be developed and characterized. The solar modules chosen to be integrated to the body and tail are the same as those used for the wings. Based on the 676 cm^2 surface area of the original tail, it was possible to integrate a maximum of 4 solar cell modules. To provide uniform charging of the lithium polymer battery from each module, an even number of solar modules had to be introduced to the system. On the body there was enough space for 2-3 more solar cell modules. With this constraint, a maximum of 6 additional solar cell modules could be integrated into the system, since

2 modules are required in series to generate the 8.4 V necessary to charge the battery or operate the servo motors.

In addition to the wings, the tail also plays a crucial role in flight performance. Actuated by a small servo, it allows the vehicle to turn left and right. It also plays a role in flight stability, allowing the vehicle to maintain its pitch through the moment generated by the drag force acting on the tail. Therefore, integration of solar cells into the tail is expected to affect aerodynamic performance of the FWAV. The tail's effective drag changes with geometry. This alters the vehicle's ability to convert thrust force into aerodynamic lift. Two main design changes were identified that would allow for the tail to keep its current functionality while making it possible to integrate solar cells. First, the surface area of the tail can be increased. This change will cause more drag, and is expected to reduce thrust while increasing lift. However, it also allows for more solar cells to be integrated to the tail. The second aspect is the geometry of the tail, which can have its spread angle altered. This allows for different orientations of solar module integration to be tested, and for determining the effects of changing the drag moment by changing the width of the tail while maintaining a constant surface area.

In order to determine the effects of the tail design on the aerodynamic forces and moments generated during flight, it was necessary to develop an appropriate analysis. Using previously developed models for downwash effects on lift and thrust [48], predictive equations can be developed to describe tail effects on aerodynamic forces. Assuming that the vehicle has a constant forward velocity (i.e., steady state flight condition) and no pitch, the changes caused by the tail on the thrust force

generated by the flapping wings, F_{tT}, can be predicted from the drag and lift acting on the tail surface area by partitioning it. One portion of the wing, βA_T, will be in the blowback area of the wake of the flapping wings where the velocity increases to v_f+af proportion to the flapping frequency f. The other portion, $(1-\beta)A_T$ will be near the centerline of the body not exposed to the blowback, and experiences the normal forward velocity of v_f. The flapping frequency factor, a, can be determined by varying the flapping frequency. The portion of the tail exposed to the wake, β, is determined by flapping with and without air flow. Therefore, we can calculate the total change in the thrust force due to the tail as follows:

$$F_{tT} = \frac{1}{2} C_d \rho A_T [(v_f + af)^2 \beta + v_f^2 (1 - \beta)] \qquad (5.8)$$

where C_d is the drag coefficient determined from conventional drag equations for a plate with aspect ratio, AR, as follows:

$$C_d = \left\{ 1.28 \sin(\theta_T - \theta_0) + \frac{4\pi(\theta_T - \theta_0)^2}{\left[eAR\left(1 + \frac{2(\theta_T - \theta_0)}{AR}\right)^2 \right]} \right\} \qquad (5.9)$$

where θ_T is the pitch of the tail on the body of the FWAV, θ_0 is the angle of attack at which the drag goes to 0, and e is the efficiency factor of the shape. Therefore, a taller tail will have a lower value of β, and a wider tail will have value closer to 1. Similarly, the contribution to the lift force from the tail, F_{lT}, can also be derived similar to the drag force produced by the tail and the increase from the blowback effects from the wings:

$$F_{lT} = \frac{1}{2} C_l \rho A_T [(v_f + af)^2 \beta + v_f^2 (1 - \beta)] \qquad (5.10)$$

where the coefficient of lift, C_l, is given by:

$$C_l = 2\pi(\theta_T - \theta_0) / [1 + 2(\theta_T - \theta_0)/AR] \qquad (5.11)$$

5.3.2 Designing and Fabricating Solar Tails

To validate the effects of these design changes and the model, new tails with solar modules were designed and fabricated. Tail geometries were limited by the size of the solar modules integrated into tail. The new tails were designed to be as small as possible while still being able to integrate 3 or 4 solar modules. The 120° design was the largest angle that enables 3 modules to fit inside and the 90° design was the smallest angle that enabled 4 modules to fit inside the tail while still having a similar surface area to the 120° 4 module design. These four designs allowed us to characterize how tail geometry affects FWAV performance. The design specifications for each new tail design can be seen in Table 5.3 and a schematic of each geometry is shown in Figure 5.6. These tails were tested using the same force measurement system as the wings. However, to understand the drag effects of each tail design, one extra set of data with the vehicle parallel to the ground was collected.

Table 5.3: Specifications for solar cell tail designs

Tail Design	**Specifications**			
	Surface Area (cm^2)	***Angle (degrees)***	***Mass (grams)***	***Number of Solar Cells***
Original (0)	354	120	6.2	0
1	678	90	16.0	4
2	546	90	13.1	3
3	683	120	17.0	4
4	546	120	14.0	3

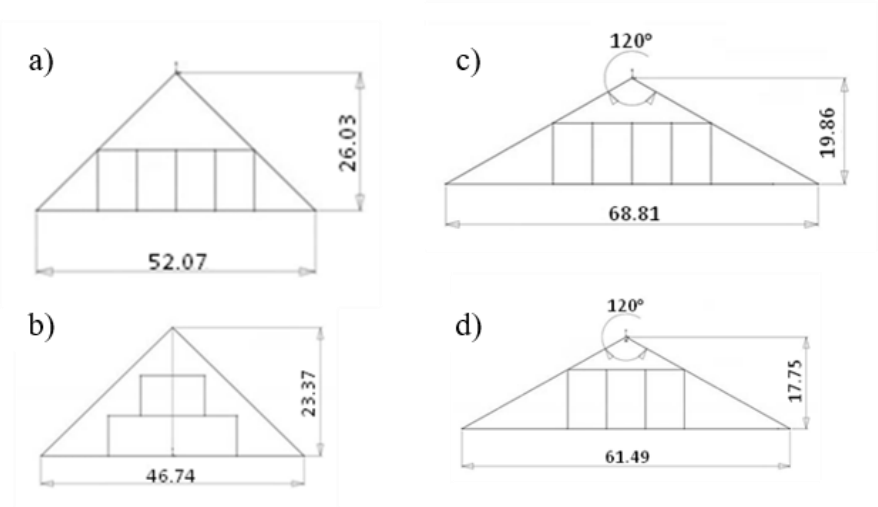

Figure 5.6: Solar cell tail designs that were tested: a) Tail 1 b) Tail 2 c) Tail 3 d) Tail 4 (dimensions in cm)

Each of these designs is expected to have different effects on vehicle performance. However the number of solar modules introduced to the FWAV system was constant because the voltage requirements limited the addition of solar cells to an even number. Thus, the new tail designs contribute up to 1.2 W of additional power, increasing the maximum power that can be generated to 10.8 W, or a 12.5% increase.

5.3.3 Tail Testing

The results from wind tunnel testing gave new insights to the benefits of each tail design. The lift and thrust loads produced by each tail design under the 4 conditions were found with a wind velocity of 6 m/s, which is consistent with the velocity of the FWAV during flight. By comparing the drag at 0°, thrust at 20°, lift at 20° we can characterize the role of tail in the vehicle flight.

The static response of each tail is consistent with the physics of drag and the model. A larger tail is expected to create a larger drag force in the wind tunnel. That is evident when comparing the tails that simply differ in the amount of solar modules integrated. If the geometry of the tail is the same, the tail with more solar modules

and a larger surface area will create more drag. This can be observed in the drag results for each tail design presented in Figure 5.7. The 120° angle spread tails generate more drag than their 90° spread counterparts. Tail 1 and Tail 4 have the same amount of solar modules but the 120° spread tail generates more drag. The same observation can be made when comparing Tails 2 and 3, but with 4 solar modules instead of 3. The 90° tails have longer spars that give the vehicle a larger height, thus the aerodynamic forces on the taller tails create larger drag moments causing the spars to bend into a more aerodynamic shape. This aerodynamic shape and bending means that less surface area is orthogonal to the incoming airstream, creating less drag for the vehicle, which is why the drag for Tail 1, the tallest tail design tested, is so low compared to the predicted model.

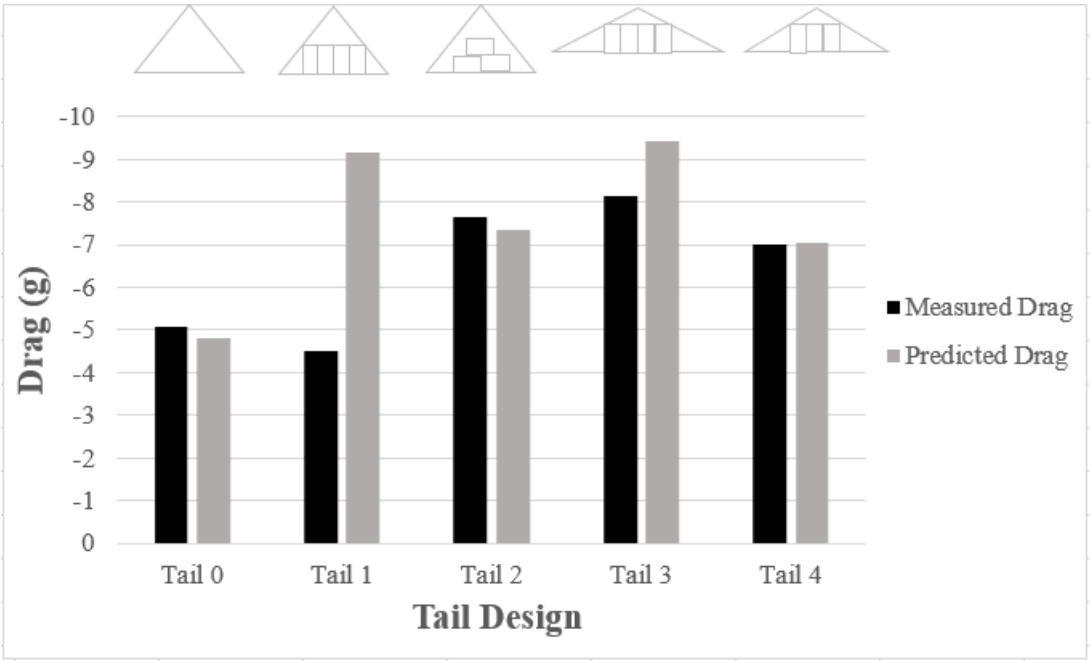

Figure 5.7: Comparison of the drag from each tail design while wings are stationary and vehicle at a 0° angle of attack

The static response of the vehicle while completely horizontal was observed for each tail design and measured. However, in actual flight the FWAV has a pitch of

20°, and additional drag forces are generated by the tail because of the blowback from the flapping wing that results in thrust. The best way to understand these effects is to run the same test with the FWAV at a pitch of 20° with the wings flapping at 3.5 Hz. Since the wings are flapping, a net positive residual thrust force is expected to overcome the drag. This residual thrust exists because the air speed of the wind tunnel is not high enough to equate the average thrust force generated. The effects of the wings for these tests can be seen in Figure 5.8. It is clear that 90° tails have less of a drag effect on the FWAV while flapping. This is due to the tails being narrower and capturing less of the air generated by the flapping wings. All of the 120° spread tails experience a larger drag force, thus generating a smaller thrust force. When comparing just the 90° tails, the effects from surface area are intuitive. The larger 90° tail (Tail 1) causes a larger drag force, thus a smaller residual thrust is observed than the smaller 90° tail (Tail 2). The opposite seems to be true for the 120° tails. The smaller tail (Tail 4) with a smaller surface area and fewer solar modules has the higher drag force than its 4 module counterpart (Tail 3). This can even be seen with the original tails with no solar modules, where it generates the largest drag force. The larger 120° tail is more susceptible to the air blown back by the wings flapping allowing the tail to bend slightly more than the smaller wing. This more streamline shape causes less drag at a 20° pitch. The model was able to take the geometry of the tail and predict what would happen to the thrust force for each of these changes (see Figure 5.8).

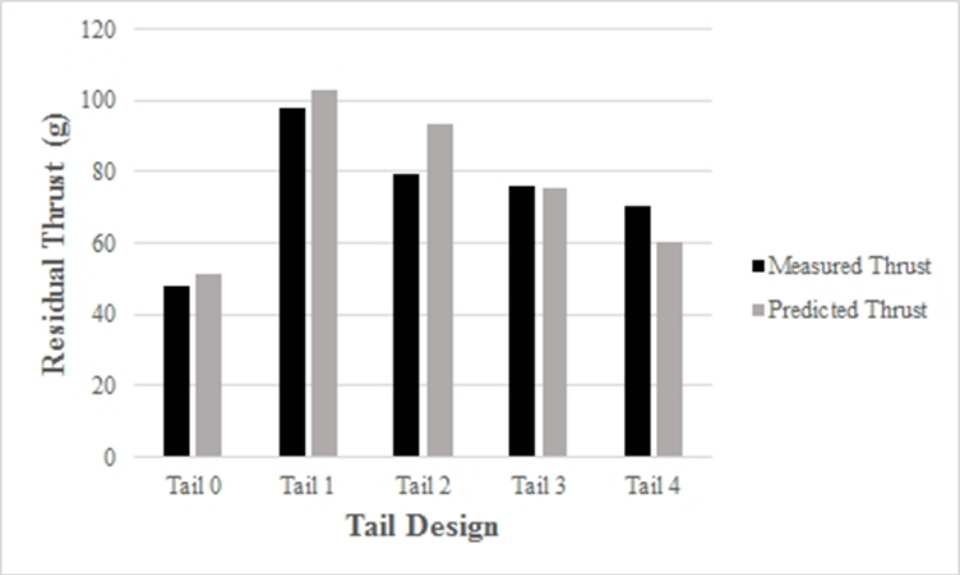

Figure 5.8: Comparison of the residual thrust from each tail design while wings are flapping and vehicle pitched at 20°

The thrust forces with the FWAV at a 20° pitch are clearly shown. Given the position of the vehicle and that incoming air is present the thrust result make sense. The tail plays a major role in lift generation. The tail of the FWAV is positioned at a 45° incline relative to the body. During flight, incoming air generates a moment with the tail that causes the FWAV to have a pitch of 20°. Tails of different shapes, sizes, and design are expected to have an effect on lift generation. The lift results, seen in Figure 5.9, help to further explain the effects of these different designs. When comparing the tails against each other they are the complete opposite to the thrust results. Excluding the original tail, the tail that provided the smallest thrust actually provided the most lift. Tail 3 and 4 were both 120° spread tails and generated the most lift. Since these tails are wider, they are able to capture more of the air generated by the wings flapping. The same effect that caused more drag and reduced thrust assisted in generating more lift. This is what the model predicted and this is exactly what was seen by the measured results.

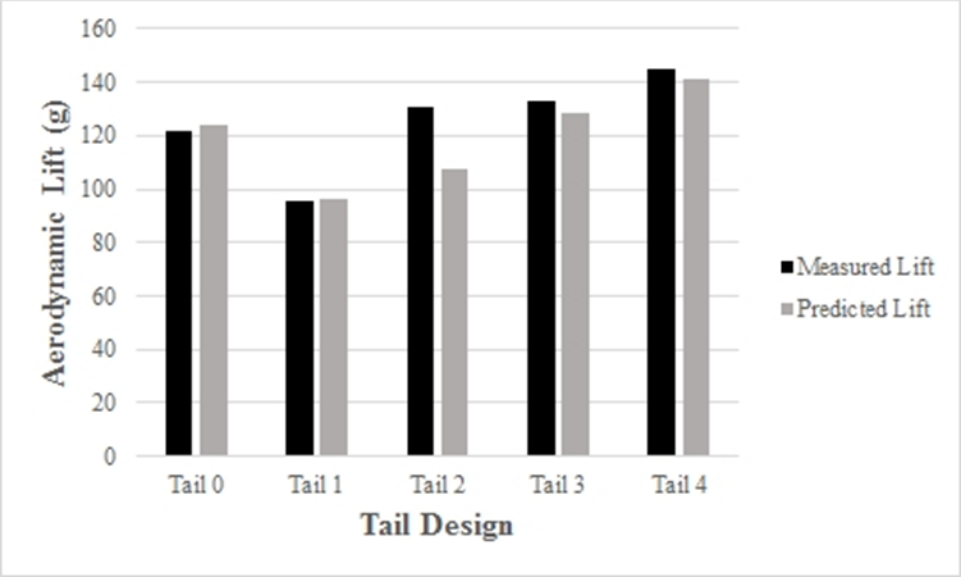

Figure 5.9: Comparison of the lift from each Tail Design while wings are flapping and vehicle is pitched at 20 degrees. Mass of each tail: Tail 0 = 6.2g, Tail 1 = 16.0g, Tail 2 = 13.1g, Tail 3 = 17.0g, Tail 4 = 14.0g

Wind tunnel testing provides a comparison amongst the five tail designs. This new information allows improvements in actual flight performance and payload can be estimated. Using the known payload with the original tail, the payload can be estimated for the new tail designs. These predictions can be seen in Table 5.4.

Table 5.4: Payload calculation from total force generation

Tail Design	FWAV Mass (g) Including Battery	Total Force Generated (g)	Estimated Total Flight Weight (g)	Estimated Payload (g)
0	346	131	367	21
1	364	137	373	9
2	362	153	389	27
3	365	153	389	25
4	363	161	397	34

Each of the new tail designs should be capable of generating enough force for flight. In fact, an increase in payload of up to 57% can be expected from all of the new tail designs except for 1. Tail design 4 was found to produce the greatest energy increase with 120% more than the original tail design 0 that did not have solar cells.

These estimations were confirmed during actual flight tests, where it was observed that the vehicle was able to fly with each of the tail designs. From load cell tests, integrating Tail 4 for our design would produce the best results and was the tail chosen for integration. This version of Robo Raven III with the same 22 solar module wings as Robo Raven IIIv2 and solar cells integrated into the tail and body of the vehicle was named Robo Raven IIIv3.

5.4 Increasing Solar Cell Coverage by Utilizing Body

Integration of solar cells into both the wings and tail are expected to have significant effects on the flight performance of the FWAV. However, integrating solar cells into the body should have a minimal effect on vehicle performance. The integration of solar cells into the body should simply add mass to the system, which takes away from the payload capacity, and does not affect the force generation or aerodynamics of the wing and tail structures. To integrate solar modules into the body, it was necessary to design two mounts that allow solar modules to attach to the carbon skeleton of the FWAV's body, but allow as much area as possible to orient towards the sun.

Tail mount that houses the tail servo was re-designed to provide a surface for the solar cells to be attached to the top of the vehicle. Another mount was designed as a simple clip with the same surface to hold the other end of the solar cell panel. Depending on the configuration of solar modules used for the tail (3 or 4), 2 or 3 modules were used to create the solar panel to be integrated with the two body mounts. The new mounts for the solar cells added 4.4 grams to the vehicle. The two module configuration adds a total of 7.8 grams to the FWAV and the three module

configuration adds 9.5 grams to the system (1 solar cell module = 1.7g). The integration of the 6 new solar modules to the body and tail of Robo Raven IIIv3 can be seen in Figure 5.10.

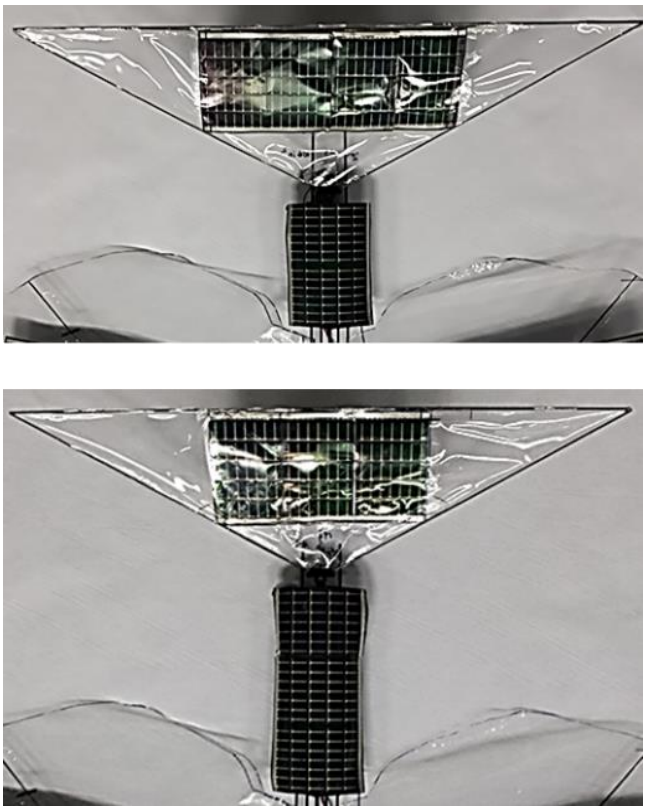

Figure 5.10: Two different design configuration for integrating 6 additional solar cell modules: (Top) 2 modules in body, 4 modules in tail; (Bottom) 3 modules in body, 3 modules in tail

5.5 Results and Discussion

5.5.1 Flight Tests

The fabricated wings and tails were all flight tested to validate the results from load cell testing. Each wing design that did not have solar cells was tested first to determine their fundamental flight capability. The best metrics to observe the best flight were the vehicle's climb rate and total flight times. A design with a fast climb rate shows good aerodynamic force production and affords a higher payload capacity.

Consistent with load cell results, it was determined that Wing B flew the best. It clearly had a faster climb rate than Wing A. However, the first new phenomenon observed was that the larger wings seemed to operate better while flapping slightly slower than the smaller wings where they could achieve the desired flapping range with the torque-limited servo motors.

Next, the wing designs with solar cell were tested. It was determined that Wing AS was not able to maintain flight due to an inability to achieve sufficient lift to maintain an adequate climb rate. This flight behavior was consistent with the results from load cell testing, because Wing AS produced only slightly more lift than Wing A, which was inadequate to carry the additional 51.8 g from the solar cells. However, Wing BS were able to produce enough extra lift and thrust to maintain flight. The total payload for these wings must have only been slightly greater than the 51.8 g of the solar cells, because there was a notable decrease in overall vehicle performance.

Flight testing the new tail designs with the Robo Raven III v3 wings was consistent with the results observed from load cell testing. First, the FWAV was able to fly with each new tail design. However, the worst flight was with Tail 1. It simply did not climb like the others. It had a notably slower climb rate. Due to changes in wind and condition variability, it was not possible to observe many more differences in performance between the tail designs. However, from our load cell results Tail 4 was chosen to be the best design. Using Wing BS and Tail 4 designs, Robo Raven IIIv4 was built and flown, and is shown in Figure 5.11.

Figure 5.11: Robo Raven IIIv4

This final Robo Raven IIIv4 design was thoroughly flight tested to determine its flight characteristics. With the improvements that went into this design, a total of 36 solar modules were successfully integrated into the wings, tail, and body of this FWAV. This final design was able to maintain flight. The FWAV weighed 361.4 grams without the battery. With the battery, the vehicle weighed 388 grams. The vehicle was able to carry an extra 6 grams before it would no longer climb. The flight characteristics of Robo Raven III v4 are shown in Table 5.5 below and compared to the original Robo Raven design.

Table 5.5: Flight Characteristics of Robo Raven and Robo Raven IIIv4

Flight Characteristics	Robo Raven [26]	Robo Raven IIIv4
Vehicle Mass	263.3 g	361.4 g
Forward Velocity	7 m/s	5.6 m/s
Climb Rate	0.53 m/s	0.23 m/s
Turning Radius	6.1 m	5.5 m
Payload (without batteries)	54 g	32.6 g

As seen in Table 5.6, the FWAV with 36 solar modules produced 10.8 W. However, since the wings were larger, they required more current from the battery. Where the previous version took 4.5 minutes to deplete the battery, the larger wings took 3 minutes and 45 seconds due to the aforementioned increase in torque required to drive the heavier wings. The 36 module FWAV flapped for 4 minutes 35 seconds. This 50 second increase demonstrated a 22.2% increase in total flight time, which is a 46% increase over the previous design. It is important to note that these measurements were conducted at the highest flapping frequency of 4 Hz (due to limitations of the remote control used outdoors), and that lowering the flapping frequency decreases power consumption and increases flight time while also generating optimal aerodynamic force at a frequency of 3.5 Hz as previously reported.

Table 5.6: Flight Time Results for Different Numbers of Solar Cell Modules

Robo Raven Version	Number of Solar Cell Modules	Maximum Power Generated (W)	Increase in Flight Time(sec)	% increase
Robo Raven I	0	0	0	0
Robo Raven III v2	22	6.6	38	15.2
Robo Raven III v4	36	10.8	50	22.2

5.5.2 Battery Recharge Tests

While wind tunnel testing provided new insight into the change in flight performance for different design changes, the electrical benefits of adding solar cells to the FWAV needed to be characterized as well. The solar modules were expected to extend the flight time of the FWAV and decrease the recharge time for the battery. Outdoor tests were conducted to determine the effects that the 36 modules will have on harvesting solar energy.

To measure flight endurance, the FWAV was flapped outdoors until the battery was completely depleted. The FWAV was held in place with the normal surface of the wings pointed directly at the sun before the test began. This ensured that the photovoltaic cells were exposed to the maximum amount of sunlight for maximum power production. Upon plugging in the battery, the FWAV started flapping and a timer was started. The timer was stopped as soon as the FWAV stopped flapping due to the lack of power. These times were recorded and compared. To measure the recharging time of the FWAV a recharging circuit was built to safely recharge the battery to full charge. A zener diode with a breakdown voltage of 4.3 V was used as a voltage regulator. This value is necessary as the charging voltage of the Lithium Polymer battery is limited to 4.2 V per cell. The resistor in the circuit is

placed to dissipate power so a 1.3 W zener diode can be used instead of a higher wattage. This circuit is designed under the assumption that the solar panel acts primarily as a current source at constant voltage. A schematic of the recharging circuit used to test the recharging capabilities of the 36 module design is shown in Figure 5.12.

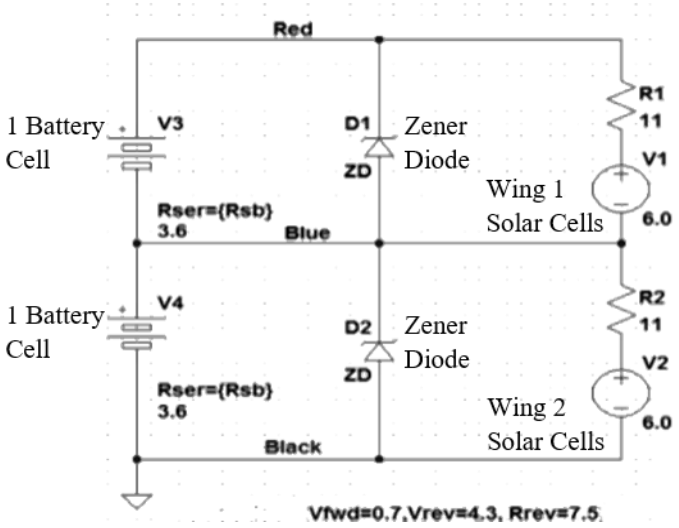

Figure 5.12: Recharging circuit that regulates voltage going to the battery for safe recharging where 4.2V are supplied to the battery at the blue node and 8.4V are supplied at the red node

The 2 cell Lithium Polymer battery uses a three node plug for safe charging. However, the consequence of charging a single battery using this recharge circuit is to reduce the effective charging current from 600 mA to only 300 mA. Furthermore, the maximum power output is also not maintained since the voltage is decreased to a limit of 4.2 V. This obviates the advantage of using a Maximum Power Point Tracking circuit. However, commercially available MPPTs have a negative effect on FWAV performance by increasing weight beyond the payload capability. In this circuit, the battery is charged only when the D2 diode has a minimum of 4.2 V across it and D1 has a minimum of 8.4 V. Current flows from high voltage to low voltage, so

the solar cells must always be higher than the voltage of the battery. The diodes are capable of reaching the minimum voltage even on a party cloudy day. It is expected that on an overcast day the diodes would not give enough solar power to reach the required voltage. Testing was conducted with a measured solar flux of 102 mW/cm2 (i.e., full sun) in order to prove the solar cells were capable of charging the battery.

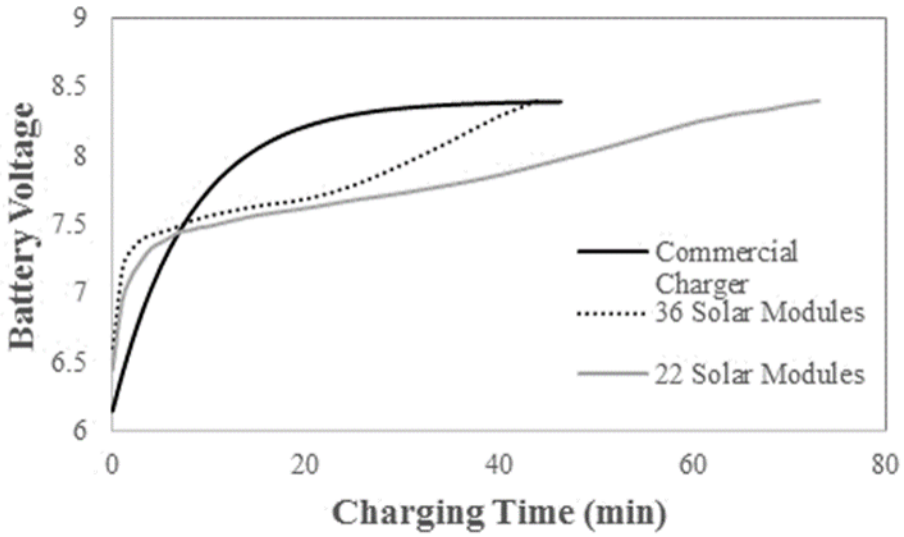

Figure 5.13. Comparison of recharging results

The total recharging time of the 22 module FWAV was previously found to be 73 minutes. The new 36 module FWAV was able to recharge a depleted battery in 44 minutes. More solar cells allow for more current to be transferred to the batteries. With a power increase of 4.2 W, or 64% more power, we were able to recharge faster than a typical LiPo battery charger (Figure 5.13).

5.6 Conclusions

This chapter investigates the tradeoff in flight performance when changing the design of wings and tail in FWAVs to integrate solar cells for harvesting energy and enhancing flight endurance. New wings were designed to successfully fly with the

amount of solar cells integrated. To utilize all the surface area available, solar cells were integrated to the body and tail of the vehicle. Even though the effects of integrating the solar cells to the body were negligible, the effects of integrating solar cells to the tail and wings were significant.

Predictive models were implemented and shown to predict how changes to the wings and tail can affect performance. These models can be used for other FWAVs that are forward flying and rely on a deforming membrane to generate thrust. Using larger wings allows greater forces to be generated. However, integrating solar cells increases the inertial effects of the wings and stiffens the wings. Therefore, appropriate design of wings to achieve the necessary deformations during flapping was determined to be key to producing adequate thrust and lift for flight performance when solar cells are integrated into the wings. Thus, a properly designed wing that is larger and heavier due to solar cell integration was shown to achieve better flight performance than one that is smaller and lighter, while also providing the wings with the ability to harvest solar energy.

This study also investigated improving performance through altering the FWAV tail design and integrating solar cells into them. It was determined that the spread angle between the spars had the greatest effect on aerodynamic forces, where a tail spread of 120° will produce more lift and less thrust than a tail with a 90° spread of the same surface area due to these tails capturing more of the air pushed back by the flapping wings. Based on how a FWAV is performing, the tail can be altered to accommodate the necessary tradeoff in lift and thrust that is characteristic of the tail design as follows: (a) a wider tail can be used to generate more lift from faster

moving air associated with the blowback effect from the wings, while (b) a narrower tail can be used to generate more thrust by avoiding this effect.

The resulting Robo Raven IIIv4 design produced 10.8W of the 37W needed for continuous flight during sunlight. The flexible Amorphous Silicon cells used are only 5-6% efficient. Flexible Gallium Arsenide cells that are 28-30% efficient would produce a total of 54W using the same vehicle design while only adding 5g to the total vehicle weight. Realizing this design with GaAs cells would allow us to achieve flight using only solar cells during sunlight.

Lessons learned from this study will be applicable to the broad FWAV community. Wing deformation significantly affects the production of aerodynamic forces. Integration of solar cells should be done to minimize the negative impact on the wing deformation during the flapping cycle. Our studies show that it is better to integrate solar cells towards the front spar of the wing. Bigger wings help in harvesting more energy, but they also need more power to flap at higher frequencies, as evidenced by a significant drop in flapping amplitude and subsequent lift and thrust generation. The approach described in this chapter can be used to find the right size of solar integrated wings for a given actuator.

Chapter 6: Designing a Flapping Wing Air Vehicle Capable of Continuous Solar Flight by Integrating High Efficiency Photovoltaic Solar Cells

This chapter is completed work that has yet to be submitted. Up to this point, flexible solar cells have been integrated into the wings, body, and tail of our flapping wing air vehicle. The solar cells have allowed the vehicle to stay in flight for longer periods of time and allows for the battery to recharge without using a battery charger. However, the technology used in the previous versions of Robo Raven III use amorphous silicon solar cells that have an efficiency of 6%. Using flexible high efficiency solar cells, creating a FWAV that stays in flight using only solar power is possible. This paper investigates more efficient photovoltaic technologies and establishes GaAs photovoltaic solar cells as the best option going forward. A model that predicts the mechanical performance due to a change in stiffness and material used in the wings was developed. A new wing design using a material similar to the GaAs commercially available as developed, tested, and flown. The new wing design was lighter and more deformable than the previous version allowing for better performance. By actually integrating the GaAs solar cells in place of the mock material, the first FWAV capable of flying continuously in sunlight can be developed.

6.1 Introduction

A major drawback of flapping winged flight is the continuous need of power to keep the vehicle flapping. Typically payload is extremely limited since flapping winged flight is challenging to achieve and the vehicle must be as light as possible to maintain flight. With a limited payload, the battery that is used to power the vehicle is

typically small. This small battery can only store so much energy which usually results in short flight times. Shorter flights restrict the UAVs overall mission capabilities. If the vehicle could harvest energy while in flight, the UAV would have longer flight times. Harvesting enough energy would allow the UAV to stay in flight indefinitely.

The previous versions of Robo Raven III demonstrate the development of solar cell integration into our Robo Raven vehicle. Robo Raven III v1 was an investigative study to see if solar cell integration was possible. By achieving flight and increasing flight time, we knew that solar cell integration was a viable way to increase flight time. To investigate the limitations of solar cell integration, the solar cell wings were redesigned for Robo Raven III v2. This design consisted of 11 solar modules integrated to each wing. This was the maximum amount of solar cells that could be integrated into the original Robo Raven wings and still maintain flight. Robo Raven III v3 consisted of the same wings developed for Robo Raven III v2 however, with solar cells integrated into the body and tail of the vehicle. This allowed 6 more solar cells to be integrated into the vehicle. This also demonstrated just how important the tail of the FWAV is for generating lift. The different tail designs tested gave new insight to how the tail translates the thrust generated by the wings into aerodynamic lift.

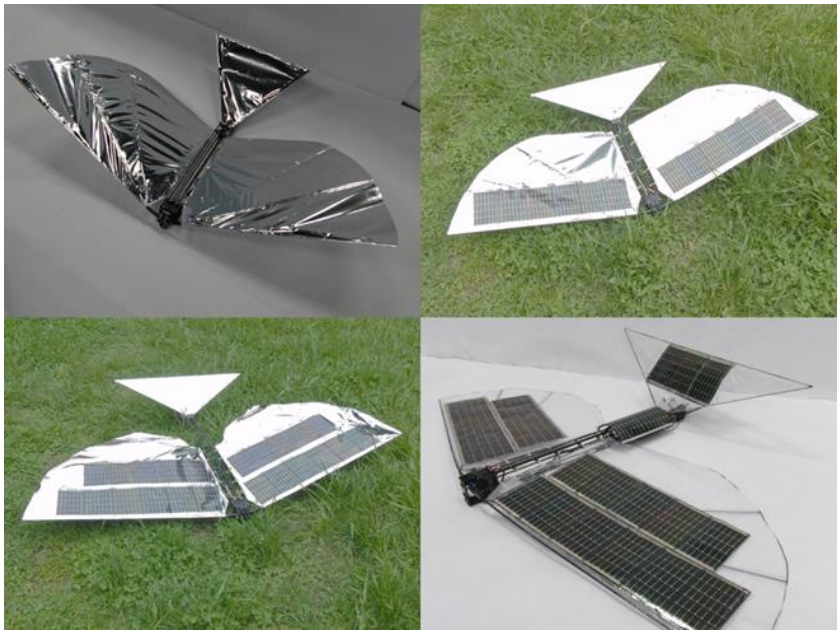

Figure 6.1: Previous Robo Raven & Robo Raven III design: Top left: Robo Raven I, Top right: Robo Raven III v1, Bottom left: Robo Raven III v2, Bottom right: Robo Raven III v3

With Robo Raven III v3, the total available surface area of the original Robo Raven design was completely saturated with A-Si solar cells. However, with 28 A-Si solar modules, the FWAV was harvesting a maximum of 8.4W while it was consuming 37W. For completely solar powered flight the FWAV would need to harvest 37 or more Watts. Using the same solar cell technology, the best option was to increase the available surface area for solar cell integration. By designing larger wings for the FWAV we can increase the surface area while also generating more thrust and lift. A previous study [42] observed the effects of using larger wings for Robo Raven. It was found that larger wings can actually generate larger forces while flapping at a slower rate than the current design. However, going too large can be detrimental since the flapping is limited to the torque the motors can output. Another study was done where solar cells were integrated to larger wings for a Robo Raven III design that would carry the maximum amount of solar cells [51]. The largest wings

that allowed the most amount of solar cells to be integrated were found. These wings had a wingspan that was 66% larger than the original Robo Raven wings. This allowed a total of 30 A-Si solar modules to be integrated into the wings. With the additional solar cells on the body and tail of the FWAV, a total of 36 solar modules made up Robo Raven III v4. Producing a total of 10.8W, we are producing 29% of the energy we need for completely solar flight. At this point, the limits of A-Si technology has been reached. New more efficient materials must be investigated to help reach the goal of completely solar flight. However, integrating different materials, instead of the A-Si solar cells that are currently integrated, is expected to alter the way the wings deform, thus changing the performance of the FWAV. A new investigation must be done where different solar cell technologies are tested and their effects on wing performance are estimated, measured, understood, and modeled.

6.2 Solar Cell Technologies

6.2.1 Amorphous Silicon Solar Cells

For photovoltaic solar cells to be a viable method for energy harvesting, thin flexible solar cells must be used for the wings to deform correctly and generate the lift and thrust necessary for flight. Currently Amorphous Silicon (A-Si) solar cells are being integrated into the wings. The specific solar modules chosen for integration were provided by Powerfilm Inc. They provide several off-the-shelf models to choose from. To steadily increase the number of modules integrated into the body while still providing an appropriate voltage, model MPT6-75 was chosen. This module had an operating voltage of 6V and an operating current of 50mA. Each module can cover an area of 72.5mm by 111mm. The A-Si modules have a protective encapsulation to

protect the surface of the solar cells. With the encapsulation each module weighed 2.0 grams and had a thickness of 0.18mm. However, the encapsulation made the cells too stiff when compared to the Mylar membrane of the wings. By removing the encapsulation, the stiffness of the solar cells was reduced as well as shedding a considerable amount of the module's total weight. Each module now weighed 1.6g while the thickness was reduced to 0.14mm. This was a 20% drop in mass and 22.2% drop in thickness. These solar cells have proven to be a material that can be integrated into the wings of a FWAV. However, producing a FWAV that would fly continuously in sunlight would be impossible with the low amount of electrical energy produced with these cells. These A-Si cells were found to be 6% efficient under the best conditions. While the MPT6-75 modules were the perfect candidate for exploratory research, their lackluster electrical performance influenced further investigations into more efficient photovoltaic technology.

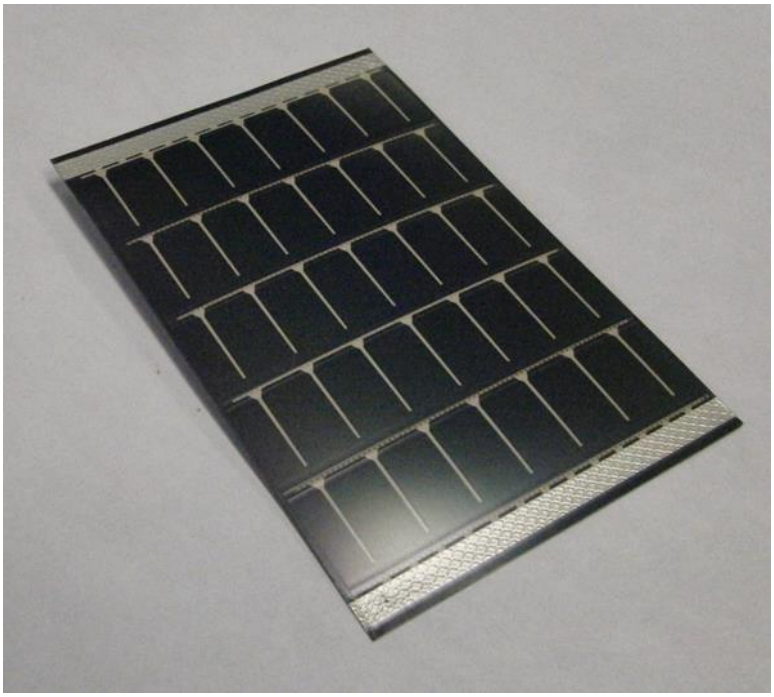

Figure 6.2: Powerfilm MPT6-75 A-Si Solar Module

6.2.2 Semi-flexible Polycrystalline Solar Cells

The next photovoltaic solar cells considered for integration into FWAVs were polycrystalline solar cells. These semi flexible solar cells were 17.6% efficient. The solar cells are silicon based and the silicon material is melted then poured into a mold. As the silicon cools, it crystalizes in an imperfect manner. The grains of the crystals can actually be observed on the surface of the solar cells. On the back side of the cells is a thin piece of aluminum that serves to electrically connect each of the cells together. These cells are not as efficient as monocrystalline solar cells, but are more flexible. These solar cells came in various sizes but the cells we observed were 8cm x 15.5cm and weighed 6g. If the A-Si solar cells were simply swapped out for the polycrystalline solar cells, the FWAV would be harvesting 31.7 Watts of the 37 needed for continuous solar flight. However, these solar cell feel much stiffer than the A-Si cells and proved very difficult to integrate. When these cells were integrated into the wings, they shattered during the wing fabrication process. By being very careful and gentle during the wing fabrication process, we were able to complete a set of wings with these solar cells. However, when it came to flapping these wings, the cells shattered while flapping.

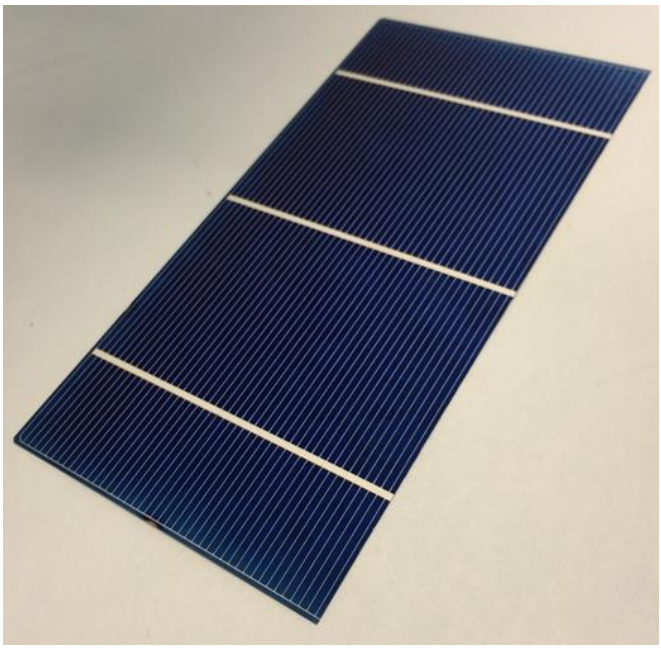

Figure 6.3: Polycrystalline Solar Cell

6.2.3 Gallium Arsenide Solar Cells

The final solar cell technology that was considered for integration were gallium arsenide (GaAs) photovoltaic cells. The manufacturer use a metalorganic chemical vapor deposition process to grow a thin layer of GaAs, then remove this thin layer via an epitaxial lift-off (ELO) process which leaves a thin, flexible, and lightweight solar cell. These thin film flexible solar cells can be up to 30.8% efficient if they are dual junction, however the single junction cell observed was 24% efficient. The flexibility of these cells are more comparable to the flexibility of the A-Si cells. Comparing the efficiencies of these two cells, completely solar flight could not only be achieved by these solar cells, but with less surface area than the total surface area of solar cells in the current Robo Raven III v4 design. A sample GaAs module produced can be seen below. However, custom GaAs cells can be ordered for specific voltages and shapes.

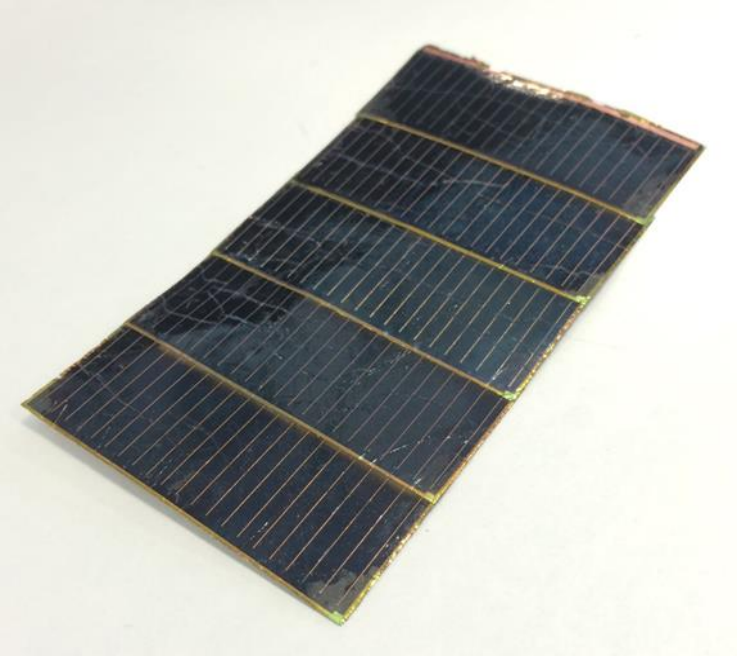

Figure 6.4: Sample GaAs photovoltaic solar module

Through previous investigations, the effects of integrating the A-Si cells is well known; however, integrating other solar cell materials will be slightly different due to their difference in mass and stiffness. The physical properties of these materials must be compared so that the change in performance can be predicted. A stiffness coefficient must be found for each of the materials to understand how much more or less the wings will deform while flapping. The density of the cells must also be found to determine the change in weight of the vehicle and wings. To determine the stiffness coefficient, the elastic modulus of each material was found using a micro tensile testing machine. A sample was cut from all of the solar cell materials as well as the Mylar material that makes up the membrane of the Robo Raven's wings. The surface of the sample was painted in a speckle pattern. This machine applied a continuous tensile load on the sample while a 2D Digital Image Correlation system measure the strain on the speckled surface of the sample. This enables us to measure

the force and strain on sample. Using the cross-sectional area of each sample, the Elastic modulus was calculated by observing the elastic region of the results.

The thickness of all of these materials will play a major role in stiffness. However, the Mylar was the only material that was isotropic. The other materials consisted of layered materials and the weakest layer of that material would cause the failure. Below are the physical characteristics of the different materials that were investigated.

Table 6.1: Comparison of photovoltaic materials

Material	Thickness (mm)	Elastic Modulus (GPa)	Stiffness Coefficient	Volumetric Density (kg/m^3)	Density by Area (kg/m^2)
Mylar	0.025	3.2	0.08	1390	0.0353
A-Si Cell	0.14	1.7	0.24	1420	0.199
Polycrystalline Cell	0.23	7.1	1.63	2110	0.486
GaAs Cell	0.14	1.5	0.21	1580	0.221

Analyzing these results, it becomes quite clear which high efficiency solar technology would be the best fit for the next Robo Raven III design. The polycrystalline cells were 6.8 times stiffer than the A-Si cells and 2.4 times heavier per unit surface area. The integration of the polycrystalline solar cells would clearly have a negative effect on performance when compared to the performance of Robo Raven III v4. The large increase in mass will make it more difficult for the motors to actuate the wings. The large increase in stiffness will not allow the wings to deform when the deformation is necessary to produce the thrust and lift forces to maintain flight. The only way to integrate polycrystalline cells into the FWAV is to limit the integration to just the body and tail of the vehicle.

6.3 A-Si and Polycrystalline Powered Vehicle

To determine the benefits that using polycrystalline photovoltaic cells can potentially bring, a FWAV was designed that incorporated them into the body and tail of Robo Raven III. As previously stated, Polycrystalline cells were initially integrated into the wing; however, through the fabrication process these cells began cracking and falling apart. Even when the wings were fabricated without breaking the solar cells, upon initial testing, the forced deformation of the wing induced by flapping caused the cells to crack and eventually completely fracture. Integrating these cells into the wings was simply not an option.

To stay consistent with the aerodynamic performance of the previous Robo Raven III v4 vehicle [51], the same wing geometry was chosen for the new polycrystalline tail. To sufficiently cover a similar area, two different sized polycrystalline modules were integrated into the tail. The first were 2 large 15x8cm modules that can each generate 1.9W. The second were 8 small 5.8x1.9cm modules that each generated 0.14W. One additional large polycrystalline module was integrated to the body of the FWAV. These polycrystalline solar cells alone generate 6.82W of power. Including the 30 A-Si modules already integrated into the wings, this platform generates 15.82W. The new tail design can be seen in Figure 6.5.

Figure 6.5: Polycrystalline tail and body integrated to Robo Raven III v4

Outdoor testing was performed to understand how the increase in power translates to an increase in flight time. First, the FWAV was held in place and oriented so that the solar cells produced the most power. The vehicle was first flapped with just the battery integrated to determine the flight time without the solar cells. Then, the vehicle was flapped with the solar cells to determine the benefit the solar cells provide. Without the solar cells, the vehicle flapped for 3 minutes and 35 seconds. With the solar cells the vehicle flapped for 4 minutes 45 seconds. This was 10 seconds more than the 36 A-Si FWAV. The previous design demonstrated a 22% increase in power for the vehicle where the new design that includes the polycrystalline cells had a 33% increase in power. This vehicle generated the most power out of any Robo Raven III design manufactured and can be seen in Figure 6.6.

Figure 6.6: Robo Raven with polycrystalline solar cells in the tail and body, and Powerfilm flexible solar cells in the wings.

The benefits in power generation are clearly there; however, the polycrystalline cells added a substantial amount of weight compared to the previous design with the A-Si cells. Robo Raven III v4 only had a payload of 32.6g [51]. When the battery is considered, this is only an extra 6g of payload capacity. The new tail and body weighed 11.1g more than the previous design. This increase in mass proved to be detrimental during actual flight tests. The FWAV could not maintain flight simply due to the increase in mass. From this it was concluded that the benefits provided by the polycrystalline cells did not outweigh their negative effects on flight.

The best path forward is to use the GaAs solar cells. The GaAs cells are less stiff than the A-Si cells. This means that the integration of these solar cells is expected to be similar to the integration of the solar cells used for Robo Raven III v4. The GaAs cells are slightly denser than the A-Si cells but they are so much more

efficient that they will not take the same surface area to achieve completely solar flight.

6.4 Modeling of the Effects of Wing Characteristics on Flapping Power, Thrust, and Lift

Integrating different materials into the wing structure changes the aerodynamic forces the wing can produce. It changes how the wings deform and therefore how much air the wings can interact with during the flapping cycle. For this vehicle, the design of the flapping wing plays a major role in force production. The planform area of the wing, weight of the wing, and stiffness of the wing are expected to alter the performance of the FWAV. The weight of the wing will alter the flapping amplitude and frequency of the wing. Applying a larger load makes it more difficult for the motors to actuate the wings. This result in a slower flapping rate with a smaller amplitude. The velocity profile of the flapping wing, v_o, is given by the following equation [51].

$$v_o = 2fr(\theta_{max} - \theta_{min}) \tag{6.1}$$

Where f is the flapping frequency, r is the distance any given point on the wing from the axis of rotation, and θ is the angle of the wing during the flapping cycle. This equation was adapted from the angular velocity of the wing and described in terms that can be used in predictive models. The velocity is limited by the motor torque motor.

The power effects for the drag of the wing flapping through air and against gravity were adapted from Wu et al. [45] and can be calculated as follows:

$$P = \int C_D \rho v^3 \, dA + mgc_g w \tag{6.2}$$

Where C_D is the drag coefficient of the wing, ρ is air density, A is the wing area, m is the mass of the wing, c_g is the center of gravity for the wing measured from the motor that actuates the wing, and w is the angular velocity of the wing. However, power effects are expected to change under different operating conditions and for different wing designs. As described in previous findings [38], they can be easily transformed when the axis of rotation is reoriented to the angle of attack during flight. Therefore, the power effects can be accounted for when the velocity, mass of the wing, center of gravity, and flapping angle change for each wing design.

Our previous studies on compliant wing structures have shown that there is a direct correlation between spar deformations and thrust [25]. In these studies, analytical models of the wing shape and aerodynamic forces generated (F_L and F_T) due to drag during flapping have been employed and adapted from previous work, and then were modified to include aerodynamic lift as follows [38]:

$$F_L = \int C_D \rho v^2 \cos(\theta)\, dA + C_L S \rho v_f^2 \tag{6.3}$$

$$F_T = \int C_D \rho v^2 \sin(\theta)\, dA \tag{6.4}$$

where C_L is the coefficient of lift, S is the planform area of the wing, θ is the angle of attack, and v_f is the forward velocity of the platform. These equations describe the forces generated when the axis of rotation is in the direction of thrust due to the drag of the wing as it rotates, along with the lift generated as it is dragged forward through the air during flight. This model produced good correlation with observed trends in lift and thrust, which conformed to assumed characteristics of the wings generating these loads. Therefore, these models can be used to predict the changes in lift and thrust production for each wing design due to the integration of solar cells.

In addition, empirical terms have been employed for the thrust to account for the compliance of the wing while the wing captures air during its deformed state and pushes air towards the rear of the vehicle at the apex and nadir of the flapping cycle, known as the "blowback effect", as follows [38]:

$$\Delta F_D = (kf)\sin\left(\frac{\pi(\theta-\theta_i)}{\theta_f-\theta_i}\right) \tag{6.5}$$

$$v = \left(1-\frac{D_f}{c\delta}\right)v_o \tag{6.6}$$

where ΔF_D is the change in total drag force that is decomposed into corresponding contributions to lift and thrust as given in equations (4) and (5) based on the angle of attack, k is an empirical constant of proportionality previously determined to be 0.2, f is the flapping frequency, θ is the angle of the wing during the flapping cycle, D_f is the level of the drag force above the point at which the deformation transitions from global to local during blowback, c is the global stiffness of the wing, δ is the displacement of the mid-chord of the semi-span of the wing if it were infinitely rigid, and v_o is the corresponding rigid wing velocity. It is important to note that the contribution from ΔF_D to thrust and lift only occurs when the wing is near apex or nadir [25].

The global stiffness of the wing will change with different solar cell materials and allows for the change in lift and thrust to be predicted. Based off Equation (6.6), increasing the global stiffness will decrease the flapping velocity of the wing. This decrease in velocity decreases the aerodynamic forces given in Equations (6.3) and (6.4). The global stiffness can be found using the following equation that follows the linear rule of mixtures:

$$c = k_m(A_m/S) + k_s(A_s/S) \tag{6.7}$$

where k_m and k_s are the stiffness coefficients of the Mylar membrane and solar cell material respectfully and A_m and A_s are the percent area of the wing taken up by the mylar and solar cell material. Using this global wing stiffness in the velocity equation (6.6) allows the lift and thrust forces to be predicted for different wing designs.

6.5 Wing Design for Integrated GaAs Solar Cells

Integrating the GaAs solar cells into wings follows the same process as the A-Si cells except slightly easier. The manufacturer can develop custom photovoltaic solar cells to meet the needs of Robo Raven. They can provide a cell module that operates at 7.68V while providing a 233mA current. Each module measures 141.8mm x 50mm and provides 1.712 W. This means we will only need 22 GaAs solar modules to reach the 37W needed to completely power Robo Raven IIIv5. That is a total area of 0.156m^2 that needs to be taken up by solar cells on the vehicle. Robo Raven III v4 has 0.290m^2 taken up by solar cells with 0.241m^2 on the wings. With 6 of the new GaAs cells being integrated into the tail and body, only 16 modules need to be integrated into the wings. That is a total area of 0.113m^2 of the wings that needs to be taken up by GaAs solar cells. That is 53% less surface area than is taken up by the A-Si cells in Robo Raven III v4's wing design. Since less surface area of the wing is taken up by the solar cells, this new wing design will go through larger deformations while flapping than the Robo Raven III v4 design.

Not only do these modules take up less surface area, preparing them for wing integration is much easier. The A-Si modules came with an encapsulation that needed to be removed to reduce the module's stiffness and mass. The manufacturer

of the GaAs cells is able to send the custom modules without any encapsulation. This eliminates a very time consuming process in wing fabrication.

To build these new wings, the GaAs cells must be available. Due to the high demand for this newer more efficient technology, using a mock material instead of the actual GaAs cells is preferable. The best option was to use a material that had a similar or higher stiffness coefficient with the same density. If flight can be achieved with a stiffer material, then flight can be achieved with the GaAs cells; however, the same density is required to replicate the load on the motors and total payload of the vehicle. The material used as the mock material was 110 copper. A 0.025mm thick roll was cut into the same shape as the GaAs cells. The copper shim was about twice the stiffness of the GaAs cells, but had the exact same density as the solar cells. If the new wings can achieve flight with these mock copper cells, then they would be able to achieve flight with the actual GaAs cells.

To actually make the new wings, the layout of the solar cells must be determined. Keeping the solar cell at the front most section of the wing allows for the best performance [47]. Using the same size and geometry of the Robo Raven III v4 wings, 8 mock GaAs cells can be easily integrated into the front most portion of the wings. This design calls for the 8 modules to be laid in two horizontal rows. When complete this wing looks very similar to a larger version of Robo Raven III v1. Interestingly though this design will harvest enough energy to completely power the FWAV. This wing weighed 37.2g which was 21.5g less than Robo Raven III v4's wing. A picture of the completed wing can be seen in Figure 6.7.

Figure 6.7: Left: Mock GaAs wings Right: Completed Robo Raven III v5 design

With the additional 6 cells on the tail and body of the FWAV, this vehicle mimics a solar cell powered FWAV. If this vehicle were to have the actual high efficiency GaAs solar cells, it would have the capability to stay in flight as long as there is sunlight. However, this vehicle must be able to maintain flight. Comparing this vehicle's performance to the performance of Robo Raven III v4 would show a clear understanding of the effects of the vehicle's performance and the effects of changing the design and material used for solar cell integration.

6.6 Performance of Mock GaAs Wings

To quantify the difference in performance that these changes to the wing cause, the previous wing performance was compared to the performance of the new design. The forces generated by each wing design were measured and compared. The same test stand with a 6 degree of freedom from Chapter 5 was used to measure the forces produced by the wings. This 6 DOF load cell is capable of measuring up to 40 N of force with a resolution of 0.01 N in the thrust direction and 120 N of force with a resolution of 0.02 N in the lift direction. It allows us to simultaneously record the lift and thrust forces being produced. The raw signal is sent through a Labview

program that converts the raw voltage to forces and the data is platted in an Excel file. The raw time resolved results can be seen below.

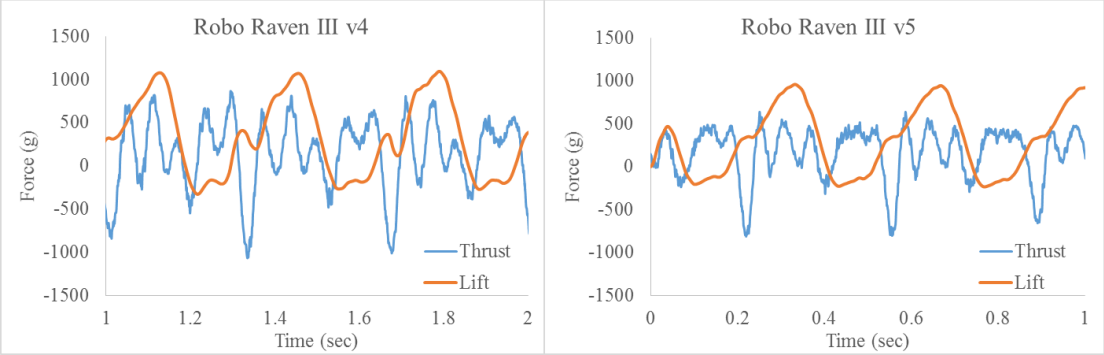

Figure 6.8: Time resolved results of Robo Raven III v4 and v5

To compare the difference in performance the average forces produced by each wing design were observed. These lift and thrust forces are necessary to maintain flight and can be predicted using the models mentioned before. The results demonstrate that the new Robo Raven III v5 wings produce more thrust and less lift than Robo Raven III v4 as was predicted by the models. This was expected because the ability for the wing to deform increased causing more thrust to be generated while flapping. However, the greater mass of the Robo Raven III v4 wing allows more lift to be generated during the downwards portion of the flapping cycle.

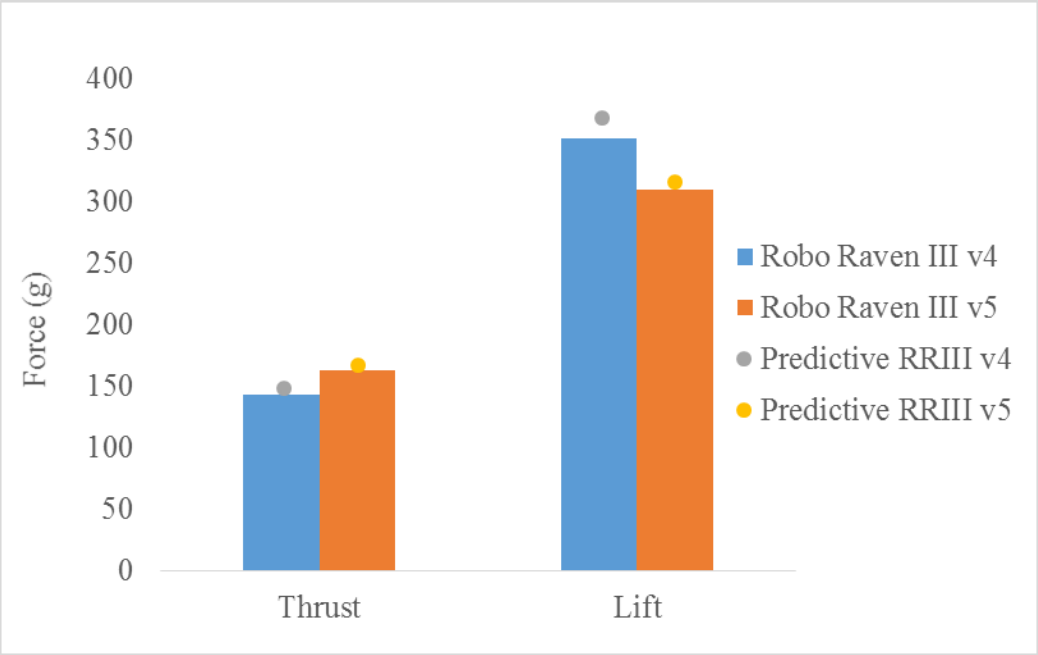

Figure 6.9: Average lift and thrust generated and compared to the predicted results

From these measured results, a prediction can be made about the actual flight results. Like airplane or a fixed wing aircraft, this type of FWAV relies heavily on the production of thrust to generate lift. However, this vehicle has the advantage of also generating lift by flapping. Ideally to measure the actual lift force each vehicle is capable of producing, the average thrust force should reach 0g. The extra thrust produced by Robo Raven III v5 would translate to more lift. How much is unclear for this new design. The best way to discover the lift is to run payload tests with the new design. Actual flight tests are the final real test to directly compare the two designs. The results from actual flight tests can be seen below.

Table 6.2: Flight Characteristics of Robo Raven III v4 and v5

	Total Vehicle Mass (g)	Forward velocity (m/s)	Climb Rate (m/s)	Payload (g)
Robo Raven III v4	381	5.6	0.23	32
Robo Raven III v5	340	7	0.55	42

Robo Raven III v5 had an additional 10 grams of payload. Even though the wing from Robo Raven III v4 generated more force, it had to overcome a larger vehicle mass. The payload measured did not include the battery necessary for flight. If the payload included the 27 gram battery, the payload actually goes down to 5 grams for Robo Raven III v4. Since this FWAV developed had a material that mimicked the actual high efficiency solar cells, a battery had to be used to power this vehicle. However, with the actual high efficiency GaAs cells, only a very small battery or large capacitor must be used to safely help power the vehicle. The payload will still be close to 40 grams with the GaAs cells. Not only will this FWAV fly longer than its predecessor, it will actually have better performance as well.

6.7 Expected Electrical Impact of New Design

The combination of wing design and solar cell technology in Robo Raven III v5 is expected to outperform any previous version and produce enough energy through solar power to completely power the vehicle. The percentage of the wing covered by solar cell material and efficiency of the solar cell material play a major role in the amount of power that can be produced. The following plot demonstrates the potential of the wing design used.

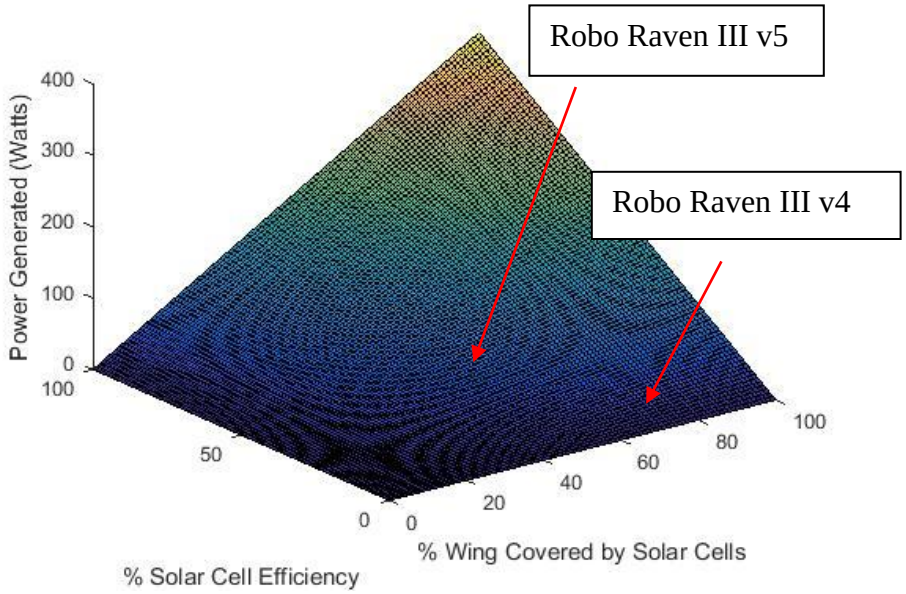

Figure 6.10: Potential Power produced by Robo Raven III v5 wing design

Ignoring the fact that the maximum theoretical photovoltaic efficiency is 86% and a wing that is completely covered by would never fly, this wing design can produce 327.5 Watts of electrical power. However, we are limited to the efficiency of thin film solar cell technology. Figure 6.11 demonstrates the potential of the A-Si cell and the GaAs cell.

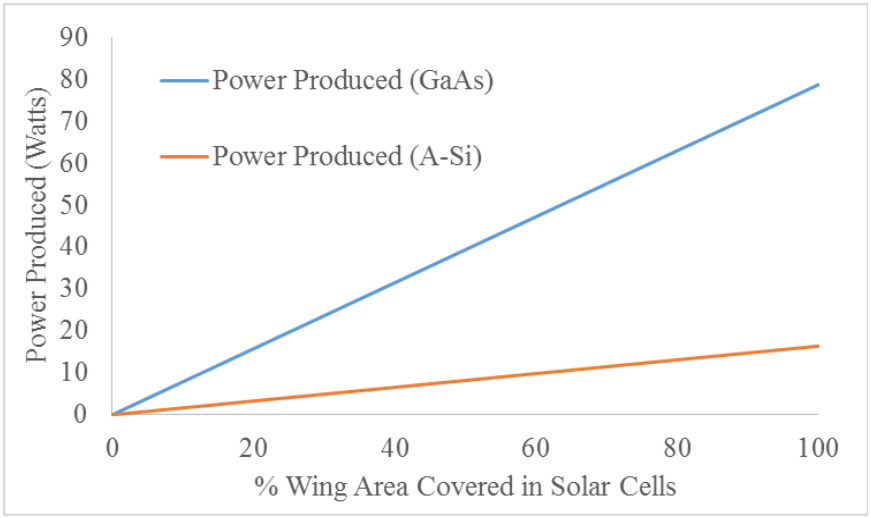

Figure 6.11: Power produced by available solar cell technology for Robo Raven III v5 wing design

Needing only 37 Watts to power the entire vehicle, the new wing design with GaAs cells requires less than half of the total wing area to produce that power. Using the A-Si cell, this goal would never have been reached. The Robo Raven III v4 wing used more than 50% of it wing area and was still capable of flight. This means that The GaAs version will be able to fly. It will also be able to rely solely on solar power to fly.

6.8 Conclusions

Current battery technology has limitations when applied to FWAVs. The necessity for a small lightweight battery limits how much energy can be stored to be used during flights. This means that typical flights and missions for FWAVs can only span a short distance for a limited amount of time. Previous energy harvesting efforts have proven that solar cells can be integrated to the wings, tail and body of FWAVs and more specifically Robo Raven. Previous versions of Robo Raven III used amorphous silicon cells. These cells allowed for investigations of how wing deformation is affected by solar cell integration; however, lacked the efficiency to provide prolonged or completely solar flight.

This investigation sought to understand the integration of high efficiency solar cells into an already established viable design. Different solar cell technologies were observed and gallium arsenide cells were determined to be the best material to be integrated to the wings. With a similar stiffness and density to the A-Si cells, not much difference was expected in terms of performance. Using this stiffness, a model that was previously developed was adapted to include a change in performance

caused by changes in stiffness to the wing. This model allowed the performance of the new wing design to be predicted.

Without being able to acquire the GaAs solar cells, copper shim material was used as a substitute material. This copper shim was the same density, but twice as stiff as the solar cells. This meant that if the new wing design was capable of flight with this material, it would be capable of flight with the GaAs cells. The increase in efficiency from the A-Si cell to the GaAs cells is dramatic enough that less of the win's surface area is used to harvest all of the energy needed to power the FWAV while in flight. The new design called for 16 GaAs modules to be integrated to the front most portion of the wing, 4 modules in the tail, and an additional 2 modules in the body. The final completed design was named Robo Raven III v5.

Load cell testing was done to compare the performance of Robo Raven III v5 to the previous design (Robo Raven III v4). It was found that the new design outperformed the previous version with respect to thrust but underperformed with respect to lift. The increase in deformation is what caused this increase in thrust. The additional mass of the previous version allowed it to achieve a larger force in lift. Even though the previous version generated more lift it also had a larger mass to overcome to achieve flight. The new Robo Raven III v5 had a smaller overall mass and had a larger payload capacity than Robo Raven III v4. Taking into account the weight of the battery, Robo Raven III v4 had a total payload capacity of 5g. Since Robo Raven III v5 does not need a battery, it has a total payload of 40g. This means that Robo Raven III v5 mechanically outperforms the previous version. By actually

integrating the GaAs cells into the wings of this final design. The first FWAV with the capability to fly indefinitely with sunlight will be developed.

Chapter 7: Conclusions

There were several contributions to the field of FWAVs that came from this work. Although this work can be seen as pioneering in terms of solar cell integration to different structures of FWAVs, there were many small contributions along the way that gave new insight to the field in general. These contributions include new testing methods, new fabrication methods, and intellectual contributions.

7.1 FWAV Fabrication

The integration of solar cells into various structures of the Robo Raven platform required new fabrication techniques to be developed. The methods for developing these new structures have been established through this work using an additive manufacturing approach based on layered object manufacturing. The fabrication technique for wings with integrated solar cells was also used to integrate solar cells into the tail structure. This included both mechanical and electrical integration of the solar cells into these structures. Thus a FWAV that flew on both battery and solar power was created and flown.

This work also developed 5 new versions of the Robo Raven III vehicle. The effects of hanging the wings design were clearly investigated. Even though the larger version consumed more power, they lead to a design that has the ability to rely solely on solar power for flight. Although Robo Raven III v5 was not actually made with the GaAs solar cells, it is the most impressive. While still capable of flight, a swap of the copper used to simulate the GaAs cells for the actual solar cell will produce a FWAV that has the potential to fly completely on solar power.

7.2 Characterization

7.2.1 Characterization of Aerodynamic Forces

The forces produced by new wing designs was a major aspect of this work. Even though these loads have been measured in different ways in the past, the development of our test stand was novel. Not only was the technology used better than what was used previously, but the flexibility to test different conditions while only making small adjustments to the test stand was new.

Previously, a single axis load transducer was used to measure the forces generated by a smaller FWAV [23,25,26]. This did not allow for simultaneous lift and thrust to be collected. With the new test stand, a 6 DOF load transducer was used to simultaneously collect all of the loads and moments generated by the FWAV. We focused on just lift and thrust; however, this test stand is capable of measuring much more. As the work developed so did the test stand. We were able to measure the actual flapping amplitude using an optical encoder and the power consumed by the vehicle. We also made the test stand able to adjust the angle of the vehicle with the incoming air from the wind tunnel. This enabled actual flight conditions to be tested. This final test stand is a great tool that can be replicated in any lab and used to compare the behavior of different UAVs.

7.2.2 Characterization of Deformation using DIC

This work is also one of the few times that 3D DIC has been implemented on a flapping wing. This gave us valuable information as to what is occurring during the flapping process of the wing. Obtaining the deformation of a flapping wing at 4 Hz is a difficult task that required knowledge of both the actual testing technique and the

behavior of the FWAV. Even though DIC has been used for a FWAV before [28], these are the largest wings yet to be observed. This provided new challenges that needed to be overcome. For example the appropriate distance and location of the camera to the flapping wing needed to be found. Also the correct amount of lighting for the indoor high speed cameras was also found. Since the wings were so large typical speckling techniques could not be used and the wing needed to be hand painted. These difficulties lead to an accurate and correct process that enable anyone to of similar wing size to use these techniques and find more information in wing deformation and performance.

One major contribution that was touched on before is the information extracted from the 3D DIC data. A correlation between shear strain observed on the surface of the wing and thrust force generated was found. A correlation between the biaxial strain observed on the surface of the wing and lift force generated was also found. This new information in wing deformation allowed for a better wing design and lead to Robo Raven III v2.

7.2.3 Electrical Performance Characterization

Since the advantages of implementing solar cells into a FWAV needed to be observed, this lead to the development of electrical testing procedures for Robo Raven III. An endurance test was created that enables the new endurance of a solar powered FWAV to be determined. This required new circuitry that enables the FWAV to operate using two power sources. This circuitry involved a boost controller to increase the voltage of the solar cells to make it comparable to the voltage of the battery. The test itself involved several aspect that cannot be controlled. For example

the weather had to be a clear day with no clouds. Also, the FWAV needed to be held still at the correct azimuth to the sun to gain the most power possible.

The ability to recharge the battery was also tested for serval versions of Robo Raven III. This required the development of a new circuit to safely charge the lithium polymer battery using the energy harvest by the solar cells. Like the previous test, the weather also needs to be accommodating for these tests to take place. Although these electrical tests were conducted for a FWAV, these tests can be conducted for any vehicle using solar power.

7.2.4 Characterization of Self Sensing

An interesting finding in this work was how the solar cell was affected by the wing's deformation. This provides the wing with the ability to sense its own deformation using the power produced by the solar cell. The correlation to shear strain and thrust provides available onboard information on vehicle performance.

Thus, it was determined that multifunctional solar cell wings may be capable of three functions:

(1) Lightweight and flexible structure to generate aerodynamic forces,

(2) Energy harvesting to extend operational time and autonomy,

(3) Sensing of an aerodynamic force associated with wing deformation.

7.3 Modeling

7.3.1 Multifunctional Modeling

A multifunctional performance model was developed. This model broke the vehicle down in terms of mass and energy and allowed the increase in flight time to be predicted. This model can be used for any UAV and is not limited to FWAVs.

This means that the feasibility of introducing solar cells to any UAV can be determined before the project is started.

7.3.2 Aerodynamic Modeling

The information gained from vehicle performance allowed for predictive aerodynamic models for lift and thrust to be generated. The predictive models allow for changes in performance to be based off changes in design. These models can be applied to FWAVs that are designed to fly laterally (usually with a wingspan of 0.25m to 2.5). One model was used to predict changes in wing performance. The change in design causes a change in wing velocity that is used to predict the change in lift and thrust of the vehicle. The other predictive model was used to predict how changes in the tail would affect tail performance. These models were based off the coefficient of lift and drag of a plane through air.

Finally by introducing stiffness as a component in wing design, the effects of integrating other materials to the wings can be predicted. The model produced altered the previously mentioned wing lift and thrust models to compensate for global stiffness. An equation for global stiffness allowed for a wing with different materials to obtain one global stiffness coefficient and be plugged into the lift and thrust model. This allowed for a more robust model that can be used not only for solar cells but different membrane materials. In result from the fabrication, characterization and modeling work accomplished for the different version of Robo Raven III, the new flight times, recharge times, thrust forces, and lift forces were predicted and measured for each version created. A table summarizing the work accomplished can be observed below. The total flight weight is the total weight of the FWAV and how

much payload the vehicle can carry during flight. By subtracting the vehicle's weight, the payload for each Robo Raven III version can be found.

Table 7.1: Summary of each version of Robo Raven III fabricated

	Robo Raven III Version 1	Robo Raven III Version 2	Robo Raven III Version 3	Robo Raven III Version 4	Robo Raven III Version 5
Predicted Increase in Flight Time (sec)	29	42	54	68	Infinite with 100% Sunlight
Measured Increase in Flight Time (sec)	27	38	42	50	Was Not Measured
Predicted Increase Recharge Time (min)	74	41	27	20	0
Measured Increase in Recharge Time (min)	149	90	52	44	Was Not Measured
Predicted Total Flight Weight (grams)	332	367	405	410	380
Measured Total Flight Weight (grams)	332	361	399	413	382
Predicted Payload Including Battery (grams)	41	53	35	29	40
Measured Payload Including Battery (grams)	41	47	29	32	42

7.4 Future Work

Based off the progress and findings in this work, there are several directions that that can be taken for future work. First, the actual GaAs solar cells can be integrated into the current Robo Raven III v5 design. This would be a culmination of all of the concept and findings presented in this dissertation. The results from the

actual GaAs can also be compared to the predicted results obtained by the mock cells used. To successfully power this FWAV on solar power, some investigation must be done on using a capacitor to control the flow of energy to the vehicle. From flapping the power supplied by the solar cells is expected to constantly change, so a capacitor is needed to supply constant power.

Another aspect that can be further explored is the solar sensing that was discovered in this work. Actually using these solar cells as a sensor can provide real time feedback that would allow for autonomous flight corrections.

A valuable tool that can be developed from using more DIC data would be an aerodynamic model for FWAVs. This model would incorporate the deformation and translation of the wing with the load produced due to the incoming air during flight. This involves simultaneous mechanical and fluid simulations. The results from the simulation can be compared to the measured DIC and load cell results. This is a huge undertaking, but would be an extremely valuable tool for FWAVs.

One final direction that can be taken going further is to integrate flexible batteries to the wings. With the development of thin flexible batteries, it is not far off to integrate these batteries similar to how the solar cells have already been integrated. This can be taken further and batteries and solar cells can both be integrated. These are all extension of the work that has been accomplished in this dissertation.

Bibliography

[1] Gerdes JW, Gupta SK and Wilkerson S (2012) A Review of Bird-Inspired Flapping Wing Miniature Air Vehicle Designs. ASME Journal of Mechanism and Robotics. 4(2). 021003.1-021003.11.

[2] Kumar V and Michael N, (2012) Opportunities and Challenges with Autonomous Micro Aerial Vehicles. The International Journal of Robotics Research. vol. 31, pp. 1279-1291. DOI 10.1177/0278364912455954.

[3] Sane, SP and Dickinson, MH (2002) The Aerodynamic Effects of Wing Rotation and a Revised Quasi-Steady Model of Flapping Flight. Journal of Experimental Biology. 205: 1087–1096.

[4] Yan J, Wood RJ, Avadhanula S, Sitti M and Fearing RS (2001) Towards Flapping Wing Control for a Micromechanical Flying Insect. Proceedings ICRA. IEEE International Conference on Robotics and Automation. 2001, 4:3901-3908.

[5] Ma KY, Chirarattananon P, Fuller SB and Wood RJ (2013) Controlled Flight of a Biologically Inspired, Insect-Scale Robot. Science. 340(6132), 603–607.

[6] Fenelon MAA and Furukawa T (2009) Design of an Active Flapping Wing Mechanism and a Micro Aerial Vehicle Using a Rotary Actuator. Mechanism and Machine Theory. 45(2):137-146.

[7] Zdunich P, Bilyk D, MacMaster M, Loewen D, DeLaurier J, Kornbluh R, Low T,Stanford S and Holeman D (2007) Development and testing of the mentor flapping-wing micro air vehicle. Journal of Aircraft. 44(5):1701–1711.

[8] Keennon M, et al. (2012) Development of the Nano Hummingbird: A Tailless Flapping Wing Micro Air Vehicle. presented at 50th AIAA Aerospace Sciences Meeting. Nashville, Tennessee.

[9] Pornsin-Sirirak T, Tai Y, Ho C and Keennon M (2001) Microbat: A Palm-Sized Electrically Powered Ornithopter. Proceedings of the NASA/JPL Workshop on Biomorphic Robotics. Pasadena, CA.

[10] de Croon GCHE, de Clerq KME, Ruijsink R, Remes B and de Wagter C (2009) Design, Aerodynamics, and Vision-Based Control of the Delfly. International Journal of Micro Air Vehicles, 1(2):71-97.

[11] Bejgerowski W, Ananthanarayanan A, Mueller D and Gupta SK (2009) Integrated Product and Process Design for a Flapping Wing Drive-Mechanism. Journal of Mechanical Design. Vol. 50, pp.725-735.

[12] Jones KD, Bradshaw CJ, Papadopoulos J and Platzer MF (2004) Improved Performance and Control of Flapping-Wing Propelled Micro Air Vehicles. Proceedings of the AIAA 42nd Aerospace Sciences Meeting and Exhibit. Reno, NV.

[13] Anton, S. R., & Inman, D. J. (2008, March). Vibration energy harvesting for unmanned aerial vehicles. In The 15th International Symposium on: Smart Structures and Materials & Nondestructive Evaluation and Health Monitoring (pp. 692824-692824). International Society for Optics and Photonics.

[14] Shah, A., Torres, P., Tscharner, R., Wyrsch, N., & Keppner, H. (1999). Photovoltaic technology: the case for thin-film solar cells. science, 285(5428), 692-698.

[15] Aberle, A. G. (2009). Thin-film solar cells. Thin Solid Films, 517(17), 4706-4710

[16] Antartis, D., & Chasiotis, I. (2014). Residual stress and mechanical property measurements in amorphous Si photovoltaic thin films. Solar Energy, 105, 694-704.

[17] Nemat-Nasser S, Plaistead T, Starr A and Amirkhizi A (2005)Multifunctional Materials. Biomimetics: Biologically Inspired Technologies, Ed. Y. Bar-Cohen. CRC Press.

[18] Bejgerowski W, Gupta SK and Bruck HA (2009) A Systematic Approach for Designing Multifunctional Thermally Conducting Polymer Structures with Embedded Actuators. Journal of Mechanical Design. 131(111009):1-8.

[19] Thomas JP and Qidwai MA (2005) The Design and Application of Multifunctional Structure-Battery Materials Systems. JOM. Vol 57 (3), pp. 18-24.

[20] Thomas JP et al (2005) Multifunctional Structure-Plus-Power Concepts. *AIAA*. 43rd AIAA/ASME/ASCE/AHS/ASC Structures, Structural Dynamics, and Materials Conference, Denver, CO.

[21] Yang LJ, Hsu CK, Ho JY and Feng CK (2007) Flapping Wings with Pvdf Sensors to Modify the Aerodynamic Forces of a Micro Aerial Vehicle. Sensors and Actuators A: Physical, Vol. 139 (1-2)pp. 95-103..

[22] Hsu CK, Ho JY, Feng GH, Shih HM and Yang LJ (2006) A Flapping MAV with PVDF-Parylene Composite Skin. Proceedings of the Asia-Pacific Conference of Transducers and Micro-Nano Technology.

[23] Wissman J, Perez-Rosado A, Edgerton A, Levi BM, Karakas ZN, Kujawski M, Phillips A, Papavizas N, Fallon D, Bruck HA and Smela E (2013) New Compliant Strain Gauges for Self-Sensing Dynamic Deformation of Flapping Wings on Miniature Air Vehicles. Smart Materials and Structures. 22(8), 085031.

[24] Mueller D, Gerdes JW and Gupta SK (2009) Incorporation of Passive Wing Folding in Flapping Wing Miniature Air Vehicles. ASME Mechanism and Robotics Conference. San Diego, CA.

[25] Mueller D, Bruck HA and Gupta SK (2010) Measurement of Thrust and Lift Forces Associated With Drag of Compliant Flapping Wing Air Micro Air Vehicles Using a New Test Stand Design. Experimental Mechanics. Vol 50, pp. 725-735.

[26] Gerdes JW, Cellon KC, Bruck HA and Gupta SK (2013) Characterization of the Mechanics of Compliant Wing Designs for Flapping-wing Miniature Air Vehicles. Experimental Mechanics. DOI 10.1007/s11340-013-9779-5.

[27] Hsu CK, Evans J, Vytla S and Huang P (2010) Development of Flapping Wing Micro Air Vehicles - Design, CFD, Experiment and Actual Flight. 48th AIAA Aerospace Sciences Meeting. Orlando, FL.

[28] Wu, P., Stanford, B., Bowman, W., Schwartz, A., & Ifju, P. (2009). Digital Image Correlation Techniques for Full-Field Displacement Measurements of Micro Air Vehicle Flapping Wings. Experimental Techniques, 33(6), 53-58.

[29] Pines DJ and Bohorquez F (2006) Challenges Facing Future Micro-Air-Vehicle Development. Journal of Aircraft. Vol 43 (2), pp. 290-305.

[30] Cox A, Monopoli D, Cveticanin D, Goldfarb M and Garcia E (2002) The Development of Elastodynamic Components for Piezoelectrically Actuated Flapping Micro-Air Vehicles. Journal of Intelligent Material Systems and Structures. 13(9):611-615.

[31] Muijres FT, Johansson LC, Barfield R, Wolf M, Spedding GR and Hedenstrom A (2008) Leading-Edge Vortex Improves Lift in Slow-Flying Bats. Science. 319: 1250–1253.

[32] Zhao L, Huang Q, Deng X and Sane S (2009) Aerodynamic Effects of Flexibility in Flapping Wings. Interface. 7: 485–497.

[33] Mahjoubi H and Byl K (2013) Trajectory Tracking in the Sagittal Plane: Decoupled Lift/Thrust Control via Tunable Impedance Approach in Flapping-Wing MAVs. American Control Conference (ACC). pp. 4951-4956.

[34] Arabagi V, Hines L and Sitti M (2012) Design and Manufacturing of a Controllable Miniature Flapping Wing Robotic Platform. *The International Journal of Robotics Research*. 0278364911434368.

[35] Mueller TJ (2001) Fixed and Flapping Wing Aerodynamics for Micro Air Vehicle Applications. *American Institute of Aeronautics and Astronautics*. Reston, VA.

[36] Tsai BJ and Fu YC (2009) Design and Aerodynamic Analysis of a Flapping-Wing Micro Aerial Vehicle. *Aerospace Science and Technology*. 13(7), 383-392.

[37] Madangopal R, Khan Z and Agrawal S (2005) Biologically Inspired Design of Small Flapping Wing Bird Vehicles Using Four-Bar Mechanisms and Quasi-Steady Aerodynamics. *Journal of Mechanical Design*. 127(4), 809-816.

[38] Gerdes J, Holness A, Perez-Rosado A, Roberts L., Greisinger A, Barnett E, Kempny J, Lingam D, Yeh C-H, Bruck HA, and Gupta SK (2014) Robo Raven: A Flapping-Wing Air Vehicle with Highly Compliant and Independently Controlled Wings. *Soft Robotics*. 1(4), 275-288.

[39] Perez-Rosado A, Griesinger AJG, Bruck HA, and Gupta SK (2014) Performance Characterization of Multifunctional Wings with Integrated Solar Cells for Miniature Air Vehicles. ASME 2014 International Design Engineering Technical and Computers and Information in Engineering Conference, Buffalo, NY.

[40] Stanford, B, Ifju, P, Albertani, R, & Shyy, W (2008) Fixed membrane wings for micro air vehicles: Experimental characterization, numerical modeling, and tailoring. *Progress in Aerospace Sciences.* 44(4), 258-294.

[41] Tice, Brian P (1991). Unmanned Aerial Vehicles – The Force Multiplier of the 1990s. *Airpower Journal.* 41-54.

[42] Gerdes, J, Bruck H, and Gupta SK (2015) A Systematic Exploration of Wing Size on Flapping Wing Air Vehicle Performance. ASME Mechanism and Robotics Conference, August, Boston, MA.

[43] Holness A, Bruck H, and Gupta SK (2015) Design of Propeller-Assisted Flapping Wing Air Vehicles for Enhanced Aerodynamic Performance. ASME Mechanism and Robotics Conference, August 2015, Boston, MA.

[44] Bauhuis GJ, Mulder P, Haverkamp EJ, Huijben JCCM, Schermer JJ (2009) 26.1% thin-film GaAs solar cell using epitaxial lift-off. Solar Energy Materials and Solar Cells. 93(9):1488-1491.

[45] Lin Q, Huang H, Jin Y, Fu H, Chang P, Li D, Yao Y, Fan Z (2014) Flexible Photovoltaic Technologies. Journal of Materials Chemistry C. 2(7):1233-1247.

[46] Roberts L, Bruck, HA and Gupta SK. (2014) Autonomous Loitering Control for a Flapping Wing Aerial Vehicle with Independent Wing Control. ASME 2014 International Design Engineering Technical and Computers and Information in Engineering Conference, August, Buffalo, NY.

[47] Perez-Rosado A, Gehlhar RD, Nolen S, Gupta SK, & Bruck HA (2015). Design, fabrication, and characterization of multifunctional wings to harvest solar energy in flapping wing air vehicles. Smart Materials and Structures, 24(6), 065042.

[48] Polhamus, EC (1966). A concept of the vortex lift of sharp-edge delta wings based on a leading-edge-suction analogy. National Aeronautics and Space Administration, 1-15.

[49] Taylor GK, Nudds RL, & Thomas AL (2003) Flying and swimming animals cruise at a Strouhal number tuned for high power efficiency. Nature, 425(6959), 707-711.

[50] Perez-Rosado A, Bruck HA, Gupta SK (2015) Enhancing the Design of Solar-Powered Flapping Wing Air Vehicles using Multifunctional Structural Components. ASME IDETC/CIE, Mechanisms and Robotics Conference, August 2015, Boston, MA.

[51] Perez-Rosado A, Bruck H, Gupta SK (2015) Integrating Solar Cells into Flapping Wing Air Vehicles for Enhanced Flight Endurance. ASME. J. Mechanisms Robotics. doi:10.1115/1.4032411.

[52] Oh, J., Lee, K., Hughes, T., Forrest, S., & Sarabandi, K. (2014) Flexible Antenna Integrated With an Epitaxial Lift-Off Solar Cell Array for Flapping-Wing Robots. Antennas and Propagation, IEEE Transactions on, 62(8), 4356-4361.

[53] Videler, J.J. (2006) Avian Flight-Oxford Ornithology Series. OUP Oxford Press. Great Britain, UK.

[54] Allain R. (2012) Why cant Humans Fly Like Birds. Wired Digital. Conde Nast Digital. January 2012.